

**CLOUDBURSTS IN THE NEPAL HIMALAYAS: INTERACTION  
BETWEEN THE INDIAN MONSOON AND EXTRATROPICS**

**By**

**Archana Shrestha**

A dissertation submitted in partial fulfillment of  
the requirements for the degree of  
Doctor of Philosophy  
(Atmospheric and Oceanic Sciences)  
at the  
UNIVERSITY OF WISCONSIN-MADISON  
2016

Date of final oral examination: 8/16/2016

This dissertation is approved by the following members of the Final Oral Committee:

Gregory J. Tripoli, Professor, Atmospheric and Oceanic Sciences

Larissa E. Back, Associate Professor, Atmospheric and Oceanic Sciences

Matthew H. Hitchman, Professor, Atmospheric and Oceanic Sciences

Zenzang Liu, Professor, Atmospheric and Oceanic Sciences

Grace Wahba, Professor, Department of Biostatistics and Medical Informatics

© Copyright by Archana Shrestha  
All Rights Reserved

This dissertation is dedicated to the memory of  
my grandfather, KANAK NANDAN JOSHI, my role model.

## Acknowledgments

I was overwhelmed by the magnitude of the damage from the cloudbursts and the nature of these storms that I learned from the local people during my field visits in the disaster regions for my Masters project and as a Meteorologist in the Department of Hydrology and Meteorology in Nepal. I always wondered what type of atmospheric conditions might have played a role in such a devastating weather systems. Though, us meteorologists in Nepal knew what was going on at the surface during these events, we were unclear about the upper-level conditions.

Impressed with the North American education system, I always wanted to pursue in-depth research on the cloudbursts in the United States. With the Fulbright Science and Technology PhD Fellowship award and acceptance in the PhD program by my mentor Professor Gregory Tripoli and the AOS Department, I got an opportunity to pursue my dream in January of 2010. I am very thankful to the Fulbright Program for their financial and emotional support. When I received the Fulbright Award to pursue my degree in the Fall of 2010, my son was 9 months old. The program considered my request to postpone starting my degree from the Fall of 2009 to Spring of 2010 because of my family situation. I am thankful to Fulbright team in the US and in Nepal, especially, Yamal Rajbhandari, for understanding my situation.

I am incredibly grateful to my mentor Greg for his academic and humane support in last six years. I am most inspired by his “out-of box” intellectual point of views on the issues related to atmospheric science that led me to think differently than the classical ones. I

especially appreciate him challenging my classical point of view on the weather systems. I had once mentioned to him how mountains in Nepal complicate weather forecasting. Surprisingly he bestowed the virtues of mountains and their positive role for weather forecasting. To my surprise, he explained “mountains makes things easier if other variables are known; because this is the ‘variable’ that does not change but leaves significant impact on the weather.”

I am equally thankful to my co-advisor Professor Larissa Back for guiding me to make my research methods more objective. Her invaluable comments and guidance have helped shaping my research methodology. I immensely appreciate her encouragement and support for me to learn programming and statistical skills. I want to also thank my additional committee members Professor Liu, Professor Hitchman, and Professor Grace Wahba for their constructive feedbacks to shape my dissertation.

Without a tremendous help from Pete, I would not have been efficient to learn computing skills and complete data analysis for my research. I really appreciate Pete’s timeless support whenever I had issues with computing. He was always available in person or remotely whenever I needed assistance. I am also thankful to Kathy Kruger, Graduate Student Coordinator. Her assistance on issues pertaining to administrative procedures has been really invaluable. I am equally thankful to our research team William Lewis, Luke Odell and Scott Trevor for their helpful discussion, support and suggestions. I appreciate time and effort by Zac Handlos, Alex Goldstein, Melissa Breeden and Andrew

Winters in helping me while I was exploring my research methods. I am thankful to Prof. John Young and Prof. Michael Morgan for their suggestions during this research.

Finally, I would like to thank my colleagues in Nepal and the Department of Hydrology and Meteorology, Government of Nepal for allowing me to pursue this research. I am especially thankful to Director General, Dr. Rishi Ram Sharma and Deputy Director General Saraju Baidya for their administrative and academic support. I would like to acknowledge that this research was supported in part by NASA grants: NNX11AM93G and NNX13A078G and the Office of Naval Research project N000141410132.

Last but not least I am very fortunate to have very supportive and loving family members. I would like to thank my husband, Bishwa Shrestha for his unconditional support throughout this whole process. Support from my parents and my in-laws were tremendous help during hard times. Peer support from my younger sisters and my only brother was invaluable. I would like to end this note of acknowledgements with a lovely appreciation for my thoughtful son Bivaas Shrestha, who is now 7 years and keep asking me how he can help me to finish my study. He already claims he knows how tornadoes are formed.

## TABLE OF CONTENTS

<b>Dedication.....</b>	<b>i</b>
<b>Acknowledgements .....</b>	<b>ii</b>
<b>Table of Contents .....</b>	<b>v</b>
<b>List of Figures .....</b>	<b>ix</b>
<b>List of Tables.....</b>	<b>xvi</b>
<b>Abstract .....</b>	<b>xvii</b>
<b>1. Chapter 1: Introduction: Cloudbursts Overview and Issues .....</b>	<b>1</b>
1.1 Limited Meteorological Understanding.....	1
1.2 Scientific Issues and Research Questions .....	3
1.3 Hypothesis of the Study .....	8
1.4 Objectives of the Study.....	8
1.5 Road Map.....	8
<b>2. Chapter 2: Review: Extreme events in the Himalayas, Synoptic features of Extreme Events, Theories of Tropical-extratropical Interaction.....</b>	<b>10</b>
2.1 Meteorological Features of Extreme Monsoon Rainfall Events in the Himalayas.....	10
2.1.1 Cloudburst Characteristics in the Himalayas.....	10
2.1.2 Other Extremes Rainfall Events in Nepal.....	14
2.2 Synoptic Signatures of Extreme Rainfall Events.....	18
2.2.1 Quasi-stationary Upper-level System.....	18

2.2.2	Upper level positive PV anomaly perspective.....	19
2.3	Tropical-Extratropical Interaction Aspects of Extreme Rainfall Events.....	22
2.3.1	Upper-level Upper Force Imbalance Theory in Tropical-Extratropical Interaction.....	24
2.3.2.	Eddy Shedding: A Mechanism Linking Tropical Heating, Rossby Wave, Upper-level Force Balance and Tropical-Extratropical Exchange .....	33
<b>Chapter 3:</b>	<b>Methodology and Data.....</b>	<b>42</b>
3.1	Objective 1: Identifying Cloudbursts Events.....	43
3.1.1	Cloudburst Rainfall Analysis: Station vs TRMM data.....	48
3.2	Methodology .....	52
3.2.1	Composite Analysis: An Approach to Achieve Overall Goal of the Research.....	52
3.2.2	Significance t-test.....	52
3.2.3	Objective 2: Identification of Favorable Synoptic Conditions of cloudbursts .....	53
3.2.4.	Objective 3: Enhanced Northward Tropical-extratropical Interaction....	54
3.2.5	Objective 4: Role of Tropical Heating triggering Tropical-Extratropical Interaction during cloudbursts.....	56
<b>Chapter 4:</b>	<b>Cloudburst Synoptic Features: Composite analysis.....</b>	<b>58</b>
4.1.	Synoptic Climatology during July-August.....	58
4.2	Cloudburst Composite Analysis.....	60
4.2.1	Jet Streams and Upper-Level Troughs.....	61

4.2.2	Surface Synoptic Conditions.....	64
4.2.3	Upper-Level Potential Vorticity (PV) .....	69
4.2.4	Vertical Velocity.....	72
4.2.5	Significance of Synoptic Features.....	73
4.3	Conceptual Model of Cloudburst Mechanism: Tropical-Extratropical.....	78
<b>Chapter 5: Tropical-Extratropical Interaction Mechanism during Cloudburst...</b>		<b>85</b>
5.1	Northward Tropical-Extratropical Interaction .....	85
5.1.1	Local Hadley Cell Strength.....	85
5.1.2	Momentum Transport by Mean Circulation (local Hadley Cell).....	87
5.1.3	Momentum Transport by Transient Eddies.....	90
5.1.4	Momentum Transport by Stationary Eddies.....	92
5.1.5	Momentum Flux Divergence by Transient Eddies.....	93
5.2	Force balance analysis on tropical-extratropical interactions	
	during cloudbursts: Pressure gradient verses inertial forces.....	96
5.3	Upper-level Force Balance Analysis: Role of weak inertial	
	stability on cloudburst Mechanism.....	101
5.4	Role of monsoonal heating and eddy Shedding in triggering	
	favorable condition for cloudbursts.....	103
5.5	Discussion: Monsoonal heating as a forcing to bring favorable synoptic	
	conditions for cloudbursts through Eddy Shedding process .....	112
<b>Chapter 6: Conclusions and Future Work.....</b>		<b>115</b>
6.1	Conclusions.....	115

6.2	Limitations.....	117
6.3	Future Work.....	118
	<b>References.....</b>	<b>120</b>

## LIST OF FIGURES

Figure 1.1: Vertical structure of rainfall (mm/h) at 84.5E for (a) Pre-monsoon (Mar-May). (b) Monsoon (Jun-Aug). Dashed rectangle indicates southern slopes of the Himalayas. Gray line represents north-south Himalayan topography. (All the panels are from Shrestha et al. 2012)

Figure 1.2: Horizontal distribution of rainfall types during JJA: Difference between the occurrence of stratiform and convective rainfall events. The area enclosed by black oval represents the Central Himalayan Region (Nepal). (Figure from Shrestha et al. 2012)

Figure 1.3: Spatial distribution of convection during monsoon. a) Deep. b) Stratiform. (Both panels are from Houze et al. 2007)

Figure 2.1: Conceptual diagram of cloudburst mechanism in northwest India. a) Stage I: 06:30 LST Separate cells. b) Stage-2: 08:30 LST Merger cells and downpour. c) Stage-3: 12:30 LST Dissipation. All the panels are from Das et al. (2006).

Figure 2.2: Conceptual model demonstrating key meteorological element that led to cloudbursts in northwest India. Figure from Rasmussen and Houze (2012)

Figure 2.3: Hourly rainfall in Kulekhani Watershed, Central Nepal, 19-20 July 1993. Data from Shrestha (1998).

Figure 2.4: Mean Sea Level Pressure distribution July 1993. a) 18z, 18 Jul; b) 06z, 20 Jul; c) 18z, 20Jul; d) 06z, 21 Jul; e) 18z, 22 Jul. All the panels are from Dhital et al. (1993).

Figure 2.5: Echo top height of rain events. (a) active monsoon phase in Nepal; b) Jun-Aug climatology. Both panels are from Shrestha et al. (2012)

Figure 2.6: “Vaison-la-Romaine”, France heavy rainfall event synoptic situation at 00UTC 22Sep 1992. (a) Tropopause (2-PVU isosurface) from above; (b) from below; (c) Distribution of 500-150 hPa layer mean potential vorticity (shaded in PVU) and wind in vectors at 200 hPa; (d) 3-PVU isoline of 500-150 hPa layer mean potential vorticity (thick dash-dot pattern) superimposed upon 700 hPa wind (vectors), geopotential heights (thin solid line, 30m spacing) and ascent (shaded, in Pa/s). Alpine region outlined as a thick solid line. All the panels are from Massacand et al. (1998) with improved labeling.

Figure 2.7: 72-hour backward trajectories viewed from the south in 3 dimensions. Integration starts south of the Alps (mid-picture range) at  $t=0$  i.e. 12UTC Sep 22, 1992 for Vaison-la-Romaine (pink tracks), 00UTC Sep 24, 1993 for Brig (red), 00UTC Nov 06, 1994 for Piedmont (yellow), and 18UTC Sep 13 1995 for South Ticino (white).  $T \sim -18$  hours is marked in blue. Figure from Massacand et al. (1998).

Figure 2.8: Conceptual model of the key synoptic-scale features and processes for three categories PREs (a) Jet in ridge (JR); (b) Southwesterly jet (SJ); (c) Downstream confluence (DC). The gray contours denote the 200-hPa geopotential height, with the thick dashed black line marking the primary trough axis. The gray shaded regions represent 200-hPa wind speed [m/s; gray shade bar in (a)] and the “J” marks the 200-hPa wind speed maximum. The thin red and blue arrows represent 925-hPa streamlines associated with regions of warm and cold advection, respectively. The position of the surface front is shown in standard frontal notation, and the positions of the sea level pressure maxima and minima are marked by the “H” and the “L” symbols, respectively. The light green shading indicates the region with PW values >45 mm. The thick blue arrow represents a corridor of moist low-level flow. The dark green, gold, and orange shaded regions represent radar reflectivity thresholds of 20, 35, and 50 dBZ, respectively, associated with the PRE. The TC location is indicated by the tropical storm symbol. All panels are from Moore et al. (2013).

Figure 2.9: Regions of upper-level weak inertial stability or inertial instability and its role in MCS organization. (a) Two typical regions for the occurrence of mesoscale convective systems (MCSs; darkened regions). Contours are representative of the Montgomery streamfunction (height) on isentropic (pressure) surfaces. Lows and highs marked by L and H, respectively. The equation for isentropic relative vorticity  $\zeta_s$  is given in natural coordinates. The first term on the right-hand side is the shear term and the second is the curvature term, where  $V$  is the wind speed,  $n$  is a distance oriented normal to the streamline, and  $R_s$  is the radius of curvature of the streamlines. (b) Cross section in the  $y$ - $z$  plane showing the conceptual model of trajectories of air parcels in inertially stable and unstable regions. In the inertially stable region (right side), outflow material descends in the near environment, resulting in drying and warming. The region of inertial instability (left side) permits meridional accelerations of outflow material. The thick, shaded line is a momentum (M) surface typical of inertially unstable regions. The vertical shear vector is directed into the page. Both panels are from Blanchard et al (1998).

Figure 2.10: The dynamical response of the Gill model (Gill 1980) to asymmetric heating source (north of equator). (a) The surface wind field (vectors) and vertical motion field (contours, 0.3 interval: upward in north of equator); (b) The surface wind field and perturbation pressure (contours 0.3 interval). Both panels from are Gill (1980).

Figure 2.11: Day 15 perturbation streamfunction fields (zonal average removed) for equatorial heating on Dec-Feb zonal flow for upper-level. The contour interval is  $10 \times 10^5$   $m^2/s$ . The zero contour is dotted and negative contours are dashed. Figure from Jin and Hoskins (1995).

Figure 2.12: Eddy shedding experiment for f-plane for supercritical flow condition. The phases of shedding cycle ( $t=1$ ) at  $t=0.25$ ,  $t=0.5$ ,  $t=0.75$ ,  $t=1.0$ . Shading is absolute vorticity with an interval of  $0.025f_0$  between 0 and 1.575 (warm color: low vorticity and cold colors high vorticity). The inner circle marks the size of the imposed axisymmetric mass source (corresponding to heat source) and the outer circle marks the limit of the

corresponding axisymmetric divergent circulation. From Hsu and Plumb (2000).

Figure 2.13 Eddy shedding experiment for  $\beta$ -plane for supercritical  $\beta$  parameter. The phases of shedding cycle ( $t=1$ ) at  $t=0.25$ ,  $t=0.5$ ,  $t=0.75$ ,  $t=1.0$ . Shading is absolute vorticity with an interval of  $0.025f_0$  between 0 and 1.575 (warm color: low vorticity and cold colors high vorticity). The line contours are geopotential perturbation plotted with a contour of  $10\text{m}^2\text{s}^{-2}$ . Vectors denote the wind field. The inner circle marks the size of the imposed axisymmetric mass source (corresponding to heat source) and the outer circle marks the limit of the corresponding axisymmetric divergent circulation. From Hsu and Plumb (2000).

Figure 2.14: A snapshot of model output on Eddy shedding experiment for  $\beta$ -plane with critical  $\beta$  parameter but with heating function at various latitudes (various values of  $q$  parameter). Top: equivalent to mid-latitudes; Middle: equivalent to subtropics; Bottom: equivalent to near equator. Shading is absolute vorticity with an interval of  $0.025f_0$  between 0 and 1.575 (warm color: low vorticity and cold colors high vorticity). The line contours are geopotential perturbation plotted with a contour of  $10\text{m}^2\text{s}^{-2}$ . Vectors denote the wind field. The inner circle marks the size of the imposed axisymmetric mass source (corresponding to heat source) and the outer circle marks the limit of the corresponding axisymmetric divergent circulation. From Hsu and Plumb (2000).

Figure 2.15: Snapshot of model output on eddy shedding experiment for  $\beta$ -plane with high supercritical  $\beta$  parameter and heating function at between subtropics and near equator ( $q=0.5$ ). Shading is absolute vorticity with an interval of  $0.025f_0$  between 0 and 1.575 (warm color: low vorticity and cold colors high vorticity). The line contours are geopotential perturbation plotted with a contour of  $10\text{m}^2\text{s}^{-2}$ . Vectors denote the wind field. The inner circle marks the size of the imposed axisymmetric mass source (corresponding to heat source) and the outer circle marks the limit of the corresponding axisymmetric divergent circulation. From Hsu and Plumb (2000).

Figure 3.1: Station locations of the top ten maximum daily rainfall events in each region in Nepal during 1980-2008 along with topography. Cross: East region stations, Open circles: Central region stations, Stars: West region circles.

Figure 3.2: Distribution of daily maximum rainfall (mm) in Nepal during 1975-2008. Source: Prepared by Department of Hydrology and Meteorology, Nepal using Kriging Interpolation method in SURFER software.

Figure 3.3: Rainfall intensity during cloudbursts in Nepal. a) Hourly rainfall intensity Kulekhani, Central Nepal, 19-20 July 1993 from station data, b) 3-hour average rainfall intensity for five 21<sup>st</sup> century cloudburst events from TRMM data, c) Evolution of spatial distribution of 3-hourly rainfall intensity based on TRMM data during 30-31 of July 2003 cloudburst (LST means local standard time). (TRMM data: 3B42 version 7)

Figure 3.4: Spatial distribution of daily rainfall (mm) during the July 30-31 2003 cloudburst events. a) Rain gauge station data plot (size and color of circles represent

rainfall magnitude expressed in the color bar. b) Calculated from 3-hourly TRMM Data (3B42 version 7).

Figure 3.5: Comparison of the ratio of effective sample size to actual sample size for Leith (1973) and Bretherton et al. (1999) formulas as a function of  $r(\Delta t)$ . ( $r$  is autocorrelation coefficient and  $t$  is time step. Figure adopted from Hartmann (2016).

Figure 4.1: ERA-Interim July-Aug 18 UTC climatology (1980-2010). a) 200 hPa wind speed (shading, m/s), geopotential height (magenta contours, km), 28 m/s westerly jet core (black contour); b) 125 hPa total wind speed (shading m/s) and vectors, geopotential height (magenta contours, km), 35 m/s easterly jet core (black contour); c) surface total wind (vectors), mean sea level pressure 'MSLP' (magenta contours, hPa), approximate location of the monsoon trough axis (thick black dash line); d) same as (c) but zoomed over Nepal with MSLP at 1 hPa interval. D) 850 hPa GPT height pattern. Gray shading in a, b c and d represents the Tibetan Plateau and the Himalayas with elevation higher than 2000 m above sea level.

Figure 4.2 Evolution of composite upper-level geopotential height anomalies and wind speed anomalies from two days before (-2 day) to two days after (+2 day) the cloudbursts. a) Left panel is 200 hPa; b) Right panel is 125 hPa. 0 day is cloudburst day. Blue vectors: total wind (m/s), shading: wind speed anomaly (m/s), Magenta contours: Negative GPT anomaly (20 m interval), Green contours: Positive GPT anomaly (10 m interval), Yellow contours: 95% significance of geopotential anomaly, Red contours: 95% significance of wind speed anomaly, Black contours: climatological jet core (35 m/s, 125 hPa and 30m/s, 200 hPa), Cyan contours: Cloudburst jet core (35 m/s, 125 hPa and 30 m/s, 200 hPa), Gray thin contour: 2 km elevation above sea level.

Figure 4.3 Evolution of composite surface synoptic features from two days before (-2 day) to two days after (+2 day) the cloudburst day. 0 day is cloudburst day. a) Surface total wind vectors, MSLP (magenta contours at 2 hPa interval; b) Comparison of the cloudburst surface wind (blue vector) with climatology (black vector) zoomed over Nepal, MSLP (magenta contours at 1 hPa interval); Gray shading in (a) and (b) represents area with topography > 2 km above sea level and dashed line represents monsoon trough. c) Surface wind anomaly (vectors), MSLP anomaly (shading), 95% significant level (white contour); Gray thin contour: 2 km elevation above sea level.

Figure 4.4 Evolution of composite surface synoptic features from two days before (-2 day) to two days after (+2 day) the cloudburst day. 0 day is cloudburst day. a) Surface total wind vectors, geopotential height (GPH)(magenta contours km; b) Comparison of the cloudburst surface wind (blue vector) with climatology (black vector) zoomed over Nepal, GPH (magenta contours at 1 hPa interval); Gray shading in (a) and (b) represents area with topography > 2 km above sea level and dashed line represents monsoon trough. c) Surface wind anomaly (vectors), surface pressure anomaly (shading), 95% significant level (white contour); Gray thin contour: 2 km elevation above sea level,

Figure 4.5: Vertical cross-section (averaged over 85-86E) showing evolution of composite PV anomaly and vertical velocity from two days before (-2 day) to two days after (+2 day) events. 0 day is cloudburst day. a) Potential vorticity (PV), shading: PV anomaly, yellow contour: 95% significance level of positive PV anomaly above 300 hPa, Thick magenta: 1.5 PVU surface and thin magenta: 1 PVU surface, Blue contour: 1.5 PVU surface in climatology, b) Vertical velocity (shading), red contour: cloudburst 0.2 Pa/s, green contour: climatological 0.2 Pa/s, Thick magenta: PV of 1.5 PVU surface and thin magenta: 1 PVU surface, Blue contour: 1.5PVU (PV climatology); Cyan contour: 30 m/s jet cores (cloudburst), Black contour: 30 m/s jet cores (climatology), White shading represents topography.

Figure 4.6: Composite timeseries of synoptic features from 7 days before to 7 days after the cloudburst event. Averaging regions are given in Table 2. 0 day is the cloudburst day. a) Westerly trough, 200 hPa negative geopotential anomaly; b) WJ shift, 200 hPa positive wind speed anomaly; c) EJ shift, 125 hPa wind speed anomaly; d) Monsoon trough shift, MSLP anomaly over Nepal; e) upper-level PV anomaly, 300 hPa PV anomaly; f) Rising motion, 850-400 hPa vertical velocity anomaly (Pa/s). Red lines from (a) through (f) represent  $\pm 0.5$  standard deviation.

Figure 4.7: Timeseries of synoptic features for July 19-20 1993 cloudburst from 7 days before to 7 days after the cloudburst event: a) Westerly trough, 200 hPa negative geopotential anomaly; b) WJ shift, 200 hPa positive wind speed anomaly; c) EJ shift, 125 hPa positive wind speed anomaly; d) Monsoon trough shift, negative MSLP anomaly over Nepal; e) upper-level PV anomaly, 300 hPa PV anomaly; f) Rising motion, 600 hPa negative vertical velocity anomaly. Red lines from (a) through (f) represent  $\pm 1$  and  $\pm 2$  standard deviations. The list of the regions each of the variables is averaged over is in Table 3.

Figure 4.8: Conceptual diagram of interaction of synoptic features during cloudburst. a) Role of Upper-level trough in monsoon trough shift and moisture convergence towards the Nepal Himalayas; b) Role of Easterly and Westerly Jet shifts for enhanced vertical motion over the Nepal Himalayas; c) Upper-level PV anomaly associated with tropopause fold intensifying surface low and moisture convergence over the Nepal Himalayas.

Figure 5.1a: Mean meridional streamfunction ( $10^{11}$  Kg/s) at 5 longitudinal zones. Left panel: Climatology; Right panel: Cloudburst composite. Gray contour (blue shading): anticlockwise circulation, black contour (orange shading): clockwise circulation; Red contour: streamfunction 0; Green contour: northerly wind (m/s); Magenta: southerly wind (m/s); Purple with white mask: mountains

Figure 5.1b: Northward transport of westerly momentum by mean meridional circulation at 5 longitudinal zones (Shading in  $m^2 s^{-2}$ : Blue is southward  $< -50 m^2 s^{-2}$  and red is northward transport  $> 50 m^2 s^{-2}$ ). Left panel: Climatology; Right panel: Cloudburst composite. Gray contour: anticlockwise streamfunction cell ( $10^{11}$  Kg/s), black contour:

clockwise streamfunction cell ( $10^{11}$  Kg/s), Red contour: 0 streamfunction; Green contour: Easterly and Westerly Jets (m/s). Purple with white mask: mountains

Figure 5.1c: Northward transport of westerly momentum by transient eddies at 5 longitudinal zones (Shading in  $m^2 s^{-2}$ : Blue is southward  $<-50 m^2 s^{-2}$  and red is northward transport  $>50 m^2 s^{-2}$ ). Left panel: Climatology; Right panel: Cloudburst composite. Gray contour: anticlockwise streamfunction cell ( $10^{11}$  Kg/s), black contour: clockwise streamfunction cell ( $10^{11}$  Kg/s), Red contour: 0 streamfunction; Green contour: Easterly and Westerly Jets (m/s). Purple with white mask: mountains

Figure 5.1d: Northward transport of westerly momentum by stationary eddies at 5 longitudinal zones (Shading in  $m^2 s^{-2}$ : Blue is southward and red is northward transport). Left panel: Climatology; Right panel: Cloudburst composite. Gray contour: anticlockwise streamfunction cell ( $10^{11}$  Kg/s), black contour: clockwise streamfunction cell ( $10^{11}$  Kg/s), Red contour: 0 streamfunction; Green contour: Easterly and Westerly Jets (m/s). Purple with white mask: mountains

Figure 5.1e: Divergence of momentum flux divergence by transient eddies (Shading  $ms^{-2}$ : green is convergence and magenta is divergence). Left panel: climatology; Right panel: cloudburst composite. Gray contour: anticlockwise streamfunction cell ( $10^{11}$  Kg/s), black contour: clockwise streamfunction cell ( $10^{11}$  Kg/s), Red contour: 0 streamfunction; Green contour: Easterly and Westerly Jets (m/s). Purple with white mask: mountains

Figure 5.2a: Zonal cross section of Montgomery streamfunction gradient (MTG) at 370K for climatology (Shading). Black contours: Westerly and Easterly Jets. Red Contour: 0 MTG

Figure 5.2b: Zonal cross section of climatological inertial terms  $[(f+\zeta)\vec{u}]$  at 370K (Shading). Black contours: Westerly and Easterly Jets. Red Contour: 0 Inertial term.

Figure 5.2c: Zonal cross section of climatology of force balance ratio (FB-ratio) at 370K (Shading). White contour: FB-ratio=1. Westerly and Easterly Jets

Figure 5.2d: Climatology of meridional variation force balance ratio (FB-ratio) at 370K for mean 80:90E and mean 90:100E.

Figure 5.2e: Zonal cross section of time evolution of force balance ratio at 370K for cloudburst composites (shading) from -6day to +6day. 0day is the cloudburst day. White contour: FB-ratio=1. Westerly and Easterly Jets

Figure 5.2f: Meridional variation force balance ratio (FB-ratio) at 370K for cloudburst composites averaged for longitudes 80:90E and mean 90:100E.

Figure 5.3a: Climatological pattern of  $\alpha [(Q^2-A^2-B^2-D^2-2\beta*u)x0.5]$  in  $s^{-2}$  at 370K given by Eq. 5, Chapter 3. ( $\alpha$  is equivalent to inertial frequency)

Figure 5.3b: Time evolution of  $\alpha$   $[(Q^2 - A^2 - B^2 - D^2 - 2\beta \cdot u) \times 0.5]$  in  $s^{-2}$  at 370K given by Eq. 5, Chapter 3.  $\alpha$  is equivalent to inertial frequency) at two-day interval from -6day to +4day for the cloudburst composite (shading). Green contours: Easterly and Westerly Jets (m/s)

Figure 5.4a: Dynamic response of tropical heating (Jul-Aug) climatology. Green contours: OLR minima (190-200  $w/m^2$ ) representing tropical heating; Purple contours: Montgomery Streamfunction high at 370K; Blue contours: monsoon trough (low pressure) at 850 hPa; Black contours: Easterly and Westerly Jets; Shading: PV in PVU; Yellow contour: 1.5 PVU; White contour: 2 PVU.

Figure 5.4b: Jul-Aug Climatology of 500 hPa vertical velocity (Shading), 370K wind vectors and Montgomery Stream function high (Purple contours). Cyan contour maximum rising motion centers

Figure 5.4c: Time evolution showing westward eddy shedding process of upper level high in response to tropical heating for the cloudburst composite from -7day to -2day. Green contours: negative OLR anomaly (-10 to -30  $w/m^2$ ) representing tropical heating; Purple contours: Montgomery Streamfunction high at 370K; Blue contours: monsoon trough (low pressure) at 850 hPa; Black contours: Easterly and Westerly Jets; Shading: PV in PVU; Yellow contour: 1.5 PVU; White contour: 2 PVU. Continuation to Figure 5.4d.

Figure 5.4d: Continuation of Figure 5.4c. Time evolution showing westward eddy shedding process of upper level high in response to tropical heating for the cloudburst composite from -1day to +4day. Green contours: negative OLR anomaly (-10 to -30  $w/m^2$ ) representing tropical heating; Purple contours: Montgomery Streamfunction high at 370K; Blue contours: monsoon trough (low pressure) at 850 hPa; Black contours: Easterly and Westerly Jets; Shading: PV in PVU; Yellow contour: 1.5 PVU; White contour: 2 PVU

Figure 5.4e: Time evolution showing westward eddy shedding process of upper-level low PV (1.5 PVU) and wind vectors at 370K in response to tropical heating for the cloudburst composite from -7 day to +4day Shading: PV in PVU; Yellow contour: 1.5 PVU; White contour: 2 PVU; Purple contours: Montgomery Streamfunction high at 370K; Blue contours: monsoon trough (low pressure) at 850 hPa;

Figure 5.5: Snapshot (0 day cloudburst composite) of westward eddy shedding process of upper-level low PV (1.5 PVU) at 370K in response to tropical heating. Shading: PV in PVU; Yellow contour: 1.5 PVU; White contour: 2 PVU; Purple contours: Montgomery Streamfunction high at 370K; Blue contours: monsoon trough (low pressure) at 850 hPa. Green contour: 3-day (-7d to -5d) mean negative OLR anomaly (-10 to -30  $w/m^2$ ); Cyan contour: 3-day (-4d to -2d) mean negative OLR anomaly (-10 to -30  $w/m^2$ ).

## LIST OF TABLES

Table 1: Daily rainfall with dates recorded during the top ten “cloudburst” events in 3 regions of Nepal, ordered by highest rainfall amount in each region.

Table 2: Description of six synoptic features of cloudburst composite, timeseries of which are shown in Figure 4.8

Table 3: Description of six synoptic features of individual cloudburst events along with regions averaged, timeseries of which are shown in Figure 4.7 for the 1993 event

Table 4: Status of anomalies of cloudbursts synoptic features compared to daily climatological standard deviations for the individual events.

## ABSTRACT

“Cloudbursts” are the most intense rainstorms in the Himalayan Region during the monsoon season. This study is focused on two questions: 1) “What are the favorable synoptic features of the cloudbursts?” and 2) “What triggers the favorable condition for the cloudbursts?” To address these two questions, this study investigated the synoptic conditions and possible upper-level tropical–extratropical interaction during the cloudbursts in the Nepal Himalayas using composite analysis of ERA-Interim data for ten cloudburst events in the central Nepal.

Composite analysis suggested four significant synoptic conditions during the cloudbursts: 1) an upper-level extra-tropical westerly trough over the northwest of the Nepal Himalayas, 2) a shift of the westerly and easterly jets towards the Himalayas, 3) an upper-level positive potential vorticity anomaly, associated with a steep tropopause fold around the westerly jet over the Himalayas north of the cloudburst region, and 4) at the surface, a northward shift of the monsoon trough towards the Nepal Himalayas and the extension of westerly surface wind flow directly from the Arabian Sea to the Himalayas in the “cloudburst” region. These conditions are accompanied by a strong rising motion, from the surface to 300 hPa over the southern slopes of the Nepal Himalayas, indicating deep convection in the cloudburst region.

The study concludes that cloudburst events begin when an anomalous convective event, external to the monsoon, opens a breach in the inertial wall that normally prevents the monsoon outflow from being directed across the Himalayas.

Composited analysis suggested that no single type of anomalous event causes the breach, although evidence suggests that anomalous convective activity occurring north of the usual location of monsoon convection was often the cause. The resulting convective heating anomaly seems to initiate an eddy-shedding process aloft in the outflow layer of that convection. This in turn is shown to be associated with the weakening of the inertial wall north of the Nepal Himalayas, upsetting the inertial force balance in the upper atmosphere that typically traps potential energy built up by the monsoon outflow in the tropics that would typically flow into the upper-level easterly jet. This resulting breach in the inertial wall north of the normal monsoon activity enables the poleward pressure gradient force in the upper troposphere over India to push the upper tropospheric monsoon outflow dome poleward leading to an associated diversion of the low level monsoon flow poleward across the Himalayas resulting in a cloudburst as the moist monsoonal plume is forced over the high terrain.

# Chapter 1

## Introduction: Cloudbursts Overview and Issues

### 1.1 Limited Meteorological Understanding

Cloudbursts are the most catastrophic extreme weather events affecting the southern slopes of the Himalayas (Nepal, India and Pakistan) during the Indian monsoon season. These events are localized intense orographic-convective rainfall episodes triggering devastating flashfloods, landslides and debris-flows in the steep terrains of the Himalayas (Das et al. 2006; ISET-N and ISET 2009). A cloudburst on July 19-20, 1993 in the central Nepal was the most catastrophic cloudburst event in recorded history. This event dropped 540mm/day with maximum intensity of 65mm/hr (ISET-N and ISET 2009). This total daily rainfall was almost half of the total for the monsoon season and approximately 5400% of the mean daily active monsoon rainfall in this location in Nepal (~10 mm/day estimated from Figure 11a in Shrestha et al. 2012). This single event claimed about 1300 lives and left a devastating economic impact in central Nepal (Dhital et al. 1993). Recently, another major cloudburst on August 5-6, 2010 in the West Indian Himalayas claimed 255 lives (Thayyen et al. 2013).

Typically, these events tend to but not always occur during the monsoon break phase in India, suggesting a critical shift of the usual monsoon flow pattern that gives rise to the cloudburst events. For example, the cloudburst of July 1993 was accompanied by the monsoon break in India (as defined by Rajeevan et al. 2010). Monsoon breaks in India are usually associated with the active monsoon phase in the Himalayas (Rajeevan et al. 2010; Shrestha et al. 2012). However, as a Meteorologist in Nepal, I noticed that although monsoon breaks in India and active monsoon in the Himalayas occur almost every year,

cloudbursts do not. This suggests a different monsoon dynamics of the cloudbursts in the Himalayas than monsoon breaks in India and active monsoon phase in the Himalayas.

Understanding this anomalies monsoon dynamics that lead to the formation of cloudbursts is a pre-requisite to improving their prediction and reducing the human loss in the region. Despite their catastrophic impact on the human lives and the socio-economy in the Himalayan countries, only little attention is given to the meteorological study of the “cloudbursts” while the focus of the study was limited to the damage and flood assessment.

The limitation in understanding cloudbursts phenomena is of two fold. First is the lack of availability of meteorological in situ data on the cloudbursts in the Himalayas. Because of the sparse station network for rainfall intensity and other meteorological variables (e.g. upper air), not enough *in situ* data are available on the cloudburst events in the Himalayas. This limits the study of the cloudburst phenomena.

Secondly, there is only limited number of studies on meteorological aspects of the cloudbursts in the Himalayas. Two recent studies discussed mechanisms for the intensification of convection during “cloudbursts” in the Indian Himalayas. Das et al. (2006) showed that the merging of two convective systems over terrain with favorable meridional wind shear was responsible for the intensification of the convection during the “cloudburst” of July 2003 in Shillagarh Village in the northwest Himalayas in India. Rasmussen and Houze (2012) concluded that the heavy rainfall episode in Leh Village in the western Indian Himalayas, which the Indian Meteorological Department identified as a “cloudburst,” was associated with upstream regeneration of convection and the

westward propagation of the MCS towards Leh Village via a mid level easterly jet and a continuous low-level moisture source. Both these studies showed the important roles of the upper-level flow and the low-level moisture convergence over mountains for the intensification and the upstream regeneration of convection during the “cloudbursts.” *However, these studies did not discuss how the atmospheric conditions during “cloudbursts” differ from and fit into normal monsoonal flow.*

While catastrophic flash floods around the world are triggered by very heavy rainfall from convective systems, the meteorological phenomena behind these convective systems can differ (Maddox et al. 1978). The causative and organizing features of intense convection causing flash floods may range from quasi-stationary convective systems, to the effects of terrain to tropical-extratropical interaction along a deep tropopause fold or in the equatorward jet entrance region in the westerly waves (Maddox et al. 1978; Doswell, C. A., III 1985; Galarneau et al. 2010; Bosart et al. 2012; Moore et al. 2013). In the case of the “cloudbursts” over the Nepal Himalayas, the basic synoptic conditions are still not well understood and have not been documented in the peer-reviewed literature. *Therefore, the main goal of this study is to understand the synoptic conditions and contributing dynamics of the cloudburst mechanism in the Nepal Himalayas.*

## **1.2 Scientific Issues and Research Questions**

### **a. What are the Favorable Synoptic Conditions for Cloudbursts?**

Dhital et al. (1993) reported that the cloudburst events are accompanied by the thunder and lighting activities. Personal communication with local people in the cloudburst hit regions of Nepal confirmed that the rainfall events during the cloudbursts were accompanied by the strong thunder and lightning. This clearly suggests that these events

are associated with the deep convective systems. However, previous studies and documentation suggested have suggested that deep convective systems are not common in the Nepal Himalayas during the monsoon season ( Houze et al. 2007; Rasmussen and Houze 2012; Shrestha et al. 2012).

In the Nepal Himalayas, most rainfall systems are associated with orographic lift. They can be subdivided into convective types associated with low-level instability in the pre-monsoon season (Mar-May) and stratiform types associated with the orographic uplift of moist stable southerly flow during monsoon season (Shrestha et al. 2012). The dominance of low echo-top heights during the monsoon season compared with the dominance of high echo-top heights during pre-monsoon season in Figure 1.1a is the evidence of stratiform rain events compared to the convective rain events in the monsoon season (Figure 1.1b). Similarly, the difference between occurrences of stratiform and convective rainfall events showed dominance of stratiform rain events compared to the convective rain events (Figure 1.2). Moreover, Houze et al. (2007) suggested that stratiform rain systems tend to be more frequent overall compared with convective rain systems in the foothills of the central Himalayas (Figure 1.3).

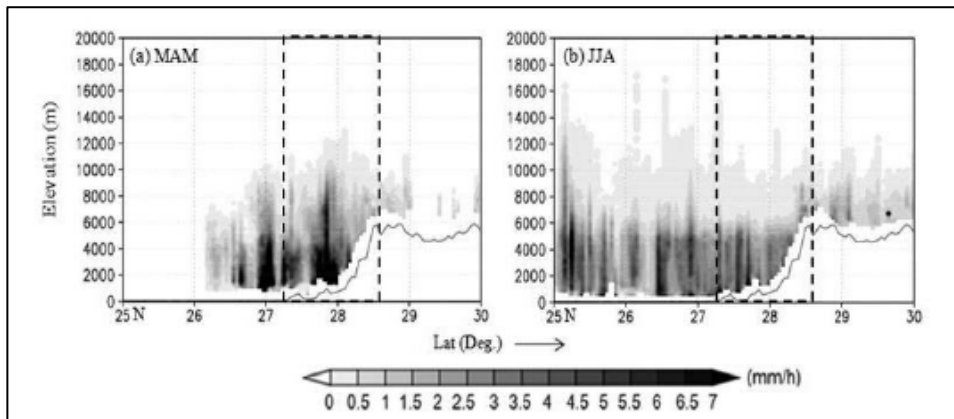


Figure 1.1: Vertical structure of rainfall (mm/h) at 84.5E for (a) Pre-monsoon (Mar-May). (b) Monsoon (Jun-Aug). Dashed rectangle indicates southern slopes of the Himalayas. Gray line represents north-south Himalayan topography. (All the panels are from Shrestha et al. 2012)

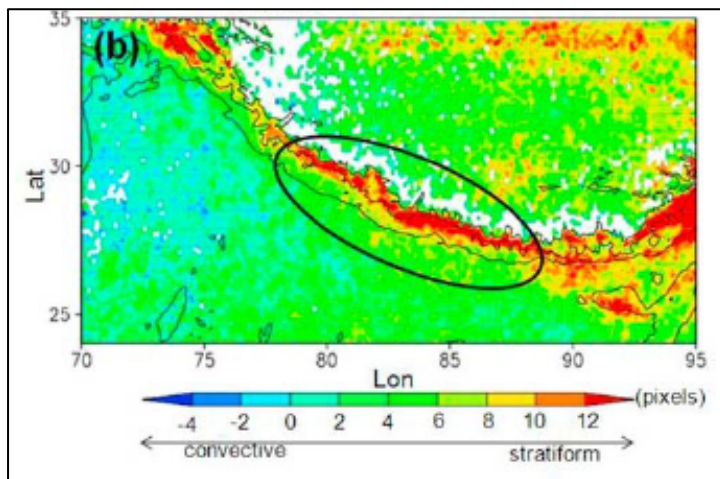


Figure 1.2: Horizontal distribution of rainfall types during JJA: Difference between the occurrence of stratiform and convective rainfall events. The area enclosed by black oval represents the Central Himalayan Region (Nepal). (Figure from Shrestha et al. 2012)

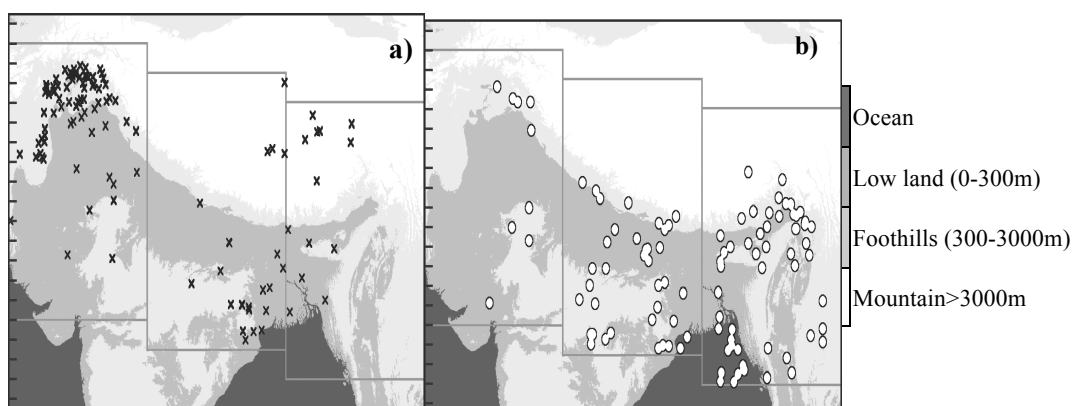


Figure 1.3: Spatial distribution of convection during monsoon. a) Deep. b) Stratiform. (Both panels are from Houze et al. 2007)

The dominance of stratiform and persistent rain system during the monsoon season in the

Nepal Himalayas was attributed to the atmospheric stability (Shrestha et al. 2012). Authors found that average atmospheric instability [difference of equivalent potential temperature in the layer ( $\theta_{e925} - \theta_{e600}$ ) between 600 and 925 hPa] is smaller during the monsoon season (14-18K) than during the pre-monsoon rain events (~18-28K). They suggested that precipitation systems in the pre-monsoon season are mostly triggered by strong atmospheric instability, while persistent rainfall in the summer monsoon season are due the mechanical uplift of stable and sufficiently moist low-level southeasterly flow.

Not only during the normal monsoon conditions, as mentioned above, but also during extreme monsoon weather events, heavy rainfall episodes in the Nepal Himalayas are attributed commonly to the broad stratiform type convective systems and sometimes to the wide intense convective systems (with convective cores of 40 dBZ extending over  $>1000 \text{ km}^2$  below 4.5 km) (Romatschke et al. 2010). The broad stratiform type convective rain systems are associated with the low-pressure systems and monsoon depressions over the Bay of Bengal that move towards land. They feature an orographically uplifted flow in the surrounding mountains, producing maritime character convective systems (Houze et al. 2007). The wide convective cores rain events are associated with the convergence of moist southerly flow with the downslope flow during the night driven by radiative cooling of the elevated terrain Romatschke et al. (2010). Romatschke et al. (2010) attributed the absence of deep intense convective systems (40 dBZ echos reaching an altitude of higher than 10 km) in the Nepal Himalayas to the unfavorable upper-level conditions, i.e. lack of upper-level dry cap to boost low-level instability. This reasoning on instability is consistent with the findings of Shrestha et al (2012) on the low atmospheric instability during monsoon season in the Nepal

Himalayas.

These studies suggest that the deep intense convection as defined in Houze et al (2007), are environmentally less favorable and less common in the Nepal Himalayas. This raises the first research question: *What kind of synoptic features and their interaction with the topography favor the localized flash-flood-generating deep convective systems, the “cloudbursts” in the Nepal Himalayas?*

**b) What is Mechanism Triggers Favorable Conditions for the Cloudbursts?**

A number of studies indicated extreme weather events in the tropics can be triggered due to the tropical-extratropical interaction [e. g. Riehl (1977); Kiladis and Weickmann (1992a); Knippertz (2007); Ding and Wang (2007) ; Hong et al (2011)] . These studies showed that the intrusion of eastward moving upper-level troughs originating in the extratropics could trigger deep convection in the tropics. It is noteworthy that “cloudbursts” occur over the foothills of the Himalayas (the northernmost edge of the South Asian monsoon) between the mid-latitude upper-level westerly jet to the north and monsoonal synoptic features (like tropical upper-level easterly jet and monsoon trough) to the south. As noted by Houze et al (2007), the presence of upper-level westerlies leading to the deep convective storms in the western Himalayas, there is the possibility of southward migration of westerlies in the central Himalayas (Nepal) as well. Therefore, this possibility raises following two questions:

- i) *Are the cloudbursts in the Nepal Himalayas associated with the tropical-extratropical interaction?*
- ii) *If so, what mechanism triggers tropical-extratropical interaction that favors the cloudbursts?*

### **1.3 Hypothesis of the Study**

To address above-mentioned research questions in understanding the cloudburst synoptic characteristics and its mechanism, this study proposes following three hypotheses:

1. Synoptic conditions during the cloudbursts are significantly different from the normal monsoon climatology.
2. Anomalous tropical-extratropical interaction takes place during the cloudbursts events compared to the normal monsoon climatology.
3. Anomalous monsoonal heating is associated with a series of synoptic events that favors the interaction between monsoon flow and the extratropics and trigger cloudburst activity along the southern slopes of the Nepal Himalayas.

### **1.4 Objective of the Study**

This study has following objectives to address the research gap on the cloudbursts in the Nepal Himalayas:

Objective 1: To identify cloudburst events using rainfall data.

Objective 2: To identify the significant synoptic features of the cloudburst events.

Objective 3: To analyze anomalous tropical-extratropical interaction during the cloudbursts.

Objective 4: To identify a possible mechanism that could trigger a series of synoptic events that favors tropical-extratropical interaction during the cloudburst events.

### **1.5 Road Map**

This dissertation is divided into two Parts:

Part I covers two chapters, Chapter 1 and Chapter 2, that basically presents background of this research. In Chapter 2 literature review on the meteorological characteristics on cloudbursts in the Himalayas and on the theories used to explain tropical-extratropical interaction were discussed.

Part II consists four Chapters, Chapter 3 to Chapter 6 that presents research methods, research results and conclusions. . Chapter 3 discusses methodology and data used for this research. Chapter 4 presents the results and discussion on significant synoptic characteristics of the cloudbursts to meet objective 3. It also presents the time conceptual model on cloudburst mechanism. Chapter 5 presents two aspects. First it presents results that suggest the anomalous tropical-extratropical interaction to fulfill the objective 3. Second, it discusses results to show anomalous tropical heating triggers the mechanism that favors tropical-extratropical interaction that leads to the cloudbursts to fulfill the objective 4. Finally Chapter 6 presents research findings and limitations of this research and potential future research.

## **Chapter 2**

### **Review: Extreme Events in the Himalayas, Synoptic Features of Extreme Events, and Theories of Tropical-Extratropical Interaction**

This section consists of the literature review of cloudbursts in the Himalayas and other extreme rainfall systems in the Himalayas during monsoon. The purpose of this review is to layout available information on the atmospheric characteristics of extreme events during the monsoon season in the Himalayas and on the mechanisms responsible for the extreme rainfall events around the globe. Second, it discusses possible theories and methods used to understand tropical-extratropical interaction.

#### **2.1 Meteorological Features of Extreme Monsoon Rainfall Events in the Himalayas**

##### **2.1.1 Cloudburst Characteristics in the Himalayas**

A limited amount of literature is available on the meteorological analysis of the cloudburst in the Indian Himalayas. Das et al. (2006) simulated cloudburst in the Shillagarh Village the northwest India using MM5 model. They focused on impact of horizontal resolution and cloud microphysics in simulating cloudbursts. They found that while the model at 30km grid resolution was able to forecast cloudburst rainfall in advance of 24 hour, the location of the storm was off by tens of km and ahead of time. With the increase in resolution the model overestimated rainfall but improved timing and provided detail thermodynamic structure of the cloudburst. The authors proposed a conceptual model (Figure 2.1a) of this cloudburst mechanism in the Shillagarh Village using their thermodynamic results from MM5. This model highlights that how the upper-level flow help in the merger of the convective cells in the presence lower-level moisture surge leading to the cloudbursts in the region. While this study presented a potential application of the numerical models in predicting cloudbursts, it also highlights the

limitation of TRMM data and necessity of dense network in situ data in understanding cloudburst in the region.

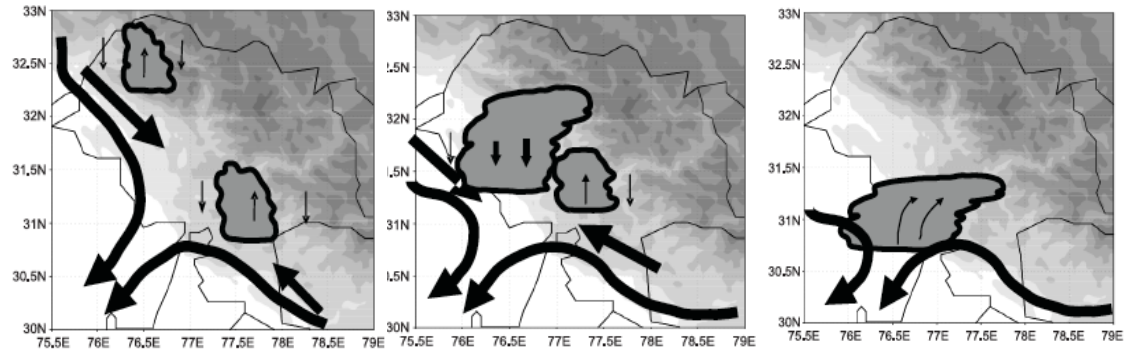


Figure 2.1: Conceptual diagram of cloudburst mechanism in northwest India. a) Stage-1: 06:30 LST Separate cells. b) Stage-2: 08:30 LST Merger cells and downpour. c) Stage-3: 12:30 LST Dissipation. All the panels are from Das et al. (2006).

Second study was by Rasmussen and Houze (2012) that showed the role of the mid-tropospheric easterly jet from the Tibet in the organization of convections that lead to heavy rainfall episodes in the Leh Village of Western Himalayas in India. They provided a conceptual model demonstrating the meteorological dynamics leading to the heavy rainfall episodes in Leh Village (Figure 2.2). This easterly jet helped the convections to organize and propagate west from the Tibet to the Leh village. No such study, especially in the upper-level conditions, is available for the Nepal Himalayas.

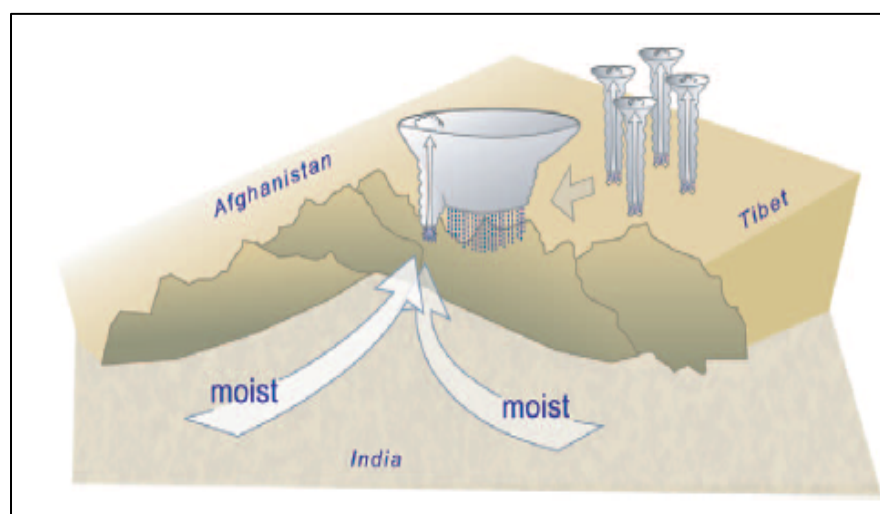


Figure 2.2: Conceptual model demonstrating key meteorological elements that lead to cloudbursts in northwest India. Figure from Rasmussen and Houze (2012)

Detailed meteorological study of the cloudbursts in the Nepal Himalayas is also scarce, and studies of upper air synoptic conditions are simply not available. Daily rainfall data is the only in situ information available for most of the cloudbursts in the Nepal Himalayas. The July 19-20, 1993 cloudburst in the central Nepal is the only cloudburst event that was studied widely from meteorological perspective, though limited to surface data. This event provided a unique situation for researchers to understand cloudburst in Nepal not only due to the catastrophic nature of damage, but also because it occurred in a region that was equipped with a number of automatic agro-meteorological stations. According to the post disaster field report (Dhital et al. 1993), high intensity rainfall with thunderstorms started at around 2pm (LST) on July 19 and continued till 7pm over Daman, the southwest mountain peaks of Kulekhani watershed, Nepal. No automatic data was available at Daman. Unprecedented high intensity rainfall with thunderstorms and lightning occurred again at about 10pm (LST) in this watershed, causing huge landslides and debris flow and the continued throughout the night. Figure 2.3 shows hourly rainfall recorded at Tistung, southern slope of northwestern peak of

Kulekhani watershed. This is the station that recorded highest rainfall intensity and daily accumulation during the event. In this location rainfall started at around noon of 19 July, with rainfall intensity increasing (50 mm/hr at 5pm) and reached maximum intensity (65mm/hr) at around midnight. The total daily maximum rainfall recorded was 20 July (9am 20 July) at this station and was 540mm. Similar rainfall pattern was recorded in valley floor of this watershed (Dhital et al. 1993). This report also studied evolution of surface pressure during the event. Figure 2.4a-e shows the MSLP evolution from Jul 18-22, 1993. The surface map of July 19 was missing. The low pressure deepened to 996mb on 0060Z -1800Z, 20 Jul over Nepal. Since maximum rainfall was on Jul 19, the sea level pressure must be lower than 996mb during height of the storm. These figures clearly depict the shift of monsoon trough towards Nepal between 18 and 22 July. The report solely attributed 1993 cloudburst event to the northward shift of monsoon trough.

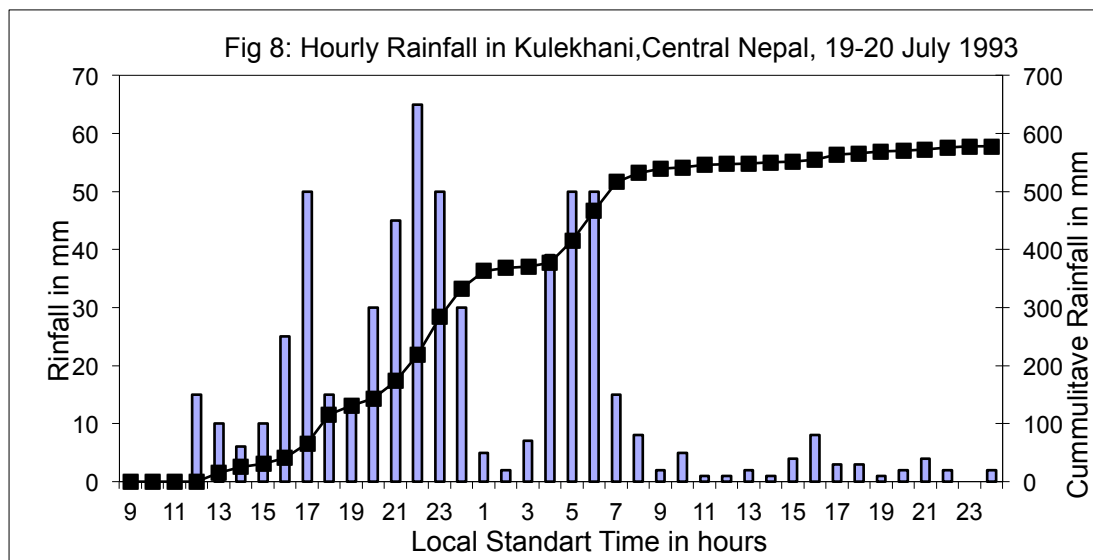


Figure 2.3: Hourly rainfall in Kulekhani Watershed, Central Nepal, 19-20 July 1993. Data from Shrestha (1998).

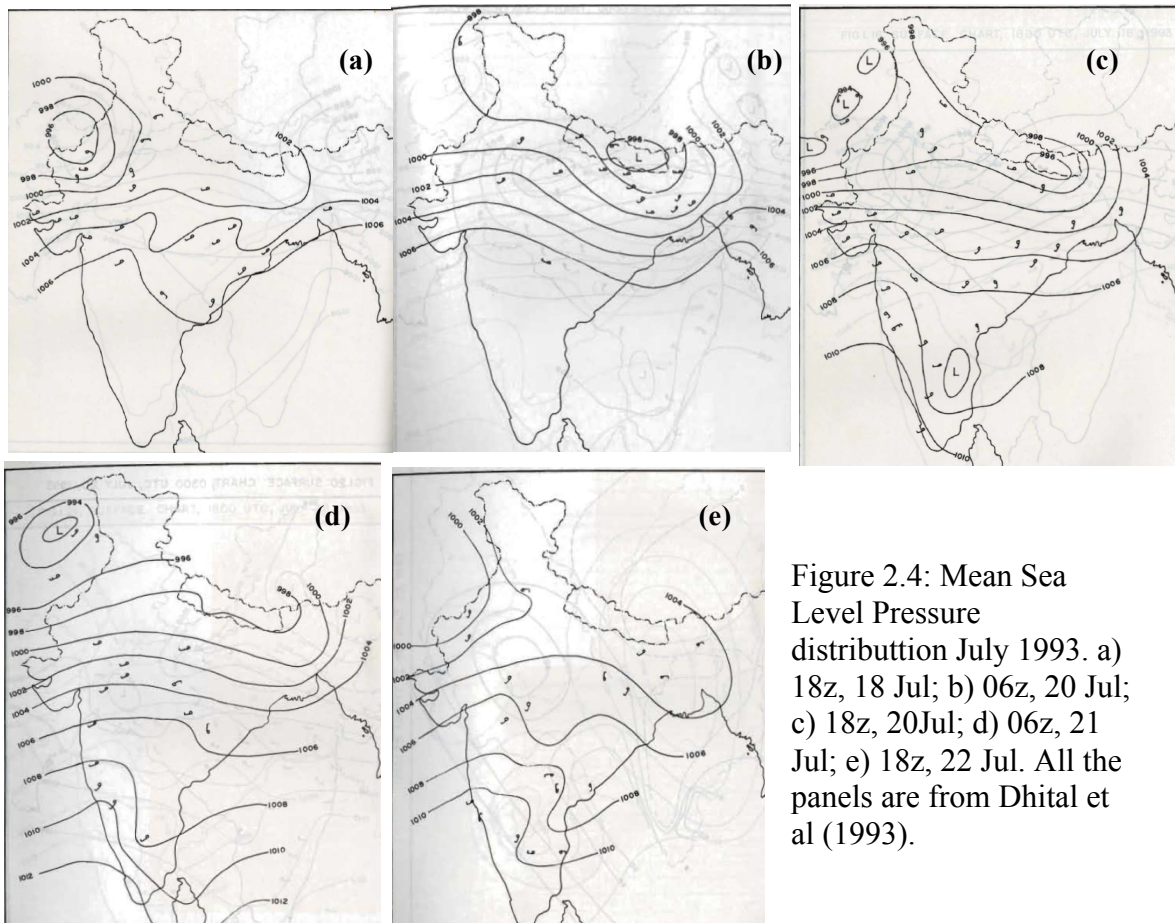


Figure 2.4: Mean Sea Level Pressure distribution July 1993. a) 18z, 18 Jul; b) 06z, 20 Jul; c) 18z, 20 Jul; d) 06z, 21 Jul; e) 18z, 22 Jul. All the panels are from Dhital et al (1993).

### 2.1.2 Other Extremes Rainfall Events in Nepal

#### a. Active monsoon in the Himalayas and its association with monsoon break in India

Active monsoon are the most common extreme rainfall events in the Himalayas that occur every year during the monsoon season. The South Asian monsoon has intra-seasonal variability of active periods and break periods that are associated with the latitudinal oscillations of the monsoon trough in the Gangetic plain of India (Ramaswamy 1962). Active monsoon in the Himalayas are associated to the northward shift of the monsoon trough over the foothills of the Himalayas and monsoon break in central India (Ramaswamy 1962; Rajeevan et al 2010). Though there is a long history on the study of monsoon break in India and active monsoon in the Himalayas occurs simultaneously with

monsoon break in the Himalayas, the past studies mainly focused on the atmospheric conditions in the central India and very little is available that are focused on the Himalayas. This section first discusses the past literature on active monsoon in Nepal and then it presents available information on synoptic aspects of monsoon break in India.

Few studies have conducted on the rainfall and synoptic characteristics of active monsoon (active phase) of monsoon in Nepal (Singh and Nakamura 2010; Shrestha et al 2012). These two studies defined active monsoon (active phase) as the period when daily rainfall is greater than 0.5 times the July-August standard deviation in the foothills of the Nepal Himalayas for at least 3 consecutive days. By definition active monsoon are widespread and persistent rain event while cloudbursts are localized high intensity rain events and thus provide some insight on the difference between two events.

Singh and Nakamura (2010) used TRMM TRMM/3B42 and TRMM/PR data to study active monsoon in Nepal Himalayas. They found that during wet period average daily rainfall is about 3.64mm/day and mean rain intensity is more than 0.3 mm/h. They also suggested that stratiform rain events are more frequently during wet periods than during dry periods, while the opposite was true for convective rain events. Shrestha et al (2012) used the 11-year (1998–2008) high-spatial resolution TRMM PR 2A25 near-surface rainfall data to study rainfall characteristics in relation with elevation during active spells in the Nepal Himalayas. They found that during the wet period the daily rainfall reached 24 mm/day over the sub Himalayan region (500–1,200 m AMSL), which is significantly higher than the mean monsoon daily rainfall (13 mm/day) whereas over lesser Himalayan region (1,200–3,000 m AMSL) mean daily rainfall is about same as the mean monsoon daily rainfall. This shows that by the amount of daily rainfall during active monsoon are

much lower than the cloudburst events

Figure 2.5 shows the echo-top height of rain events during active monsoon and monsoon climatology from Shrestha et al (2012). The echo-top height of intense rain events was similar to that of monsoon climatology. The authors attributed active monsoon to the abundant and above normal moisture supply in the lower atmosphere favoring easy triggering of convection when the moist flow encounters mountain ranges. The authors suggested that dynamical mechanism of rain events during the active monsoon and normal monsoon is same; in the sense of upliftment of moist layer by mountain but the availability of the amount moisture supply in the lower troposphere is higher during the active monsoon. The abundant moisture convergence during active monsoon is associated with the monsoon trough shift to the foothills of the Himalayas.

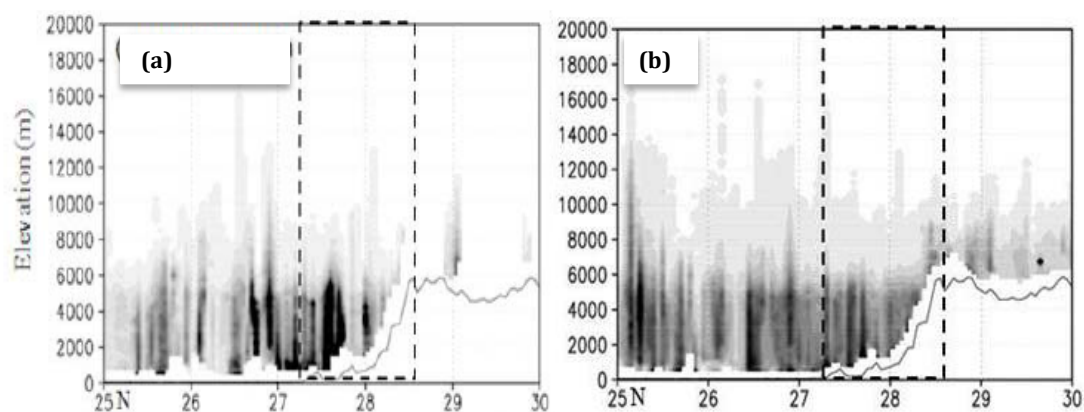


Figure 2.5: Echo top height of rain events. (a) Active monsoon during composite in Nepal; b) Jun-Aug climatology. Both panels are from Shrestha et al (2012)

The above studies on active monsoon in Nepal did not cover the upper-level conditions during the active monsoon. Active monsoon over the Himalayas also coincide with monsoon breaks in India (Rajeevan et al. 2010; Ramaswamy 1962). This association helps to draw some insight on upper-level condition during active monsoon from the studies on monsoon break in India. Main synoptic features during monsoon breaks found by previous studies (Ramaswamy 1962; Ramamurthy 1969; Krishnamurti and Bhalme 1976) are: northward shift of monsoon trough towards the foothills of the Himalayas, surface westerly flow from the Arabian Sea to the foothills of Himalayas, shifts of westerly and easterly upper-level jets closer and intrusion of upper-level (500-200hpa) extratropical wave towards Himalayas at around 65E. First two features are also discussed Shrestha et al (2012) as a synoptic changes during the active monsoon in Nepal. While there are no studies done on the extratropical wave during active monsoon in Nepal, the presence of upper-level trough over the Himalayas during monsoon break in India suggests the possibility of influence of upper-level wave during the active monsoon in Nepal. This suggests a possibility of tropical-extratropical interaction in the Nepal Himalayas.

#### **b. Monsoon Depressions**

Northwestward/northward moving monsoon depression from the Bay of Bengal is another extreme rainfall system in the Nepal Himalayas. A monsoon depression is a low pressure system in the Bay of Bengal with surface winds in cyclonic circulation with speeds between 32-59 km/h. Its pressure gradient extends from the center out to a radius of about 250 km ranges between 5 to 13 hPa (Sikka 1977). These depressions mostly travel to the northwest along the monsoon trough over the Indian subcontinent (Mooley

1973; Sikka 1977). From its formation in the Bay of Bengal to on its northwestward track, the easterly flow of this system converges in the mountain slopes of the Nepal Himalayas and produces heavy rainfall with the broad stratiform system (Romatschke et al 2010; Houze et al 2007).

In summary, the past studies showed that the rainfall pattern during cloudbursts is different from those that normally occur during the monsoon season in the Himalayas. Previous also suggested that there are some similarities between surface conditions during the cloudburst event and active monsoon, especially the northward shift of monsoon trough.

## **2.2 Synoptic Signatures of Extreme Rainfall Events**

While catastrophic heavy rainfall events around the world are triggered by the convective systems, the meteorological phenomena behind these convective systems can differ (Maddox, et al 1978). The causative and organizing features of intense convection causing heavy rainfall and flash floods have been attributed to a wide variety of influences including quasi-stationary convective systems, training of convection, the effects of terrain and, tropical-extratropical interaction (Maddox et al. 1978; Miller 1978; Doswell, C. A. III 1985; Galarnau et al. 2010; Bosart et al. 2012; Moore et al. 2012; Peters and Roebber 2014). The following few subsections discuss various synoptic mechanisms leading extreme rainfall events.

### **2.2.1 Quasi-stationary Upper-level System**

Lin et al. (2001) pointed out that one of the main ingredients for catastrophic rainfall events in US, Europe and East Asia was the existence of a quasi-stationary convective

system. Maddox et al. (1978) and Doswell (1985) found that Big Thompson flood 1976 was due to the quasi-stationary convective system. These events were triggered by a quasi-stationary negatively tilted upper-level ridge west of the flooding region for 3-4 hours, which allowed regeneration of cells in the southeast flank and moved in the near stationary system. The storm complex developed when conditionally unstable air masses pushed upslope in the higher terrain. Lower pressure west of the storm areas enhanced the easterly upslope flow. Studies showed that upper-level near quasi-stationary ridge prevented the storm from moving northward/eastward and helped regeneration of the cells causing catastrophic events. Similar synoptic conditions were also noted during the devastating Rapid City, South Dakota, flood along the eastern slopes of the Black Hills in 1972, during the flood event in Fort Collins, Colorado, in 1997, and during the flash flood event of Madison County, Virginia, in 1995 (Pontrelli et al. 1999). Similarly, Valero et al (1997) attributed heavy rainfall event in southeastern Iberia, Spain in 1993 to the slow moving surface front and upper-level blocking high and Miller (1978) attributed heavy rainfall in London area in August 1975 to the quasi-stationary cumulonimbus system and local orography.

### **2.2.2 Upper-Level Positive PV Anomaly**

A number of studies have associated the severe precipitation events, commonly in the mid-latitudes, with tropopause fold and upper troposphere potential vorticity (PV) anomaly. Massacand et al. (1998) and Fierli et al. (2003) have shown a linkage between upper-level PV anomaly associated with deep tropopause fold over the mountain ridge and the heavy rainfall events in the European Alps and in Algeria respectively. When a positive PV anomaly associated to deep tropopause fold occurs over mountains, it

couples with the elevated topography and produces strong Sawyer-Eliassen circulation around the jet over the mountain slope.

A positive PV anomaly associated with a deep tropopause fold over high mountains seems to be able to couple with the elevated topography and establish the favorable coherent environment for surface low deepening (Arreola, et al. 2003). Massacand et al. (1998) suggested that the north-south oriented upper-level positive PV anomaly streamer, during heavy precipitation over the European Alps, produced favorable conditions by reducing static stability beneath the anomaly, setting up rising motion in the forward flank (southward) of the anomaly, and enhancing a moist southerly flow component towards the mountains (Figure 2.6; Figure 2.7). The elevated topography may play a critical role in producing a “wall effect” which leads to the surface convergence region associated with moist low-level air flow over the mountain slope (Homar, et al. 2002) and same wall as can be seen in Figure 2.7.

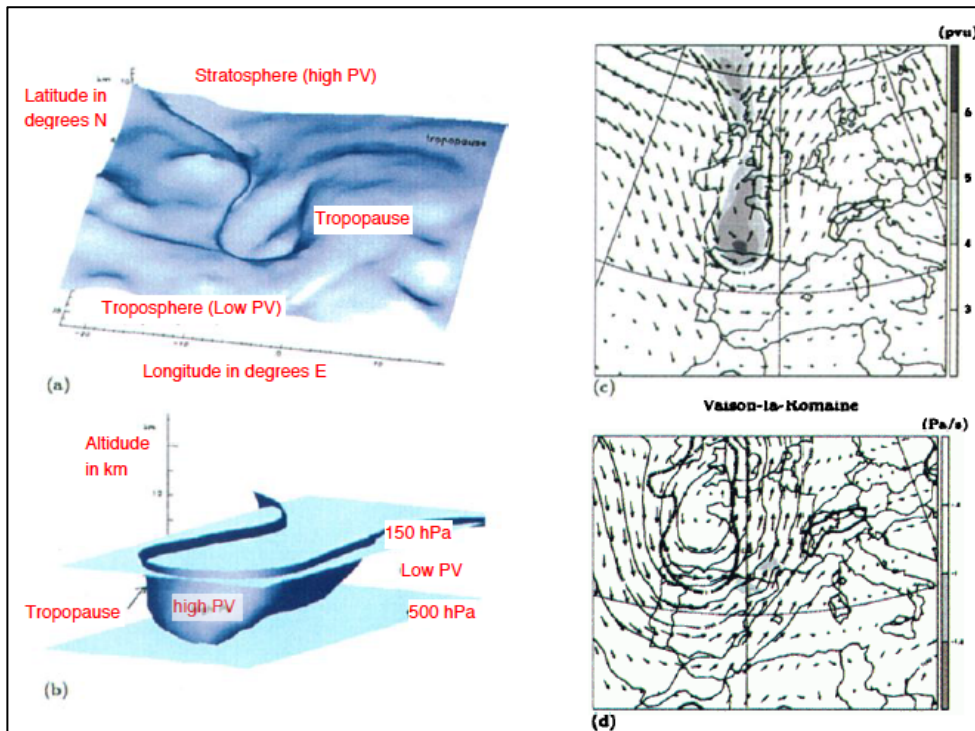


Figure 2.6: “Vaison-la-Romaine”, France heavy rainfall event synoptic situation at 00UTC 22Sep 1992. (a) Tropopause (2-PVU isosurface) from above; (b) from below; (c) Distribution of 500-150 hPa layer mean potential vorticity (shaded in PVU) and wind in vectors at 200 hPa; (d) 3-PVU isoline of 500-150 hPa layer mean potential vorticity (thick dash-dot pattern) superimposed upon 700 hPa wind (vectors), geopotential heights (thin solid line, 30m spacing) and ascent (shaded, in Pa/s). Alpine region outlined as a thick solid line. All the panels are from Massacand et al. (1998) with improved labeling.

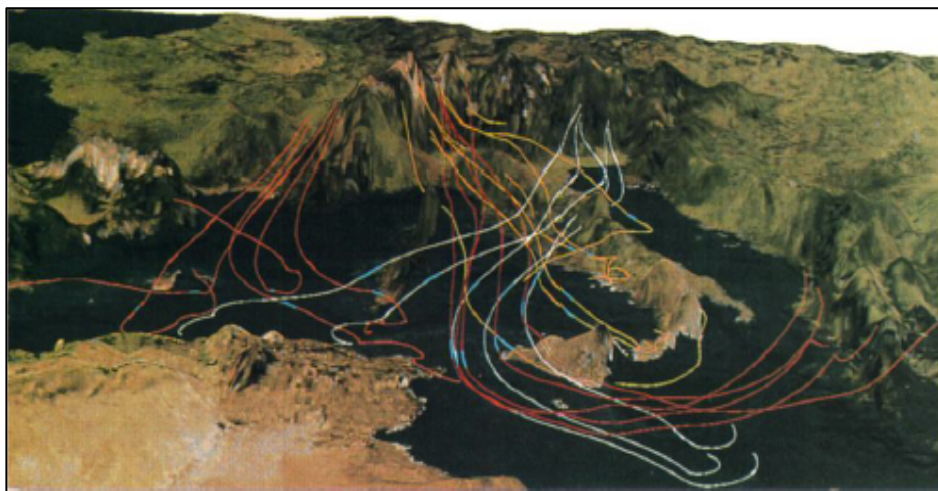


Figure 2.7: 72-hour backward trajectories viewed from the south in 3 dimensions. Integration starts south of the Alps (mid-picture range) at  $t=0$  i.e. 12UTC Sep 22, 1992 for Vaison-la-Romaine (pink tracks), 00UTC Sep 24, 1993 for Brig (red), 00UTC Nov 06, 1994 for Piedmont (yellow), and 18UTC Sep 13 1995 for South Ticino (white).  $T \sim -18$  hours is marked in blue. Figure from Massacand et al. (1998).

Moreover, recent studies have shown important role of the upper-level PV anomaly on extreme events in the South Asian subtropics. Hong et al. (2011) and Martius et al. (2012) attributed the forced orographic lifting of moist layer from the Arabian Sea to the upper-level positive PV anomaly during the July 2010 Pakistan flooding. Above studies highlighted role of upper-level positive PV anomaly as an agent that intensifies/triggers the surface low pressure forcing not only in the mid-latitudes but also in the South Asian monsoon region.

### **2.3 Tropical-Extratropical Interaction Aspects of Extreme Rainfall Events**

A number of studies showed that tropical-extratropical interactions can lead to the extreme convective weather systems in the tropics and extratropics (e.g., Sardeshmukh and Hoskins 1988; Kiladis and Weickmann 1992a; Kiladis and Weickmann 1992b; Ding and Wang 2007; Knippertz 2007, Hong et al. 2011). Extreme rainfall events, named as Predecessor Rainfall Events (PREs), in the United States are one of the examples of tropical-extratropical interaction. These rain events occur due to the interaction of upper-level westerly jet and low level moisture source from the tropical cyclones in the south (Galarneau et al. 2010; Bosart et al. 2012; Moore et al. 2012). Rappin et al. (2011) showed that presence of upper-level westerly jet north of the tropical cyclone leads to more rapid intensification and maximum potential intensity. Similarly, Chang et al. (1998) discussed Heavy rainfall events in the Mei-yu fronts in May and June over eastern China was due to the tropical-extratropical interaction. Riehl (1977) showed that interaction between deep mid-latitude upper trough with the pre-existing tropical disturbance can lead to the heavy precipitation in Venezuela.

While above studies provide evidence of tropical-extratropical interaction from diagnostic perspectives, the analysis of heat and momentum exchange between tropics and extratropics provides physical perspectives in this interaction. For example, Riehl (1977) discussed transport of heat, mass and momentum from tropics to extratropics during deep trough intrusion to the tropics. Few authors used trajectory analysis and the strength of the local Hadley circulations to show the tropical-extratropical interactions (e.g. Knippertz 2007).

This section is divided into two sub-sections. First, it presents a review of theories that highlights force imbalances in the upper-level that leads to the stronger tropical-extratropical interaction. Most previous studies on the tropical-extratropical interaction pointed out the role of deep extratropical trough triggering convection in the tropics (e. g. Riehl 1977; Kiladis and Weickmann, 1992a; Ding and Wang, 2007; Knippertz, 2007, Hong et al., 2011). These studies used quasi-geostrophic theory to explain the upper-level deep trough coupling with the tropical surface system in lower troposphere. While deep troughs of the Rossby wave train play important role in intensifying low-level forcing, a number studies have highlighted the importance of upper-level anticyclone and anticyclonic shear of jet streak on extreme events (Mecikalski and Tripoli 2003; Galarneau et al. 2010; Rappin et al. 2011; Bosart et al. 2012; Moore et al. 2013). The authors' explanation of importance of upper-level anticyclone and anticyclonic shear (horizontal wind shear that contributes the anticyclonic vorticity, mainly on the equatorward side of the westerly jet where wind speed increases poleward) might provide important insight on the weak inertial stability and the enhanced tropical-extratropical interaction associated with extreme events. Weak inertial stability indicates weakening of balance between pressure and inertial forces. The first section highlights the principle of

force balance dynamics in the outflow level of the convective systems in the presence of upper-level ridge/jet streak and how this dynamics is related to the enhancement of tropical-extratropical interaction.

Tropical heating has not only been established as the forcing that generates Rossby waves in the equator (Matsuno 1966; Gill 1980; Lau and Lim 1982) but also been considered as the influencing factor in the mid-latitude wave train dynamics (Hoskins and Jin 1991; Jin and Hoskins 1995; Kiladis and Weickmann 1992b). The second part reviews the theories that explain the mechanism that triggers the tropical-extratropical interaction during extreme events. In other words, it discusses the mechanism that explains how the tropical heating triggers mid-latitude waves and might generate force imbalances in the upper-levels.

### **2.3.1 Upper-Level Upper Force Imbalance Theory in Tropical-Extratropical Interaction**

The constraint on upper-level tropical-extratropical interaction is the apparent inertial force that acts against the poleward directed pressure gradient force that suppresses meridional acceleration (Held and Hou 1980; Schneider 1977). The authors defined this constraint as an angular momentum conserving circulation, which in turn leads to the inertial stability. Locally, the level of this constraint is often quantified as the inertial stability that depends not only on the Coriolis parameter, but on the vortical and deformational structure of the flow. Any mechanism that erodes this stability can make the formation of a meridionally directed force imbalance more probable and so enhance the likelihood of tropical-extratropical interaction. This section highlights the upper-level

force imbalance as a mechanism that relates the extreme weather and tropical-extratropical interaction.

A number of studies showed important role of upper-level inertial instability in the intensification of storms in the tropics and extratropics (Melowsky and Tripoli 2003; Galarneau et al. 2010; Rappin et al. 2011; Bosart et al. 2012; Moore et al. 2013). Galarneau et al. (2010), Bosart et al. (2012) and Moore et al. (2013) studied the role of upper-level jet in the production of weak inertial stability or even inertial instability in causing extreme rainfall events named as Predecessor Rainfall Events (PREs) in the United states. PESs are heavy rainfall events occurring ahead of tropical cyclones. PRE's occur in association with poleward advection of a deep moist layer established by the tropical cyclones in the Gulf of Mexico/Atlantic Ocean off the coast of Florida, and in the presence of a surface lifting mechanism, such as fronts, convergence or orographic regions. Moore et al. (2013) have described three types of PREs that can achieve weak inertial stability or inertial instability in the upper-level depending on the position of the jet relative to the ridge (Figure 2.8 a-c). The SJ type PREs occur near an equatorward jet entrance region (Moore et al. 2013). Although these studies only provide diagnostic approach to relate inertial stability with extreme events, it can be implied that the combination of jet and ridge created the imbalance in the normal geostrophic/gradient wind balance between pressure gradient and inertial forces.

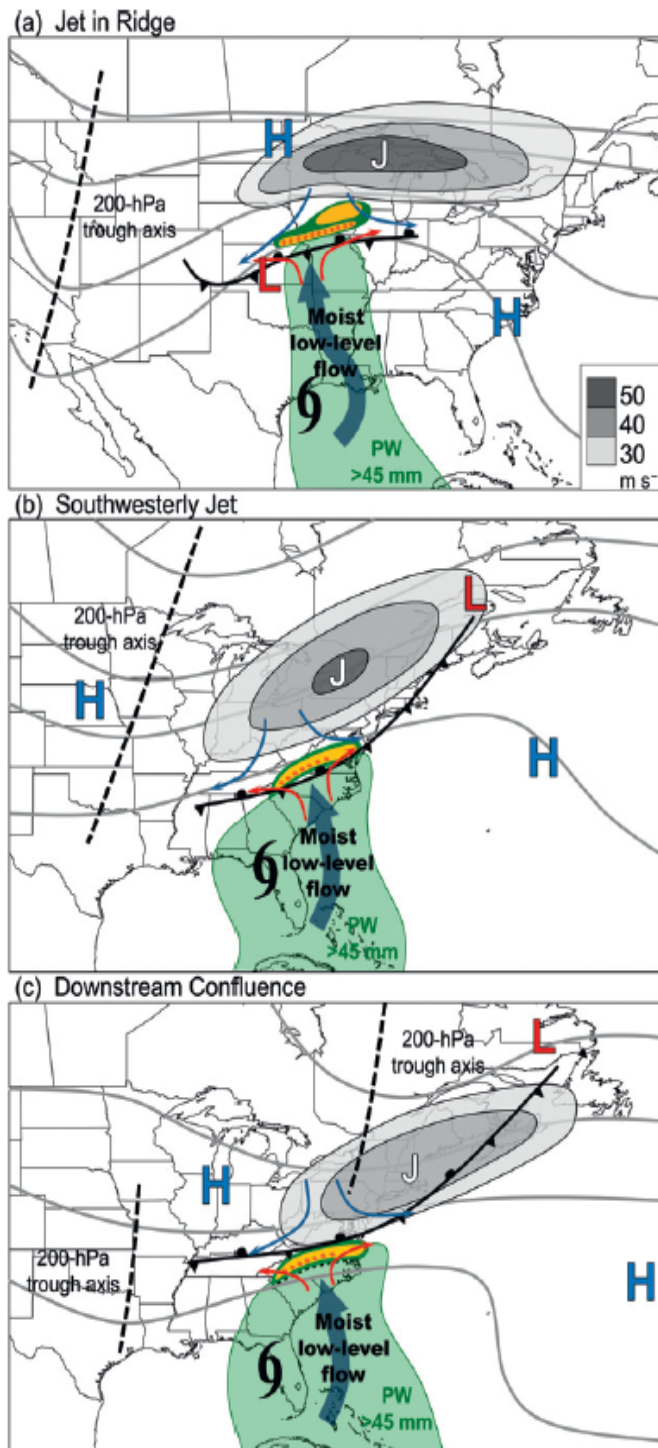


Figure 2.8: Conceptual model of the key synoptic-scale features and processes for three categories PREs (a) Jet in ridge (JR); (b) Southwesterly jet (SJ); (c) Downstream confluence (DC). The gray contours denote the 200-hPa geopotential height, with the thick dashed black line marking the primary trough axis. The gray shaded regions represent 200-hPa wind speed [m/s; gray shade bar in (a)] and the “J” marks the 200-hPa wind speed maximum. The thin red and blue arrows represent 925-hPa streamlines associated with regions of warm and cold advection, respectively. The position of the surface front is shown in standard frontal notation, and the positions of the sea level pressure maxima and minima are marked by the “H” and the “L” symbols, respectively. The light green shading indicates the region with PW values >45 mm. The thick blue arrow represents a corridor of moist low-level flow. The dark green, gold, and orange shaded regions represent radar reflectivity thresholds of 20, 35, and 50 dBZ, respectively, associated with the PRE. The TC location is indicated by the tropical storm symbol. All panels are from Moore et al. (2013).

Rappin et al. (2011) showed the impacts of the upper-level weak inertial instability on the tropical cyclone intensification and peak strength. Their main argument was that weak

inertial stability in the outflow layer of the tropical cyclone minimizes an energy sink of its secondary circulation and leads to more rapid intensification and maximum potential intensity. They proved their argument by adding an upper-level jet streak north of the cyclone vortex. They argued that the anticyclonic shear side of the jet stream weakens the inertial stability and as tropical cyclone outflow expands to the equatorward side of the jet stream, the energy expenditure of forced subsidence is minimized. The minimization is by ventilating all outflow in one long narrow path which allows more radiational cooling and lessens the work of subsidence leaving more energy for intensification. However, the authors did not use any objective parameter to define strength of inertial stability/instability, other than qualitatively mentioning anticyclonic side of jet as a qualitative measure.

Mecikalski and Tripoli (2003) showed that the mesoscale convective systems organizes itself to access the region of lowest upper-level inertial stability. The authors used low (negative) upper-level PV to objectively define the weak inertial stability (inertial instability) in northern hemisphere. Similarly, Blanchard et al (1998) discussed the role of weak inertial stability in the strengthening of mesoscale convective systems. In contrast to the convective systems that often develop in an environment with strong embedded short waves and cyclonic vorticity, many MCCs and MCSs have been observed to form in the environments where the value of isentropic absolute vorticity may approach zero or are negative, resulting in regions with weak inertial stability or inertial instability. Figure 2.9 shows the conceptual diagram of regions of weak inertial instability. Blanchard et al (1998) used the ratio,  $\alpha$ , of geostrophic absolute vorticity in isentropic level to the Coriolis parameter to objectively define the inertial instability parameter. They defined inertial instability when  $\alpha$  is negative and weak inertial stability when  $\alpha$  is close

to zero. Of the MCCs/MCSs of their study, 24% of the events showed inertial instability and most of them showed weak inertial instability prior to the storm. This shows parameter alpha seems to be a reasonable objective measure of inertial instability/weak inertial stability. However, this alpha parameter depends on geostrophic absolute vorticity, which might be problematic in the low latitudes. Moreover, Petterssen (1953) argued that application of absolute geostrophic vorticity over estimates the actual absolute vorticity and thus produces error in the prediction of storms using vorticity advection.

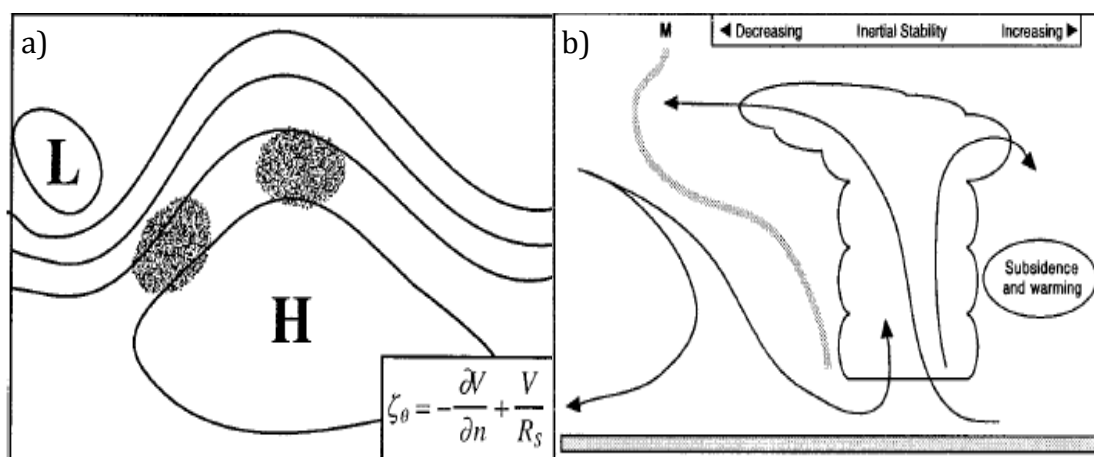


Figure 2.9: Regions of upper-level weak inertial stability or inertial instability and its role in MCS organization. (a) Two typical regions for the occurrence of mesoscale convective systems (MCSs; darkened regions). Contours are representative of the Montgomery streamfunction (height) on isentropic (pressure) surfaces. Lows and highs marked by L and H, respectively. The equation for isentropic relative vorticity  $\zeta_{\theta}$  is given in natural coordinates. The first term on the right-hand side is the shear term and the second is the curvature term, where  $V$  is the wind speed,  $n$  is a distance oriented normal to the streamline, and  $R_s$  is the radius of curvature of the streamlines. (b) Cross section in the  $y$ - $z$  plane showing the conceptual model of trajectories of air parcels in inertially stable and unstable regions. In the inertially stable region (right side), outflow material descends in the near environment, resulting in drying and warming. The region of inertial instability (left side) permits meridional accelerations of outflow material. The thick, shaded line is a momentum (M) surface typical of inertially unstable regions. The vertical shear vector is directed into the page. Both panels are from Blanchard et al (1998).

Alaka (1961) argued that inertial instability could be developed even with positive upper-level absolute vorticity. She derived a frequency (inertial instability parameter) (Eq. 1) from the gradient flow equation.

$$\gamma^2 = \left[ \left( \frac{2V}{R} + f \right) \eta \right]_{\theta} \dots \dots \dots (1)$$

Where  $\gamma$  is the inertial frequency,  $V$  is magnitude of horizontal wind,  $R$  is the radius of curvature of trajectory of the flow,  $\eta = \zeta + f$  is absolute vorticity,  $\zeta$  is the relative vorticity and  $f$  is the coriolis parameter and all the variables are in isentropic level  $\theta$ . First term in the right hand side is curvature term and second term is absolute vorticity, which contains shearing term. When the right hand side term of Eq. (1) is negative,  $\gamma$  becomes imaginary and the motion is unstable and the author defined this as an inertial (dynamic) instability. The author argues that  $\gamma^2$  can be negative either when  $\eta < 0$  with normal winds or when curvature term is negative with positive absolute vorticity in the northern hemisphere. This expression seems more robust than just using absolute geostrophic vorticity. However, this expression ignores non-linear terms of the momentum equation.

Petterssen (1953) derived the force balance equation using primitive horizontal momentum equation in the isentropic coordinate. He did not ignore any non-linear terms from the primitive equation. His work was motivated from the fact that the absolute vorticity computed from the geostrophic approximation ignore non-linear terms of the full momentum equations and thus give error in the estimation of pressure field from this vorticity. He showed that the balance between the Laplacian of the pressure and the vorticity is significantly influenced by other non-linear terms of the momentum equation.

He derived an expression that shows balance between pressure field and vorticity terms that includes divergence, deformation and beta effect as below:

$$P = (Q^2 - A^2 - B^2 - D^2 - 2\beta * u) \times 0.5 \text{-----}(2)$$

Where,

$$\text{Pressure Field, } P = \nabla^2 M + f^2$$

M is the Montgomery streamfunction and  $f$  is coriolis parameter

$$\text{Absolute Vorticity, } Q = \zeta + f$$

$$\text{Relative Vorticity, } \zeta = \frac{\partial v}{\partial x} - \frac{\partial u}{\partial y}$$

$$\text{Stretching Deformation, } A = \frac{\partial u}{\partial x} - \frac{\partial v}{\partial y}$$

$$\text{Shearing Deformation, } B = \frac{\partial v}{\partial x} + \frac{\partial u}{\partial y}$$

$$\text{Divergence, } D = \frac{\partial u}{\partial x} + \frac{\partial v}{\partial y}$$

$u$  and  $v$  are zonal and meridional components of the actual wind respectively.

P is the pressure field that incorporates Laplacian of pressure (Montgomery streamfunction in theta surface) that is corrected for the pressure generated by the centrifugal acceleration due to the rotation. He used this expression to compute actual absolute vorticity Q and argued that the geostrophic approximation overestimates the actual absolute vorticity and showed that the difference is entirely due to the deformation term. He argued that in the geostrophic approximation, the instantaneous wind was assumed to be well adjusted to the pressure contour, though no acceleration mechanism is provided to allow the wind to remain adjusted when the air moves through a variable contour field. The expression in Eq. (2) provides an insight on the complex relation between the configuration of the pressure contour field and the vorticity and other non-linear terms. This expression also confirms that deformation and divergence can change

the balance between pressure field and vorticity.

In Eq (2), when right hand side is positive this expression represents an acceleration mechanism that will enable the wind to remain adjusted while the air moves through a variable pressure field in the process to seek for balanced adjustments. But when right hand side is negative the square root of  $P$  becomes imaginary and suggests that pressure field is not balanced by the sum of the other forces in the equation of motion. Therefore the expression in the right hand side can be used to define the term that induce imbalance between pressure and inertial terms. Negative values on the right hand side is representative of terms that weaken the equatorward restoring force that works against poleward pressure gradient forced. The negative value of right hand side term, therefore, will allow the flow to move in the direction of pressure gradient force until it reaches the region where it is balanced as represented by the positive values of this term. Since this expression provides a robust measure of force imbalance in the upper-level, it can be used here to see its role in the enhancement of tropical extratropical interaction during extreme events. This approach has not been used previously to understand the tropical-extratropical exchange and its role in extreme rain events.

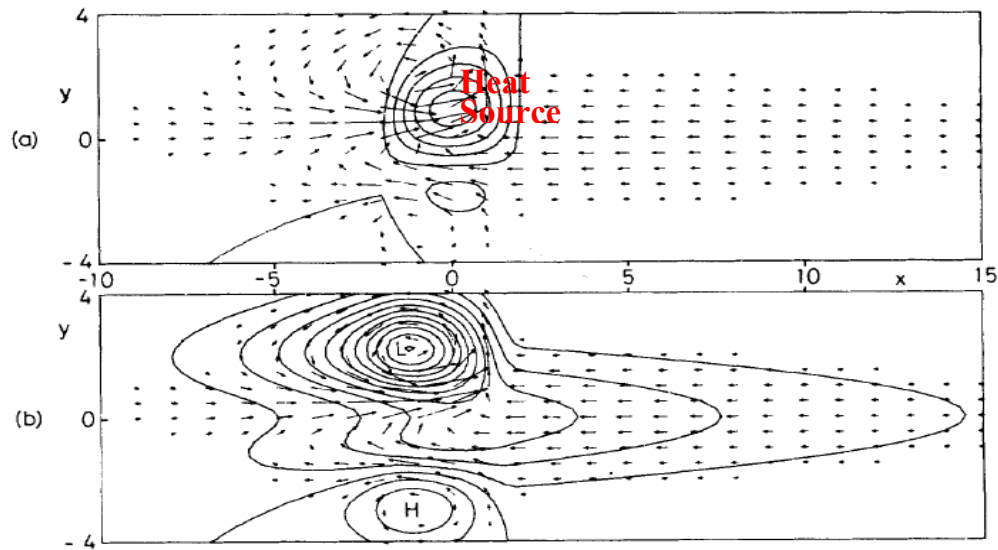


Figure 10: The dynamical response of the Gill model (Gill 1980) to asymmetric heating source (north of equator). (a) The surface wind field (vectors) and vertical motion field (contours, 0.3 interval: upward in north of equator); (b) The surface wind field and perturbation pressure (contours 0.3 interval). Both panels from are Gill (1980).

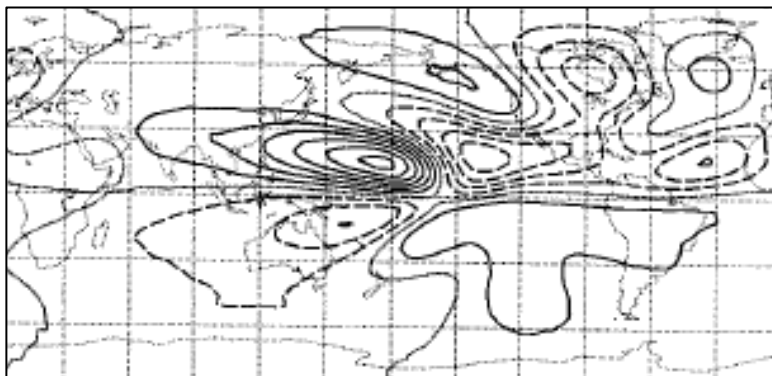


Figure 2.11: Day 15 perturbation streamfunction fields (zonal average removed) for equatorial heating on Dec-Feb zonal flow for upper-level. The contour interval is  $10 \times 10^5 \text{ m}^2/\text{s}$ . The zero contour is dotted and negative contours are dashed. Figure from Jin and Hoskins (1995).

### **2.3.2. Eddy Shedding: A Mechanism Linking Tropical Heating, Rossby Wave, Upper-Level Force Balance and Tropical-Extratropical Interaction**

Previous studies have shown tropical-extratropical interaction from two perspectives on the origination of the forcing mechanisms. One group of research showed the extratropical waves as a source of forcing for the tropical weather events. These studies considered extratropical-tropical interaction resulting from the intrusion of eastward moving upper-level troughs originating in the extratropics that then trigger convection in the tropics (e.g. Kiladis and Weickmann 1992a; Knippertz 2007; Ding and Wang 2009; Hong et al. 2011). The other studies have discussed the influences of tropical heating as a forcing on the mid-latitude weather (Sardeshmukh and Hoskins 1988; Kiladis and Weickmann 1992b). They showed that tropical convection generates a Rossby wave train poleward of the convective heating source. Gill (1980) not only showed that the tropical heating could produce equatorial Rossby waves in the west and Kelvin waves east of the heating center as a dynamic response, but also suggested that it can influence the extratropics whenever the heating is off the equator in the resting atmosphere. Figure (2.10a) shows the Gill (1980) dynamic response at the lower troposphere due to the tropical heating north of the equator for resting atmosphere. The figure shows a surface low northwest of tropical heating in the northern Hemisphere. The author found upper-level anticyclonic flow aloft the surface low.

The Gill (1980) model was for the resting atmosphere and does not provide insight on how the response would be in the presence of the basic zonal flows. Jin and Hoskins (1995) used the Gill model for the northern winter basic flow (with Dec-Feb zonal flow). They found two types of response. The response near the equator remained same as that with the Gill resting atmosphere response but the response also showed a tendency to

produce downstream (eastward) development of a Rossby wave train when the response interacted with the mid-latitude westerlies (Figure 2.11). This study was based on the equatorial heating and was done for the northern hemisphere winter (Dec-Feb) basic flow and does not provide information on how off-equator heating will impact upstream (westward) of heating source in the presence of upper-level easterlies.

A number of studies have discussed the westward eddy shedding process of the upper-level anticyclone due to anomalous tropical convection (Hsu and Plumb 2000; Popovic and Plumb 2001; Garny and Randel 2013). The authors discussed the eddy shedding process as a result of anticyclone breaking into transient eddies due to the instability from tropical heating. They defined this instability as a dynamic instability. Hsu and Plumb (2000) explained eddy-shedding process based on circulation theorem and role of divergence. They started with circulation tendency in the outflow layer for the time mean around the closed contour C, (Eq. 3):

$$\oint_C \frac{\partial \bar{u}}{\partial t} \cdot dl + \iint_A \nabla \cdot (\bar{\zeta}_a \bar{\mathbf{u}}) dA = \iint_A \nabla \cdot (\overline{\zeta'_a \mathbf{u}'}) dA + \oint_C \bar{F} \cdot dl \quad \text{-----}(3)$$

where A is the area enclosed by that contour C,  $\bar{\zeta}_a$  is mean absolute vorticity,  $\bar{\mathbf{u}}$  is mean wind, and the terms on the right describe the contributions of transient eddies and friction, respectively. For inviscid steady state condition in the absence of eddies and mean absolute vorticity  $\bar{\zeta}_a$  Eq. (3) becomes:

$$\bar{\zeta}_a \iint_A \nabla \cdot \bar{\mathbf{u}} dA = 0 \quad \text{-----}(4)$$

Eq. 4 represents the constraint that in the region with non-zero mean absolute vorticity, divergence has to be zero. For a divergence to occur in an inviscid flow the absolute vorticity must be zero. However, Hsu and Plum (2000) showed that even in the presence of divergence in an inviscid anticyclone with nonzero mean absolute vorticity satisfy the circulation constraint Eq (4) through the eddy shedding process. The main role of eddy shedding process is to relax the constraint Eq (4) by transporting PV through transient eddies, shed from the forced anticyclone and hence minimizes the effect of divergence.

Moreover, the authors showed that the eddy shedding pattern depends on the latitudinal location of forcing due to heating. They conducted a number of experiments with 2D shallow-water model for non-axisymmetric model for  $\beta$ -plane, for a varying strength of divergence, background uniform flow,  $\beta$  effect and coriolis parameter. The eddy shedding process initiates as the conditions becomes super critical causing the system to be unsteady. They found that the condition becomes supercritical in two ways: First when flow parameter is supercritical and second when the  $\beta$  parameter becomes supercritical. When the strength of the external uniform flow is high enough compared to the divergent flow, i.e when the ratio of the two flows is higher than 1.65, the flow parameter becomes supercritical. Secondly, when the strength of the “ $\beta$ -drift” is high enough compare to the divergent flow such that the ratio of two becomes greater than 2.16, the  $\beta$  parameter becomes supercritical and that leads to the unsteady condition. They performed two sets of experiments using these two parameters. For the flow parameter experiment with f-plane and the supercritical condition, eddies shed eastward (Figure 2.12 a-d). When the eastward tongue is long enough in the zonal direction, the vorticity strip becomes unstable and rolls up into a small vortex that is shed downstream. They concluded that for a steady non-axisymmetric circulation to exist under an external uniform flow, the

magnitude of the external flow cannot be much larger than that of the forced divergent flow. If the flow parameter becomes much larger than supercritical value, the potential vorticity (PV) distribution becomes zonally oriented, and the induced return flow is not strong enough to prevent the anticyclonic vorticity from being advected downstream by the external flow. In  $\beta$  parameter experiment for the mid-latitude and supercritical conditions, the eddy shedding process took place in the westward direction (Figure 2.13 a-d). Since the focus of this dissertation is on the impact of the heating force on South Asian High, the analysis will focus only on the westward eddy shedding process. In these cases, the vortex pattern shifted further southwestward and the area of convergence expanded. Along with a thin anticyclonic strip drawn out of the forcing area, a cyclonic strip was advected around the eastern flank of the anticyclone. Both strips became unstable and rolled up into a pair of vortices which then shed westward and disappear gradually.

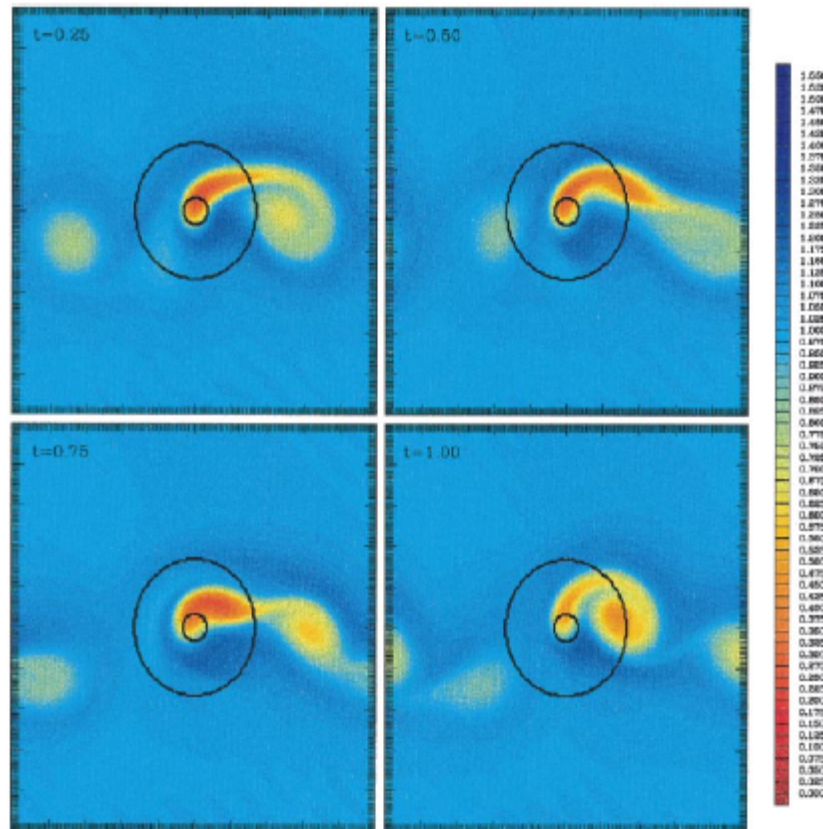


Figure 2.12: Eddy shedding experiment for f-plane for supercritical flow condition. The phases of shedding cycle ( $t=1$ ) at  $t=0.25$ ,  $t=0.5$ ,  $t=0.75$ ,  $t=1.0$ . Shading is absolute vorticity with an interval of  $0.025f_0$  between 0 and 1.575 (warm color: low vorticity and cold colors high vorticity). The inner circle marks the size of the imposed axisymmetric mass source (corresponding to heat source) and the outer circle marks the limit of the corresponding axisymmetric divergent circulation. From Hsu and Plumb (2000).

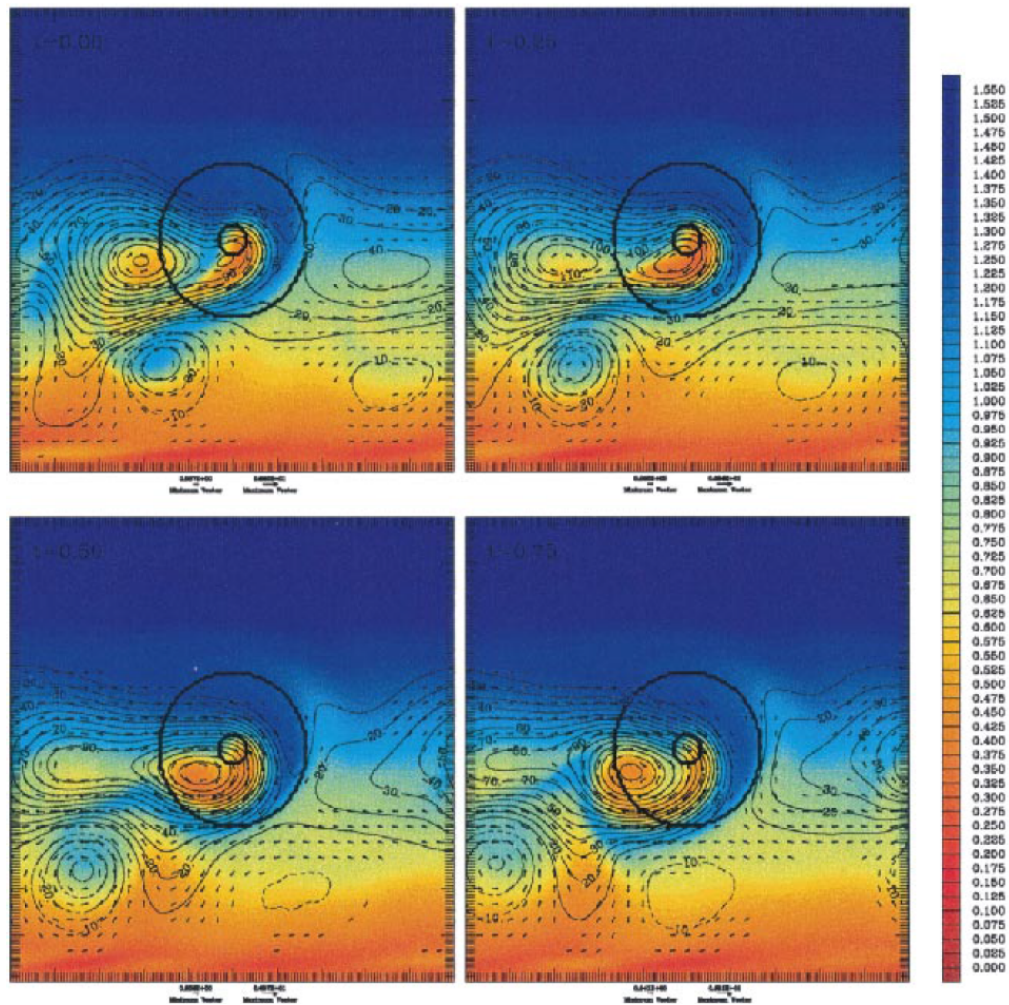


Figure 2.13 Eddy shedding experiment for  $\beta$ -plane for supercritical  $\beta$  parameter. The phases of shedding cycle ( $t=1$ ) at  $t=0.25$ ,  $t=0.5$ ,  $t=0.75$ ,  $t=1.0$ . Shading is absolute vorticity with an interval of  $0.025f_0$  between 0 and 1.575 (warm color: low vorticity and cold colors high vorticity). The line contours are geopotential perturbation plotted with a contour of  $10\text{m}^2\text{s}^{-2}$ . Vectors denote the wind field. The inner circle marks the size of the imposed axisymmetric mass source (corresponding to heat source) and the outer circle marks the limit of the corresponding axisymmetric divergent circulation. From Hsu and Plumb (2000).

For the  $\beta$  parameter scenario, the authors showed that the westward eddy shedding pattern changes with the latitudinal position of the heating forcing (Figure 2.14a-c). This figure (top to bottom) represents results for heating centered at mid-latitudes, subtropics and near equator respectively. The figure shows that for lower limit of supercritical  $\beta$  parameter, the pattern becomes less wavy as the forcing shifts to equatorward. The authors explained that this elongation of anticyclone with decreasing latitude is the result

of dynamic interaction of flow dynamics with the  $\beta$  effect as the heating function moves equatorward. One of the interesting outcomes of their  $\beta$  experiments is the one with the  $\beta$  parameter of 17.28, much higher than the lower limits of supercritical values (4.32) and the heating forcing located between subtropics and near-equator (Figure 2.15). In this scenario, the authors noticed frequent development of transient eddies. Figure 2.15 represents a snapshot of the westward eddy shedding in this scenario and the authors highlighted that it resembles the snapshot of Tibetan anticyclone during monsoon season with easterlies in the south and westerlies in north of the forced anticyclones from the monsoonal heating. Nevertheless, they concluded that the eddy shedding process is merely upper-level phenomena and did not seem to impact surface. The authors did not look into the case describing how it will couple with mid-latitudes and how these changes in the mid-latitudes, in turn, impact the lower troposphere. Few studies showed the relation between outflow from the monsoon anticyclone and Rossby wave breaks downstream (Postel and Hitchman 1999, 2001). The authors attributed the Rossby wave breaking to the dynamical instability created by reversal of PV gradient and thus lead to tropical-extratropical mixing.

The eddy shedding studies suggest that depending on the latitudinal location of monsoonal heating, the pattern of the eddy shedding changes. They further imply that if the monsoonal heating shifts northward from its normal location and the eddies expand meridionally and becomes wavy, the heating is most likely near equator creating zonally elongated westward shedding. Therefore it appears that the shift of monsoonal heating northward might trigger a favorable condition for enhanced tropical-extratropical interaction as suggested by Postel and Hitchman (1999, 2001), which might have led to the extreme cloudburst events in the Nepal Himalayas.

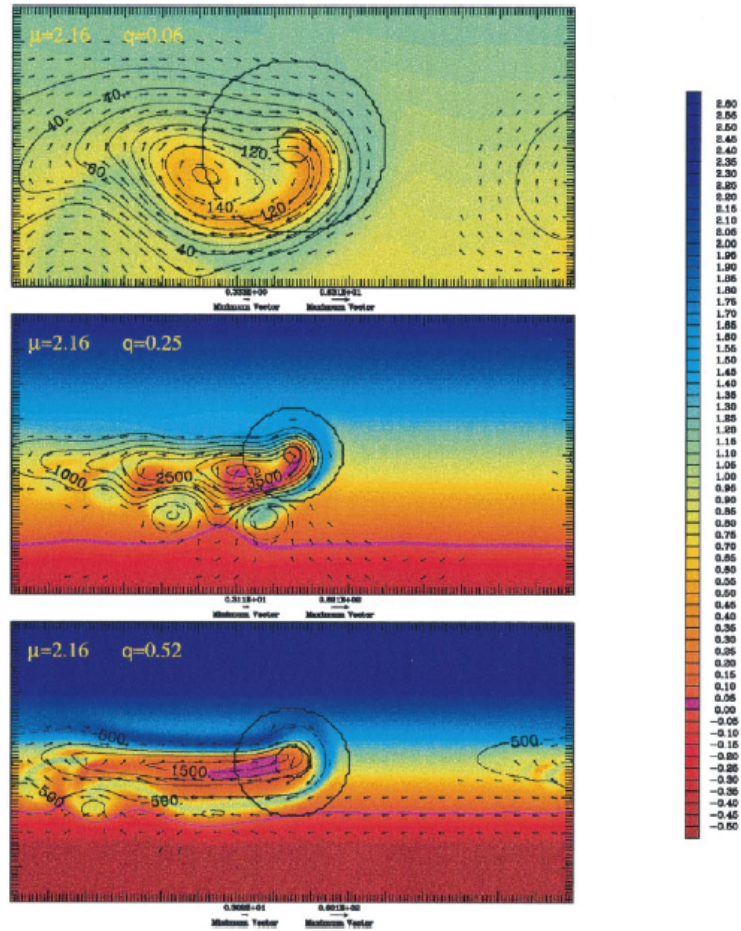


Figure 2.14: A snapshot of model output on Eddy shedding experiment for  $\beta$ -plane with critical  $\beta$  parameter but with heating function at various latitudes (various values of  $q$  parameter). Top: equivalent to mid-latitudes; Middle: equivalent to subtropics; Bottom: equivalent to near equator. Shading is absolute vorticity with an interval of  $0.025f_0$  between 0 and 1.575 (warm color: low vorticity and cold colors high vorticity). The line contours are geopotential perturbation plotted with a contour of  $10\text{m}^2\text{s}^{-2}$ . Vectors denote the wind field. The inner circle marks the size of the imposed axisymmetric mass source (corresponding to heat source) and the outer circle marks the limit of the corresponding axisymmetric divergent circulation. From Hsu and Plumb (2000).

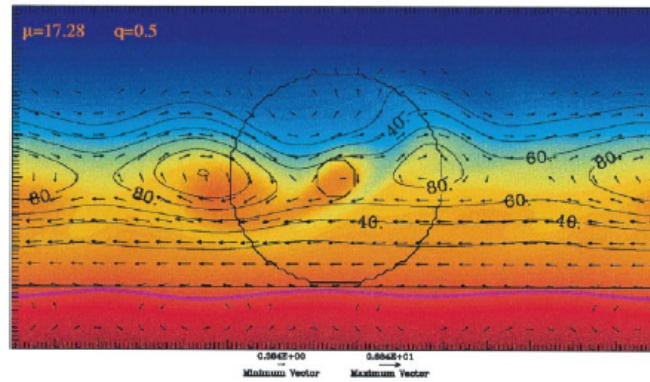
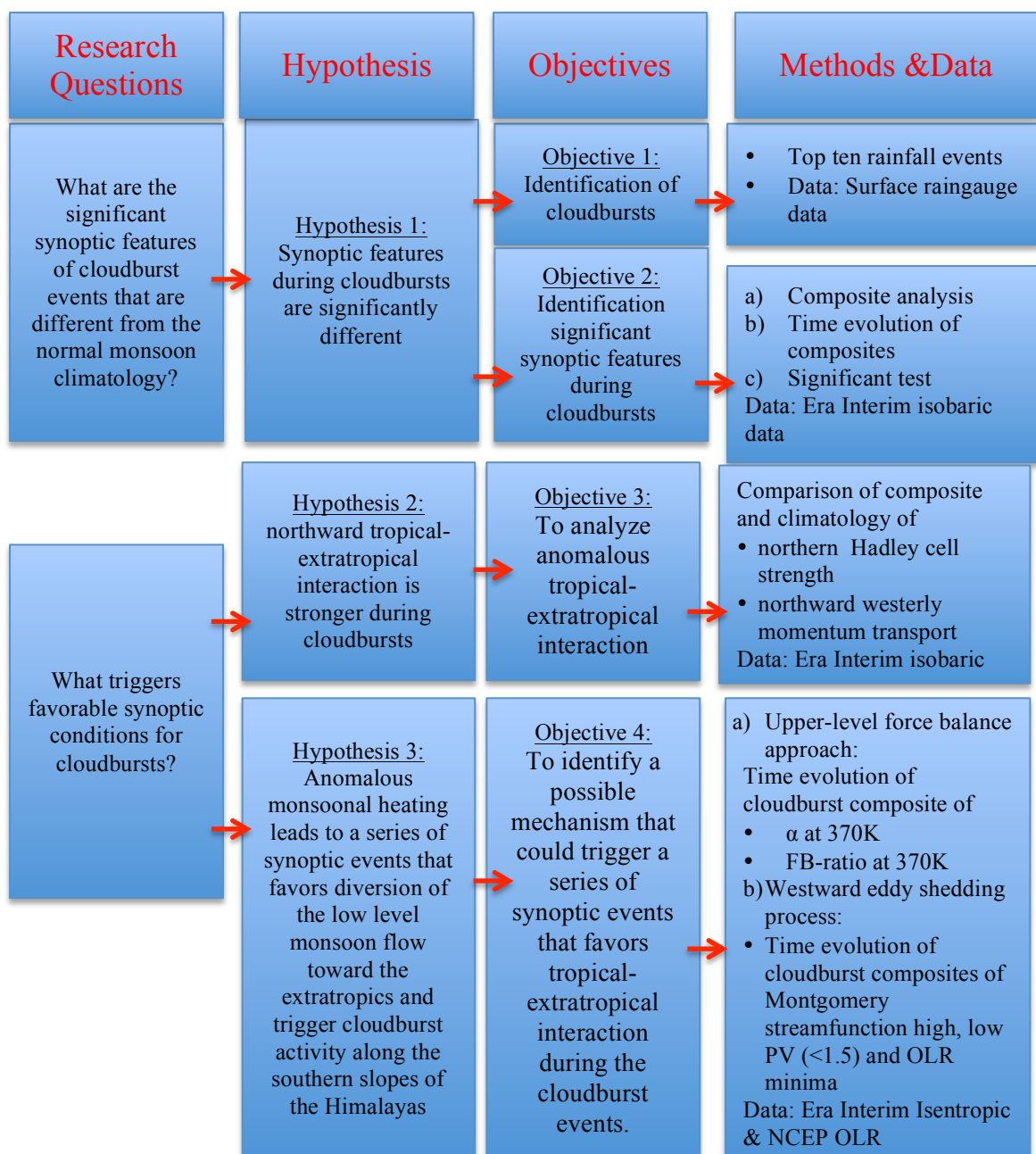


Figure 2.15: Snapshot of model output on eddy shedding experiment for  $\beta$ -plane with high supercritical  $\beta$  parameter and heating function at between subtropics and near equator ( $q=0.5$ ). Shading is absolute vorticity with an interval of  $0.025f_0$  between 0 and 1.575 (warm color: low vorticity and cold colors high vorticity, color scheme is same as in Figure 2.14). The line contours are geopotential perturbation plotted with a contour of  $10\text{m}^2\text{s}^{-2}$ . Vectors denote the wind field. The inner circle marks the size of the imposed axisymmetric mass source (corresponding to heat source) and the outer circle marks the limit of the corresponding axisymmetric divergent circulation. From Hsu and Plumb (2000).

## Chapter 3

### Methodology and Data

This chapter presents methods used in accomplishing objectives to seek support for the hypotheses of this research. It also provides the framework of the research designed to achieve these goals. This chapter furthermore describes the data used and discusses the limitation of methods and data used. The framework of this dissertation research is presented in chart below and detail methods are explained in the subsequent sections:



### 3.1 Objective 1: Identifying Cloudbursts Events:

The term “cloudburst” is used by atmospheric scientists in the Indian Subcontinent to refer to localized rainstorms characterized by a few hours of very intense rainfall in the Himalayas during the monsoon season, commonly in July and August (Das et al. 2006). Because of the sparse station network for rainfall intensity and other meteorological variables (e.g. upper air), not enough *in situ* data are available on the cloudburst events in the Himalayas for an optimal scientific investigation of the occurrence and precise location of these storms. Lack of sufficient meteorological information was likely the main limiting factor in preventing the development an objective definition of the cloudbursts in the past. For example, Das et al. (2006) presented only an unofficial definition of “cloudburst” to be “a storm with a rainfall intensity of 75-100 mm/h in India” but did not indicate any evidence of such intensity during the cloudbursts in India. The only “cloudburst” event with recorded rainfall intensity in the Nepal Himalayas was the event of July 19-20, 1993, which occurred in the Kulekhani watershed. The maximum hourly rainfall intensity recorded during this event was 65 mm/h (ISET-N and ISET 2009). Based on the daily rainfall data, this event produced the highest daily rainfall (540 mm) ever recorded in Nepal’s data history. Unavailability of sufficient *in situ* rainfall intensity data for cloudburst events limits our ability to analyze and identify cloudbursts based on rainfall intensity criteria.

Our research found remotely sensed rainfall intensity data available for this region (Yamamoto et al. 2011). According to Yamamoto et al. (2011) 3-hourly tropical rainfall measuring mission (TRMM) (3B42 version 6) rainfall data are one of the best available remotely sensed rainfall intensity data sets for this region. However, this assertion was

based on the comparison of the mean monsoon rainfall from the satellite products with mean rainfall from individual rain-gauge station data. Unfortunately, they compared datasets in which durations of the data were not the same. They also did not look at day-to-day or shorter timescale variability in intensity, which is critical to our analysis. Barros et al. (2000) compared instantaneous rainfall intensity estimated from the TRMM Precipitation Radar (PR) (2A25) to gauge data in 1999, and found quite a bit of scatter in the relationship between gauge-estimated precipitation and the 2A25 precipitation. It is not clear whether the time intervals in the rain-gauge data match the satellite observations, which could add to scatter. More generally, instantaneous rainfall is sub-ideal for identifying periods of accumulated rainfall as we wish to in order to identify cloudbursts. Because of uncertainty in TRMM rainfall intensity products, particularly for the strongest rainfall events, we used daily rainfall data from 1980-2008 from the rain-gauge stations in Nepal to identify the “cloudbursts.” We used days with the heaviest rainfall as a proxy for the “cloudburst” events and will be referring to those as cloudbursts, hereafter. We also analyzed rainfall characteristics in the TRMM (3B42 version 7) product (TRMM rainfall hereafter) for the events that we identified using station data.

Daily rainfall data was obtained from the Department of Hydrology and Meteorology (DHM), Government of Nepal, except for rainfall data of the July 1993 cloudburst, which was recorded by the Department of Soil Conservation and Watershed Management of Nepal (Shrestha 1998). The daily rainfall reported is 24-hour accumulated rainfall recorded in the meteorological stations every day at 8:45 AM local standard time (3:00 UTC). The DHM is a member of the World Meteorological Organization (WMO) and follows the technical guidance of the WMO in establishing station network, installing

instruments, and collection and quality control of meteorological data. Any data that did not meet WMO quality standards are discarded (personal communication with Mr. Saraju Baidya, Deputy Director, DHM). Because erroneous data are common in a number of remote stations in Nepal, the precipitation dataset has many missing records. Therefore, only 94 out of 282 meteorological stations have complete data (no missing data) for July and August between 1980-2008. These 94 stations with complete data were used for the cloudburst identification.

Previous studies have also shown the reliability of published rain-gauge data from Nepal. For example, Yatagai et al. (2009, in supplement) used dense station network data from Nepal<sup>1</sup> after conducting their own quality control process for APHRO\_V0902 gridded data preparation. The acceptance of a large number of stations by their quality control process further suggests that most of the station data from the DHM are reliable. Yatagai et al. (2009) found that APHRO\_V0902 showed the least error among other gridded and satellite datasets when compared with independent data (not used to prepare APHRO\_V0902) in five selected watersheds of Nepal. These studies confirm the reliability of the daily gauge data from Nepal.

In this study, we subdivided Nepal into three regions longitudinally: the west (80-83E), the central (83E-86E) and the east (86E-88E) since we wished to do a composite analysis. In each region maximum daily rainfall records were sorted in descending order. The top ten daily maximum rainfall events during July and August in each region were identified. These events, in each region, are presented in Table 1 and the locations of the events are shown in Figure 3.1. Table 1 shows that the lowest value of daily rainfall among the top

---

<sup>1</sup> This can be inferred from the figures for individual years from 1961 to 2004 in the supplement material of Yatagai et al. [2009]

ten heavy rainfall events is about 222 mm. Therefore, based on daily rainfall, for the purposes of this study, we define events with daily rainfall of more than 220mm to be cloudbursts, and examine these events.

Table 1: Daily rainfall with dates recorded during the top ten “cloudburst” events in 3 regions of Nepal, ordered by highest rainfall amount in each region.

West region				Central region				East region			
Year	Month	Day	Rainfall (mm)	Year	Month	Day	Rainfall (mm)	Year	Month	Day	Rainfall (mm)
1981	7	31	380.1	1993	7	20	540.0	1987	8	11	377.6
2007	7	21	282.3	2003	7	31	456.8	1985	7	28	352.0
1986	7	21	281.2	1990	8	27	453.2	1980	8	21	336.0
1985	8	24	262.3	2002	7	23	442.5	1983	7	15	320.6
1996	7	19	240.7	2001	8	18	357.0	1989	7	2	290.5
1990	7	10	230.5	1996	7	14	354.0	2000	8	5	280.2
2006	7	9	225.0	2003	7	18	344.2	2005	8	27	256.8
1988	7	6	224.5	1987	8	1	320.0	1994	8	15	246.3
2002	8	20	223.2	2007	8	17	311.2	1981	7	4	240.2
1992	8	27	222.1	1986	7	10	298.5	1989	7	27	240.0

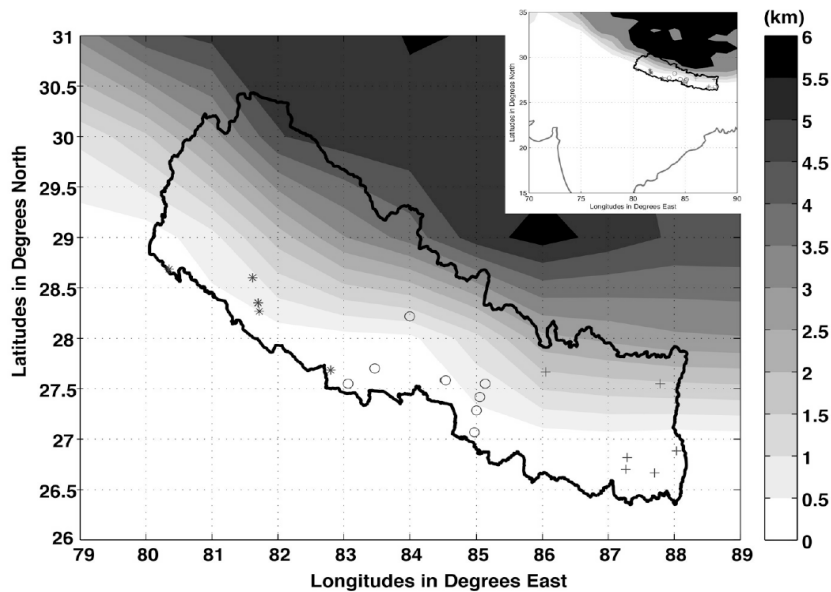


**Figure 3.1:** Station locations of the top ten maximum daily rainfall events in each region in Nepal during 1980-2008 along with topography. Cross: East region stations, Open circles: Central region stations, Stars: West region circles.

It is noteworthy that the top 10 events (Table 1) from the central region are among the top 15 heaviest rainfalls in all of Nepal, while only one event from the west and four from the

east regions ranked among the top 15. This pattern suggests that the central region of Nepal has the highest potential of occurrence of cloudbursts. Figure 3.2 presents the daily maximum rainfall distribution in Nepal during (1975-2008), which shows the pocket of the heaviest daily rainfall located in the central region (83-86E). Therefore, and because we chose to do a composite analysis of events close together geographically, this paper focuses on the cloudburst events in the central region of Nepal. Table 1 shows temporal variability in cloudburst occurrence in these three regions. In the eastern region cloudbursts occur most frequently in the 1980s while in central region, occurrences are mainly in the 1990s and in the 2000s. In the western region, the occurrences are equally distributed in three decades.

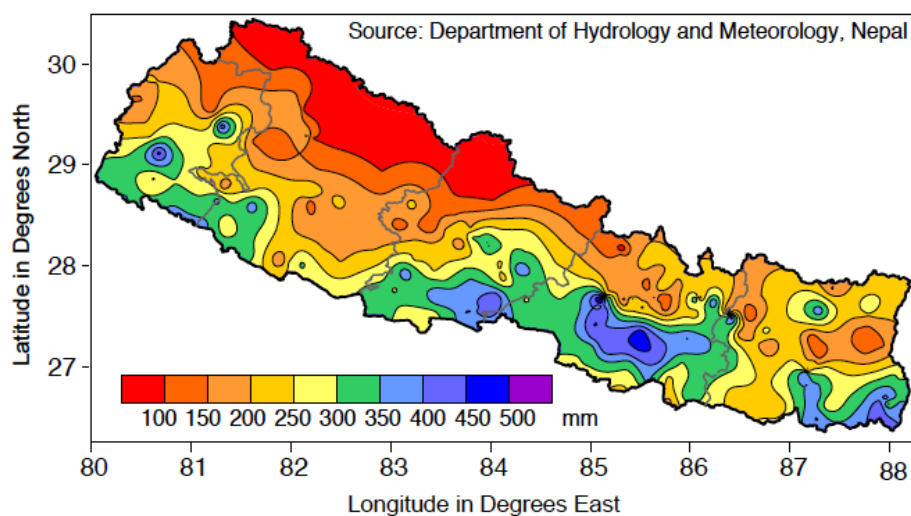


**Figure 3.2:** Distribution of daily maximum rainfall (mm) in Nepal during 1975-2008. Source: Prepared by Department of Hydrology and Meteorology, Nepal using Kriging Interpolation method in SURFER software.

### 3.1.1 Cloudburst Rainfall Analysis: Station verses TRMM data

Of the ten events in the central region of Nepal, only the July 1993 event has recorded hourly rainfall intensity (Figure 3.3a). The figure shows that the most intense rainfall, more than 40 mm/h, occurred in the 3-hour period between 9 PM and midnight local standard time (LST), with a second 3-hour peak in the early morning. Out of ten, for five events that occurred in the 21<sup>st</sup> century, 3-hourly average TRMM rainfall intensity data are available. Figure 3.3b shows the four-day (from one day before to two days after the cloudburst day) temporal variation of rainfall intensity from TRMM data (for the grid point with maximum rainfall intensity on the cloudburst day: Day 0). Similar to the station rainfall intensity pattern in the July 1993 event (Figure 3.3a), in all five cloudburst cases maximum rainfall intensity is concentrated in the three-hour period, either late night or early morning (Figure 3.3b). Only two events, July 2002 and July 30-31 2003, have maximum rainfall greater than 30 mm/h and only the July 2002 has a double peak: one in the late evening and the other in the early morning. As mentioned by Das et al. (2006), in all five cases, maximum rainfall intensity is concentrated for a short period of time (three hours).

TRMM rainfall intensities of these cloudburst events are considerably less (between 20 mm/h and 45 mm/h) than that mentioned in an unofficial definition of cloudbursts in Das et al. (2006), while the maximum intensity measured by the hourly gauge (65 mm/h in July 1993 cloudburst, Figure 3.3a) is similar in magnitude to that mentioned in Das et al. (2006). While no station data is available to make one on one comparison of TRMM and gauge intensities of cloudburst events, we should point out that lower intensities of cloudbursts in TRMM data might be due to the fact that TRMM rainfall intensity data is

an average intensity for a 0.25-degree grid rather than a point measurement in rain-gauge station data.

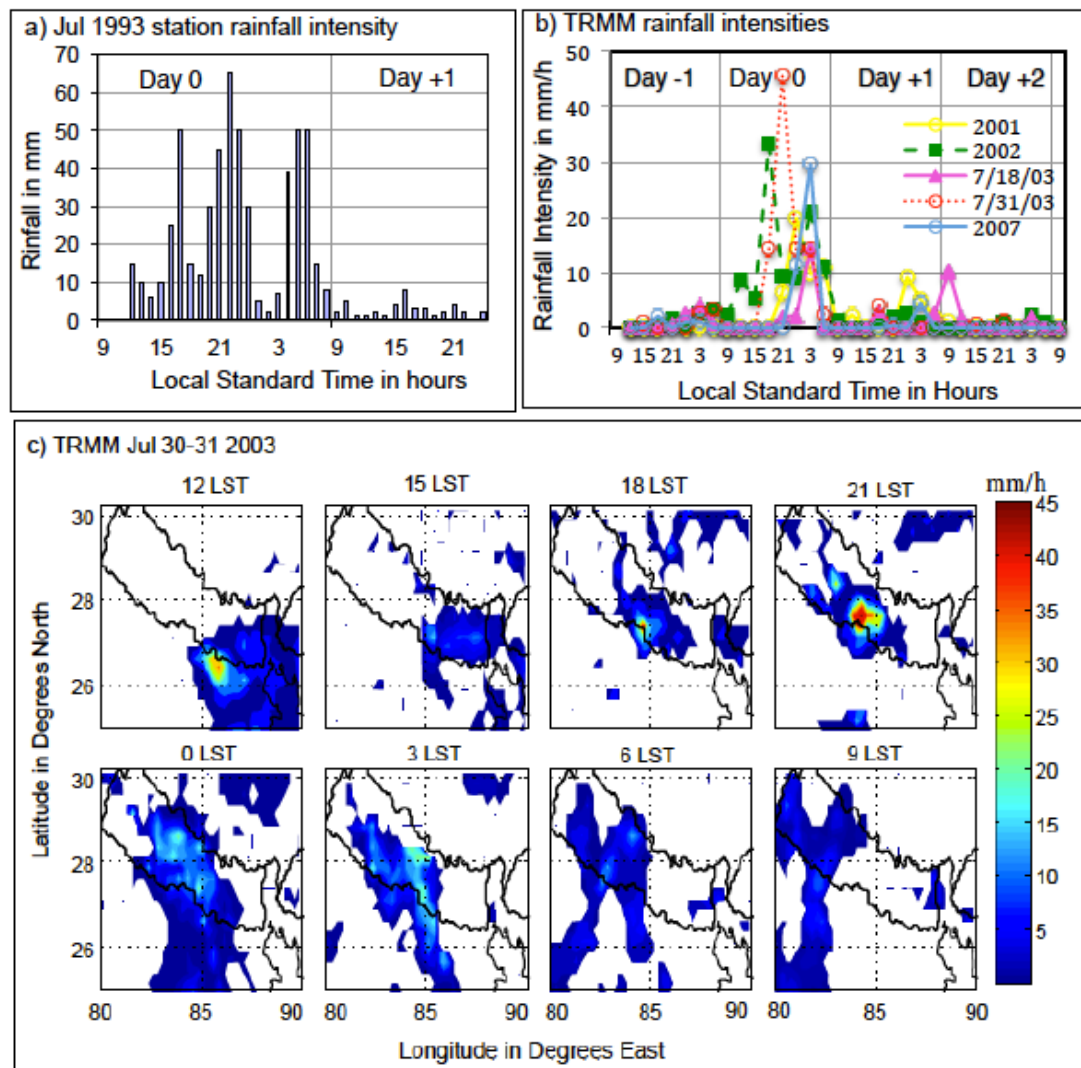


**Figure 3.3:** Rainfall intensity during cloudbursts in Nepal. a) Hourly rainfall intensity Kulekhani, Central Nepal, 19-20 July 1993 from station data, b) 3-hour average rainfall intensity for five 21<sup>st</sup> century cloudburst events from TRMM data, c) Evolution of spatial distribution of 3-hourly rainfall intensity based on TRMM data during 30-31 of July 2003 cloudburst (LST means local standard time). (TRMM data: 3B42 version 7)

The short period localized intense rainfall can be also observed in maps of the cloudburst event rainfall (Figure 3.3c). The figure shows spatial and temporal variation of rainfall intensity from TRMM data during the July 30-31 2003 cloudburst. During all of the five cloudburst events, for which TRMM data is available, the temporal and spatial

distributions of rainfall show similar localized short-period heavy rainfall (not shown here). However, the highest rainfall intensity in TRMM data for the other events is much less than in the July 30-31 2003 event.

We compared the spatial rainfall patterns of daily rainfall for the July 30-31, 2003 cloudburst event using station data (Figure 3.4a) and TRMM data (Figure 3.4b). The station rainfall distribution for July 31, 2003 is based on 197 rainfall stations without any missing data for July and August of 2003. Daily TRMM rainfall data was calculated from 3-hourly average TRMM rainfall intensity data. Again, as suggested by Das et al. (2006), strong localization of intense rainfall is observed in both rainfall data sets. We also examined the spatial distribution of rainfall for the remaining 9 events using station data (not shown here) and for 4 events of the 21<sup>st</sup> century using TRMM data (not shown here). Both datasets show the localization of heavy rainfall during cloudbursts. However, TRMM daily rainfalls show negative biases (-33% to -83%) and slight dislocation of the heavy rainfall pockets (e.g. Figure 3.4b) compared to the station rainfall distribution (e.g. Figure 3.4a). Similar spatial dislocations were observed during the other cloudburst events as well (not shown here). The bias was calculated as a percentage of the difference between TRMM rainfall and station rainfall, compared to the station rainfall on the cloudburst day. In this calculation, TRMM rainfalls of the grid point with the maximum value were used. This discrepancy could be either due to the different spatial resolution of the two data sets (TRMM data is averaged for 0.25-degree resolution while station data set is a point measurement) or it could be because the satellites used in TRMM data might have missed the heaviest rainfall episode of that event. Barros et al. (2000) suggested that TRMM rain rate performs best when the satellite overpass the storm. Therefore, further research is required to evaluate TRMM rainfall data with *in situ* data on rainfall intensity,

when focusing on extreme events in Nepal. In our analysis, we choose to use the gauge data to identify cloudbursts.

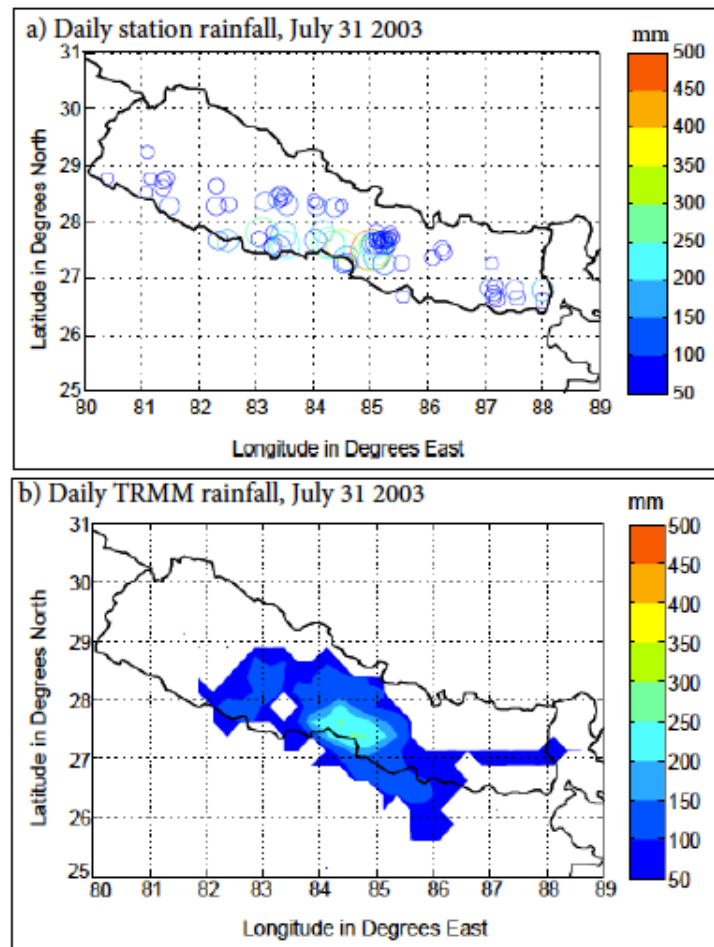


**Figure 3.4:** Spatial distribution of daily rainfall (mm) during the July 30-31 2003 cloudburst events. a) Rain gauge station data plot (size and color of circles represent rainfall magnitude expressed in the color bar). b) Calculated from 3-hourly TRMM Data (3B42 version 7)

## **3.2 Methodology**

This section discusses the methods and data used to achieve Objective 2, Objective 3 and Objective 4.

### **3.2.1 Composite Analysis: An Approach to Achieve Overall Goal of the Research**

Cloudburst composites were prepared by taking the average of the synoptic conditions of the top ten cloudburst events (Table 1) in the central region. For synoptic analysis, there is no *in situ* upper-air data in the Nepal Himalayas. Reanalysis data is the only meteorological data available for the synoptic analysis in this region. This study used ERA-Interim (European Centre for Medium-Range Weather Forecasts Reanalysis) data for synoptic analysis of the cloudbursts and monsoon climatology. ERA-Interim data is one among the high-resolution reanalysis data sets with good performance in this region (Bao and Zhang 2012; Wang and Zeng 2012; Demott et al. 2013). The horizontal resolution of the ERA-Interim data is 0.703 degrees and the data have 60 vertical levels up to 0.1 hPa (European Centre for Medium-Range Weather Forecasts 2009). To compare the cloudburst conditions with the normal monsoon synoptic conditions we also used the July-August ERA-Interim climatology for the period from 1981 to 2010.

### **3.2.2 Significance t-test**

The significance of the composite analysis results was tested using the Student's T test. This test was specifically used to test the Hypothesis 1 that if the synoptic features of cloudbursts are significantly different from the normal climatology. One of challenges of using this tool is the estimation of degrees of freedom (DOF) in dependent samples. While 10 cloudburst events are independent of each other, the samples in the climatological data series are not independent to each other. Leith (1973) and Bretherton

et al. (1999) introduce a method to estimate modified degrees of freedom using effective independent sample size. The number of independent sample size was estimated from autocorrelation values. These study found that larger the autocorrelation smaller would be the degrees of Freedom. Hartmann (2016) prepared a graph on relation between the ratio between effective independent samples size to original sample size and autocorrelation between data points (Figure 3.5). This study uses this graph to estimate effective independent samples size and degrees of freedom.

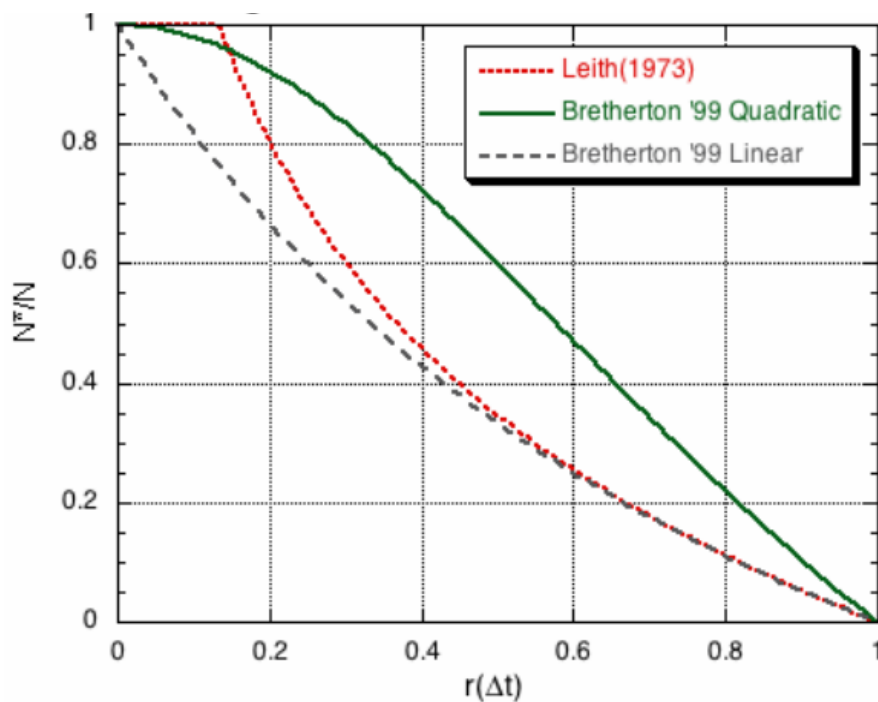


Figure 3.5: Comparison of the ratio of effective sample size to actual sample size for Leith (1973) and Bretherton et al. (1999) formulas as a function of  $r(\Delta t)$ . ( $r$  is autocorrelation coefficient and  $\Delta t$  is time step. Figure adopted from Hartmann (2016).

### 3.2.3 Objective 2: Identification of Favorable Synoptic Conditions of the Cloudbursts

Composite analysis of ten cloudburst events in the central Nepal performed to identify the synoptic features of cloudbursts. To understand the relation between synoptic features time evolution of cloudburst composites were done from 2 days before the event to 2

days after the events. In each case significant test was performed using most conservative autocorrelation value of 0.8 to estimate the degrees of freedom. With this autocorrelation value and using Leith (1973) and Bretherton (1999)-Linear curves, the effective sample size ( $N^*$ ) becomes 186 for total number of sample size for dependent time series,  $N=1860$ . Therefore degrees of freedom will be estimated using effective sample size.

### 3.2.4. Objective 3: Enhanced Northward Tropical-extratropical Interaction

To examine enhanced northward tropical-extratropical interaction a number of analysis was done. Knippertz (2007) used the strength of the local Hadley circulations to show stronger tropical extratropical Interaction. Riehl (1977) discussed transport of heat, mass and momentum from tropics to extratropics during deep trough intrusion to the tropics. In this research strength of the local Hadley cells and northward momentum transport was analyzed.

#### a) Local Hadley Cell

Strength of the local Hadley cell (mean meridional circulation) was computed from the mass streamfunction expression as below:

$$\psi_p = \frac{2\pi a \cos\phi}{g} \int_p^{1000} v dp$$

where,  $a$  is the radius of the earth,  $\phi$  is the latitude of the earth,  $v$  is the meridional wind and  $dp$  is the pressure increments from the surface to the top of the atmosphere. Then the streamfunction was averaged for the respective longitudes to obtained local Hadley cells. It is noteworthy that streamfunction here is different from the zonally (global) averaged streamfunction, which gives the mass circulation in latitude-altitude plane. In the present study, because streamfunction is calculated from the meridional wind, the meridional branch of the streamfunction contours represent true meridional

flow while the vertical branch only provides the qualitative structure of the vertical flow.

**b) Northward Momentum Transport by Mean Meridional Circulation**

Transport of westerly momentum by mean meridional circulation was computed using following expression:  $[\bar{v}][\bar{u}]$

where,

$[\bar{v}]$  is the zonal average of time mean meridional wind

$[\bar{u}]$  is the zonal average of time mean zonal wind

The positive value of  $[\bar{v}][\bar{u}]$  gives the northward transport of westerly momentum by mean meridional circulation. Time mean for climatology is 30-year period (1981-2010) and time mean for cloudbursts is mean of ten cloudburst events.

**c) Northward Momentum Transport by Transient Eddies**

Transport of westerly momentum by transient eddy is computed as:  $[v'u']$

where,

$v' = v - \bar{v}$  is the deviation of meridional wind from time mean

$u' = u - \bar{u}$  is the deviation of zonal wind from its time mean

The positive value of  $[v'u']$  gives the northward transport of westerly momentum by transient eddies.

**d) Momentum Flux Divergence by Transient Eddies**

Transient eddy momentum flux divergence was calculated using following expression:

$$\nabla \cdot ([v'\vec{u}'] \cos\phi)$$

where,  $\vec{v}$  is the horizontal velocity vector = (u, v)

The positive values of above expression mean the flux divergence while negative values mean northward flux convergence.

### **3.2.5 Objective 4: Association of Tropical Heating in Triggering Tropical-Extratropical Interaction During the Cloudbursts**

Following two steps were taken to examine the role of tropical heating on tropical-extratropical interaction during cloudbursts.

#### **a) Upper-level Force Balance Approach**

The importance of a force balance approach to understand tropical extratropical interaction was discussed in Chapter 2, section 2.3.1. In this research, Petterssen (1953) expression (Eq. 2) for force balance analysis was applied on an isentropic surface 370K. The square of right hand side of this term of Eq. 2 is named as force balance parameter ( $\alpha$ ): for the convenience and thus becomes:

$$\alpha = (Q^2 - A^2 - B^2 - D^2 - 2\beta * u) * 0.5 \text{-----(5)}$$

From Eq 2 and Eq 5, when  $\alpha$  is positive, the pressure field has real solutions, which indicates pressure field is balance by the sum of terms in the right hand side. It is noteworthy that  $\alpha$  is positive when absolute vorticity is greater than sum of the non-linear terms (deformation and divergence and beta effect). When  $\alpha$  is negative, the pressure field has imaginary solution, which means pressure field is not balanced by the sum of restoring forces. This condition can occurs when non-linear terms mainly deformation and divergence terms are much larger than the absolute vorticity thus leaving pressure field unbalanced. In such case deformation and divergence can lead to northward resulting flow and enhanced tropical-extratropical interaction.

To examine upper-level for balance, force balance parameter was calculated for 370K isentropic surface for each cloudburst event and composite maps are prepared for the period from -6 days to +5 days. Negative  $\alpha$  north of the Nepal Himalayas should represent weak restoring force compare to the pressure gradient force

Further to show that during the cloudbursts events the pressure field exceeds the restoring forces in the northern side of the Nepal Himalayas compared in the south side of the Himalayas, the ratio of Montgomery streamfunction gradient to inertial force was computed for 370K surface.

#### **b) Eddy Shedding Process**

To understand to role of the tropical heating, negative OLR anomaly was computed for cloudburst composite, which will give the tentative location of the tropical heating. Then, westward eddy shedding mechanism was analyzed using time evolution of cloudburst composite of 370K surface Montgomery streamfunction high and potential vorticity lower than 1.5PVU from -7 days before to +5 days from the cloudburst day.

Since it is well established that upper-level Tibetan anticyclone during the monsoon season is one of the features of the linear dynamic response of the monsoonal heating (Gill 1980; Hoskins and Rodwell 1995). This study did not intended to show the changes in anticyclone during the cloudbursts is due the monsoonal heating; but rather considered this relation is obvious and thus intended to establish association between the location the tropical heating anomaly and the enhanced tropical-extratropical interaction during the cloudburst via eddy shedding process.

## Chapter 4

### Cloudburst Synoptic Features: Composite Analysis

This chapter presents the composite analysis of ten cloudburst events to identify the upper-level and surface synoptic features. The focus of the analysis in this chapter will be on the synoptic features discussed in Chapter 2. This chapter first lays out the climatology of synoptic conditions during monsoon and compares upper-level jets, upper-level westerly trough, positive potential vorticity and vertical motion during cloudbursts with the climatology. To understand relation between the synoptic features time evolution of these features were prepared and also the conceptual model of cloudburst mechanism is presented.

#### 4.1. Synoptic Climatology during July-August

Figures 4.1a and 4.1b present the July-August climatology of wind with geopotential height for 200 hPa and 125 hPa isobaric levels respectively. These levels were chosen because the westerly and easterly jets have their maximum strength there (Randel et al. 2007; Roja Raman et al. 2009). Climatologically, westerly jet (WJ) cores (30 m/s) are centered at about 43N and 90E, at the 200 hPa level (Figure 4.1a). The easterly jet (EJ) core, maximum at 125 hPa level, is centered at about 12N 70E (Figure 4.1b). The EJ core is about 5 m/s stronger than the WJ core and occupies a larger area. Figures 5a and 5b also show that in the western Himalayas, north of 30N (northwestern Indian and northern Pakistan), upper air winds are weak westerlies while in the central and eastern Himalayas (over Nepal and northeastern India) the wind aloft is mainly very weak easterly. These upper-level features are consistent with favorable conditions mentioned by Houze et al. (2007) for deep intense convection in the western Himalayas, wide intense convective

system in the lowlands and broad stratiform convective systems in the eastern and central Himalayas.

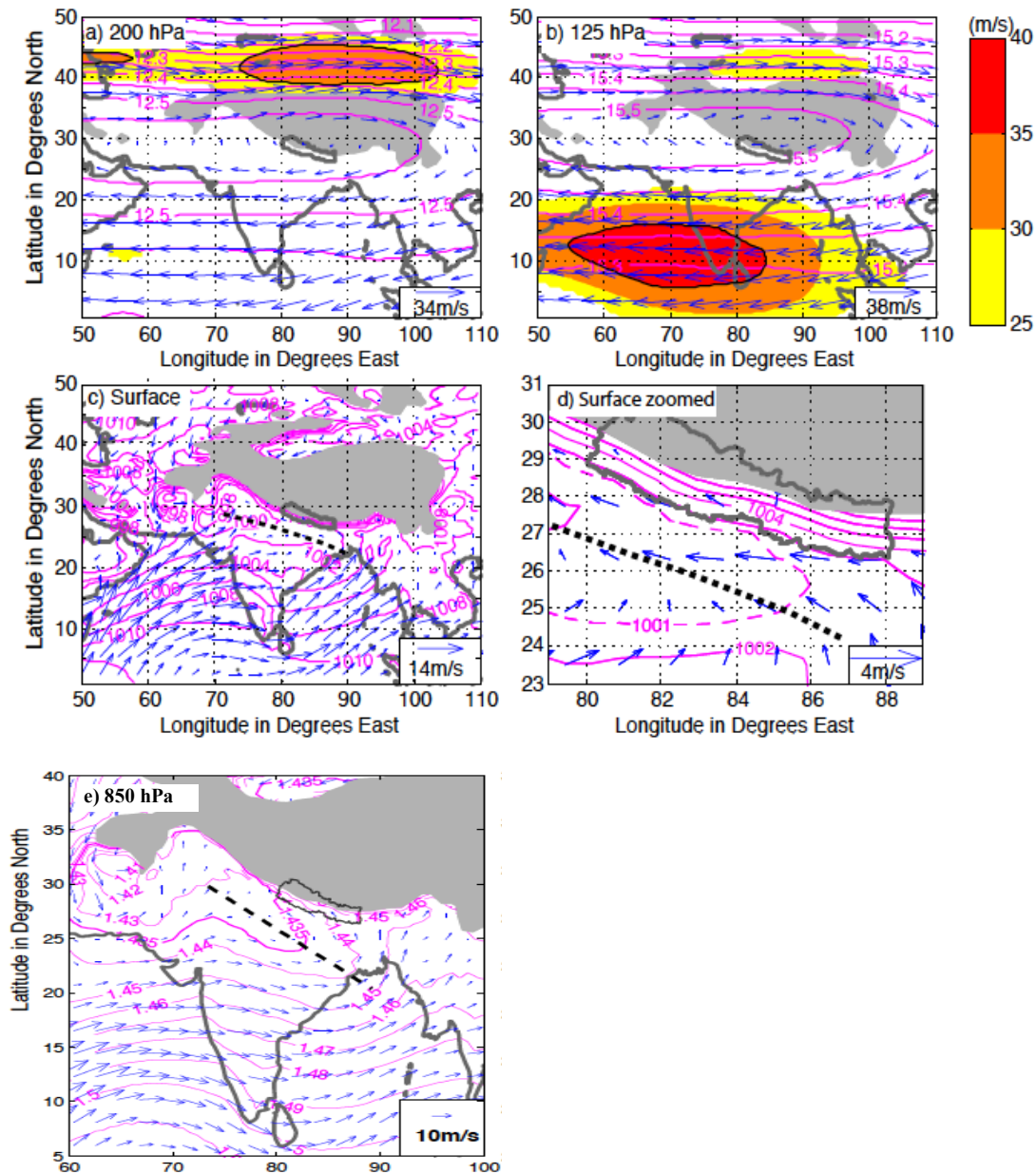


Figure 4.1: ERA-Interim July-Aug 18 UTC climatology (1980-2010). a) 200 hPa wind speed (shading, m/s), geopotential height (magenta contours, km), 28 m/s westerly jet core (black contour); b) 125 hPa total wind speed (shading m/s) and vectors, geopotential height (magenta contours, km), 35 m/s easterly jet core (black contour); c) surface total wind (vectors), mean sea level pressure ‘MSLP’ (magenta contours, hPa), approximate location of the monsoon trough axis (thick black dash line); d) same as (c) but zoomed over Nepal with MSLP at 1 hPa interval. D) 850 hPa geopotential height pattern. Gray shading in a, b c and d represents the Tibetan Plateau and the Himalayas with elevation higher than 2000 m above sea level.

Climatologically, the monsoon trough of surface low-pressure area is located in the northern plains of India, extending almost parallel to the Himalayas. Figure 4.1c shows the climatology of mean sea level pressure (MSLP), which depicts a northwest-southeast oriented monsoon trough extended from Pakistan to the Bay of Bengal almost parallel to the Himalayas. Although MSLP often does not adequately depict the horizontal variability of pressure in a mountainous region, it is used in this analysis to locate the monsoon trough, which is climatologically located over the Plains in Northern India. Close examination of the monsoon trough in the geopotential height maps for 850hPa (Figure 4.1.e), suggests that the monsoon trough in 850hPa is adequately depicted by the MSLP analysis. Figure 4.1d shows wind around the monsoon trough near the Nepal Himalayas. The wind circulation around this trough leads the surface wind to be easterly from the Bay of Bengal in the north of the monsoon trough and westerly from the Arabian Sea in the south of the monsoon trough. The easterly surface flow from the Bay of Bengal north of the monsoon trough over the Nepal Himalayas is lifted by the topography. This flow north of the trough is more supportive of stratiform precipitation than convective precipitation over the foothills of the Nepal and eastern Indian Himalayas (Houze et al. 2007; Shrestha et al., 2012).

## **4.2 Cloudburst Composite Analysis**

Cloudbursts in Nepal normally occur late at night or early morning (Figure 3.3a). The composites and their anomalies were prepared for 18 UTC (midnight local standard time) of the storm day. The significance of these anomalies was analyzed using T-test with 95% confidence level. We also compared these anomalies with the climatological

standard deviation. This section presents analysis of upper and lower troposphere synoptic features before, during and after the cloudburst events.

#### **4.2.1 Jet Streams and Upper-Level Troughs**

Figure 4.2 shows the evolution of an upper-level trough north and slightly west of central Nepal and shifts in the easterly and westerly jets compared to the climatology from 2 days before to 2 days after the cloudburst event. The left panel (Figure 4.2a) and right panel (Figure 4.2b) represent evolving condition at 200 hPa and 125 hPa respectively. The left panel (Figure 4.2a) shows a westerly trough (negative geopotential anomaly) located north-northwest of Nepal that deepens from two days before ( $\sim -40$  m) until the cloudburst day ( $\sim -80$  m) and starts weakening afterwards. The figure also shows southward shift and expansion of this trough. This trough is significant at the 95% level from one day before the event. This trough extends to 125 hPa (Figure 4.2b) and a similar time evolution is visible at 125 hPa. According to QG theory an advection of cyclonic vorticity and divergence of ageostrophic wind is maximum east of the upper-level troughs, and this advection and divergence has a tendency to support surface cyclonic circulations beneath (Martin 2006, pp 150,163). It is noteworthy that the upper-level trough associated with the cloudbursts to the north-northwest of Nepal might play a role in producing the surface disturbance over Tibet and in the Nepal Himalayas (results shown in the sub-section 4.2.2). Presence of the Himalayas appears to be responsible for the cloudbursts occurring southeastward of the upper-level trough (which is located over the southern slopes of Nepal Himalayas) rather than further north directly to the east of the upper-level trough.

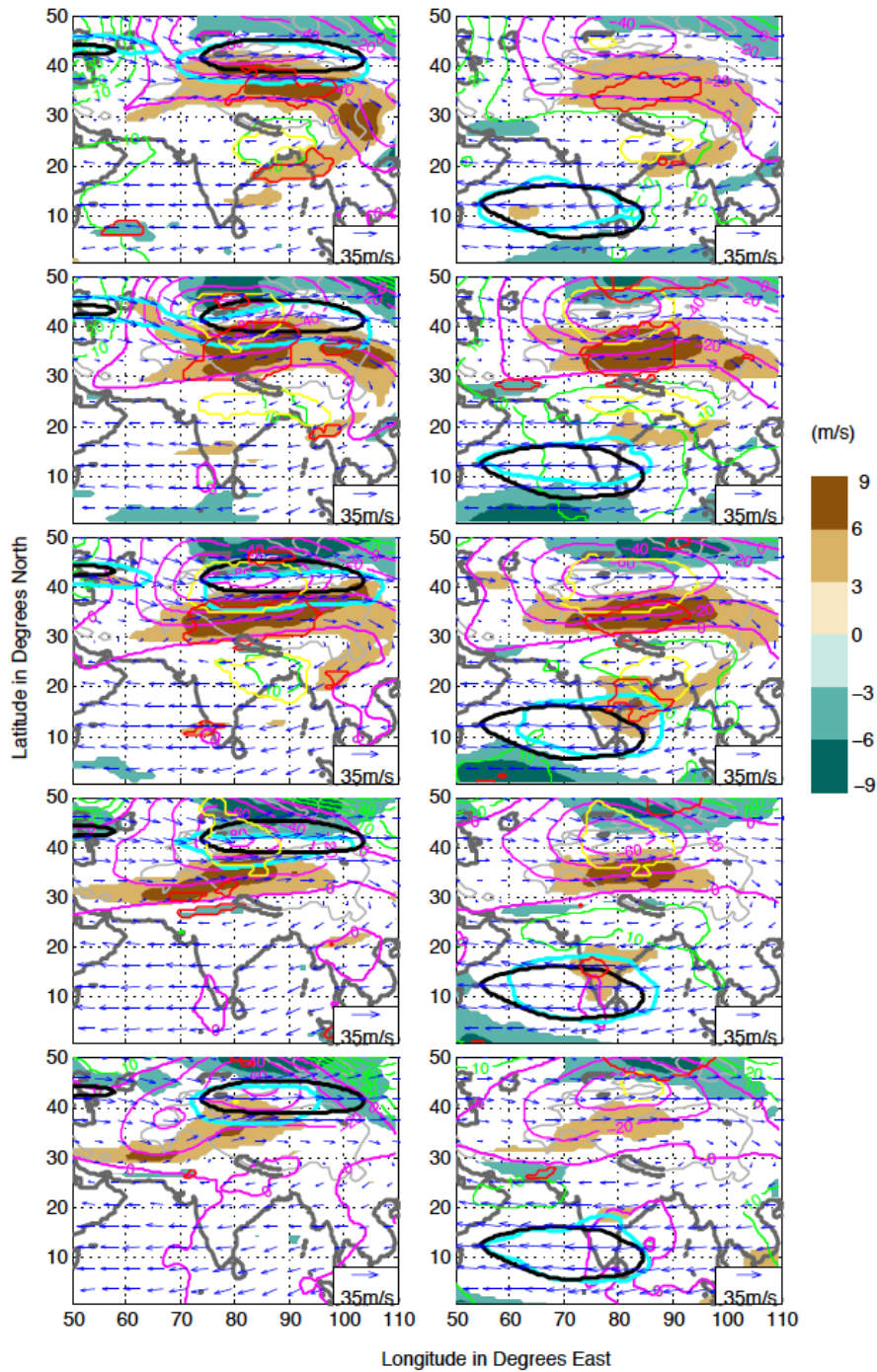


Figure 4.2 Evolution of composite upper-level geopotential height anomalies and wind speed anomalies from two days before (-2 day) to two days after (+2 day) the cloudbursts. a) Left panel is 200 hPa; b) Right panel is 125 hPa. 0 day is cloudburst day. Blue vectors: total wind (m/s), shading: wind speed anomaly (m/s), Magenta contours: Negative GPT anomaly (20 m interval), Green contours: Positive GPT anomaly (10 m interval), Yellow contours: 95% significance of geopotential anomaly, Red contours: 95% significance of wind speed anomaly, Black contours: climatological jet core (35 m/s, 125 hPa and 30m/s, 200 hPa), Cyan contours: Cloudburst jet core (35 m/s, 125 hPa and 30 m/s, 200 hPa), Gray thin contour: 2 km elevation above sea level.

Figure 4.2a also shows the evolution of westerly jet shift before, during and after the cloudbursts. The WJ core speed intensifies and shifts southward from 2 days before the event until the day of the event and then retreats and weakens. The wind speed anomaly is positive to the south of the climatological WJ core (Figure 4.2a). The magnitude and extension of this positive wind anomaly is maximum on the day of the events and weakens from one day past the event. The positive anomaly is significant at 95% confidence level from 2 days before the event to the event day. Hence, the southward shift of the WJ core ( $\geq 30$  m/s; east of 80E) near Nepal during the cloudburst is significantly different from climatology. It is noteworthy that strong positive anomaly is over the southern side of the entrance region of this jet core, which suggests that the entrance region shifts southward more than the exit region. The southward shift of the WJ entrance also suggests a southward shift of the associated rising branch (located south of the jet entrance) of the direct circulation. Quasi-geostrophic analysis would suggest that this would be associated with rising motion on the southern slopes of the Himalayas, which would then likely play some role in creating favorable conditions for the occurrence of the cloudbursts.

Figure 4.2b shows the evolution of the EJ core at 125 hPa. The entrance region of EJ core ( $\geq 35$  m/s) extends northeastward from one day before events with maximum extension on the day of the event and it then retreats afterwards compared to its climatological position. The wind anomaly shows that the EJ speed during the cloudburst is stronger in the northeast (significant at 95% level) and weaker in the southwest of the jet core than in the climatology in this five-day period, which indicates significant northeastward shifts of the EJ entrance. The monsoonal rainfall pocket in the eastern and northeastern parts of

South Asia has been attributed by Koteswaram, (1958) to the large-scale ascent associated with the direct circulation around the EJ entrance region. Other studies also suggest the applicability of the quasi-geostrophic (QG) approximation in low-latitude large-scale synoptic features with a low Rossby number (Ro) (Flohn 1964; Hastenrath 1991; Grist et al. 2002), which supports the suggestion that a relationship between large-scale rising motion and the location of the EJ may occur. Grist et al. (2002) successfully applied the QG approximation to the African easterly jet (at 15N) with a Ro of about 0.25. We found a similar Ro ( $\sim 0.24$ ) for the EJ core. With the northeastward shift of the EJ entrance region during the cloudbursts, the large-scale rising branch associated with the EJ entrance (north of the jet entrance) may have shifted northward closer to the Nepal Himalayas, playing a role in enhancing rising motion and in the anomalous rainfall during cloudbursts (discussed in sub-section 4.2.4).

On the cloudburst day, the easterly and westerly jets were about 17 degrees apart, while in the climatology they are typically about 23 degrees apart. Both of these figures (Figure 4.2a and Figure 4.2b) show that the entrance regions of both jets are co-located and closer to the Nepal Himalayas such that their rising branches are closer to the Nepal Himalayas. Thus co-location and closer proximity of the two jet entrance regions could create favorable conditions for large-scale ascent for the cloudbursts in the Nepal Himalayas.

#### **4.2.2 Surface Synoptic Conditions**

Figure 4.3 shows the evolution of the MSLP and surface wind from 2 days before to 2 days after the cloudbursts. The left panel (figure 4.3a) depicts a northward shift (and intensification) of the monsoon trough towards the Himalayas from 2 days before the event to the day of the event. It is clear from Figure 4.3a that during the cloudburst day

and a day prior to the events, the MSLP is lower than 1000 hPa in the southern slopes of the Nepal Himalayas, while on 2 days before the event and after the event days, the MSLP is higher than 1000 hPa in this region. This figure also shows that the trough axis on the cloudburst day (0 day) is shifted northward towards the Himalayas (Figure 4.3a) compared to the climatological location (Figure 4.1c). Figure 4.3b (middle panel) presents the evolution of monsoon trough and surface with zoomed over Nepal region. Northward shift of monsoon trough towards Nepal is clearly evident in Figure 4.3b. This figure also shows the evolution of surface flow from easterly to southwesterly towards the Nepal Himalayas from two days before until the cloudburst day and returning to normal (climatological: black vectors) easterly flow afterwards. This southwesterly surface flow suggests that flow in the Nepal Himalayas is from the Arabian Sea during the cloudbursts (Figure 4.3b, blue vectors) in contrast to climatological conditions when the flow in the Nepal Himalayas is easterly from the Bay of Bengal (Figure 4.3b: black vectors).

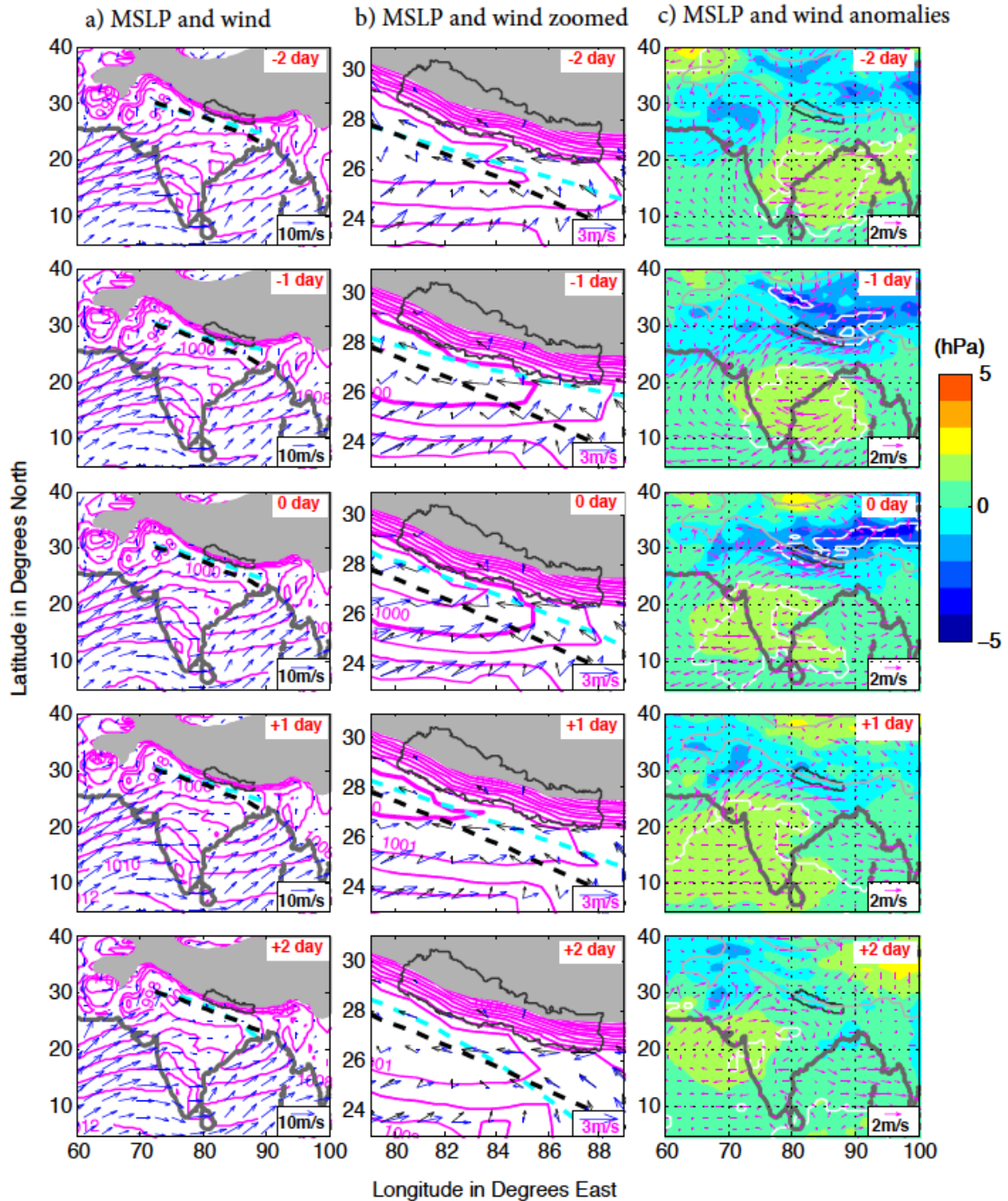


Figure 4.3 Evolution of composite surface synoptic features from two days before (-2 day) to two days after (+2 day) the cloudburst day. 0 day is cloudburst day. a) Surface total wind vectors, MSLP (magenta contours at 2 hPa interval; b) Comparison of the cloudburst surface wind (blue vector) with climatology (black vector) zoomed over Nepal, MSLP (magenta contours at 1 hPa interval); Gray shading in (a) and (b) represents area with topography > 2 km above sea level, black dashed line: climatological monsoon trough and cyan dashed line: cloudburst composite monsoon trough. c) Surface wind anomaly (vectors), MSLP anomaly (shading), 95% significant level (white contour); Gray thin contour: 2 km elevation above sea level.

Figure 4.3c (right panel) shows the evolution of negative MSLP anomaly over Tibet deepening and extending to the Nepal Himalayas from 2 days before until the cloudburst day (0 day) and weakening afterwards. Time evolution of surface pressure anomaly for this 5 day period was also examined (not shown here) and the anomaly is similar to the MSLP anomaly and thus justifies the use of MSLP in this case. The center of this negative anomaly over Nepal and Tibet is at 95% significant one day before and on the day of the events. It is noteworthy that the negative MSLP anomaly over the Nepal Himalayas and Tibet is situated east of the upper-level trough, suggesting westward tilt with height in the disturbances associated with cloudbursts. The negative MSLP anomaly over the Nepal Himalayas (and in Tibet) and the upper-level trough located north and slightly to the west of Nepal (Figure 4.2a and 4.2b) suggests the influence of the upper-level trough in the formation of a surface disturbance in the Nepal Himalayas as discussed in the section 4.2.1. The northward shift of the monsoon trough to the foothills of the Himalayas might be associated with this surface low formation over the Himalayas due to the upper-level trough. It is noteworthy that a positive MSLP anomaly and anticyclonic wind anomaly is observed over central India (Figure 4.3c). The positive MSLP anomaly, perhaps, may have facilitated the southwesterly surface flow from the Arabian Sea towards the Himalayas (Figure 4.3a and 4.3b two days before and one day before cloudburst day) in contrast to the climatological westerly flow from the Arabian Sea in central India to the Bay of Bengal (Figure 4.1c). This anticyclonic surface wind anomaly over India during the cloudburst events likely led to low-level flow almost perpendicular to the Himalayas triggering the extreme precipitation.

Figure 4.4 shows the evolution of monsoon trough and winds at 850 hPa isobaric level and also evolution of geopotential height anomaly at 850 hPa. The pattern of northward

shift of monsoon trough during the cloudburst at 850 hPa is similar to that in the MSLP level.

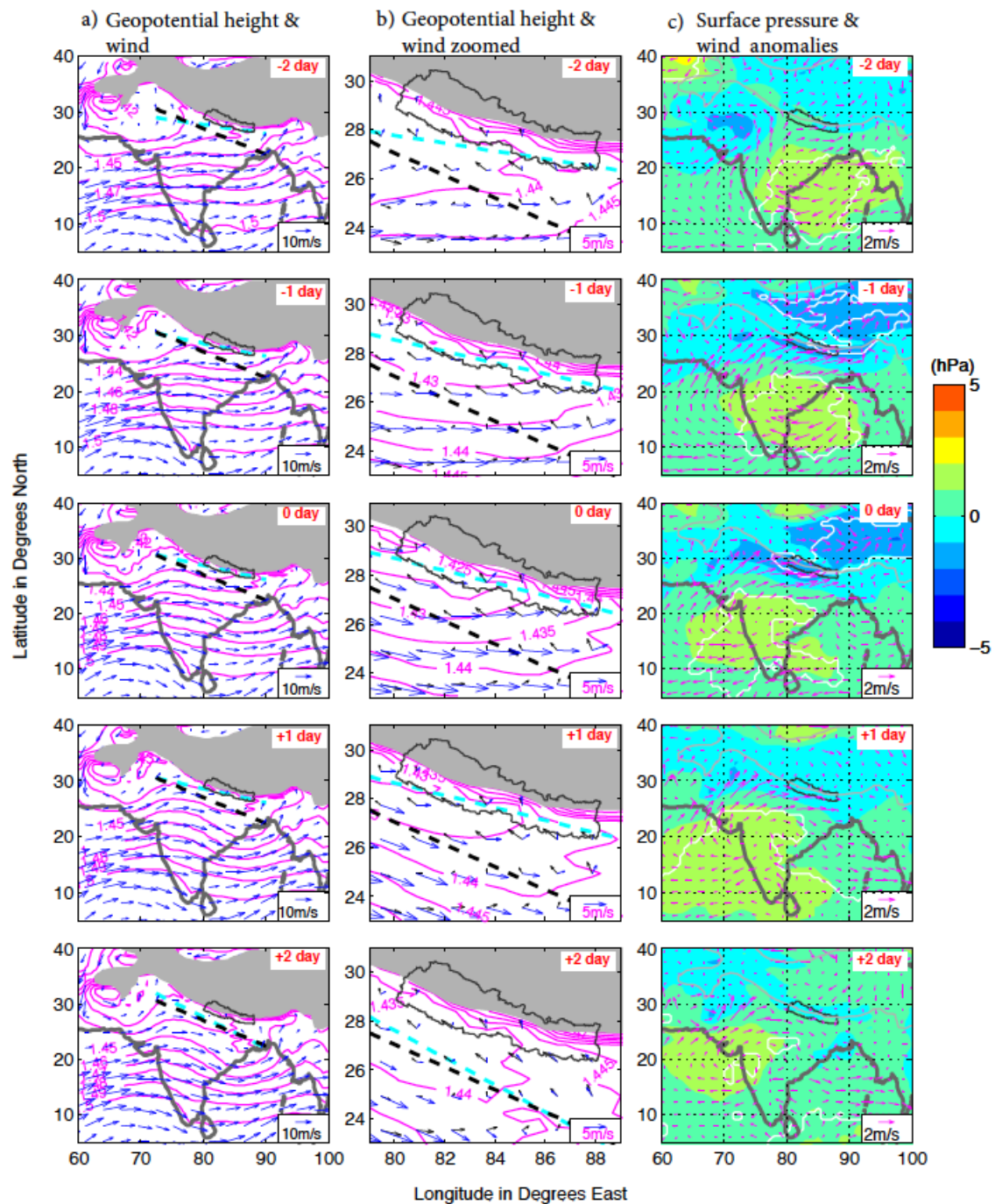


Figure 4.4 Evolution of composite 850 hPa and surface synoptic features from two days before (-2 day) to two days after (+2 day) the cloudburst day. 0 day is cloudburst day. a) 850 hPa total wind vectors, 850 hPa geopotential height (GPH)(magenta contours km; b) Comparison of the cloudburst 850 hPa wind (blue vector) with climatology (black vector) zoomed over Nepal, 850 hPa GPH (magenta contours at 0.005km interval); Gray shading in (a) and (b) represents area with topography > 2 km above sea level and dashed line represents monsoon trough. c) Surface wind anomaly (vectors), surface pressure anomaly (shading), 95% significant level (white contour); Gray thin contour: 2 km elevation above sea level,

### 4.2.3 Upper-Level Potential Vorticity (PV)

Figure 4.5a depicts the evolution of the tropopause fold and the associated upper-level PV anomaly during the five-day period. The vertical distribution of 1.5 PVU averaged between 85-86E longitudes shows a steeper tropopause fold extending towards the Nepal Himalayas during the cloudburst than in the climatological conditions. The 1 PVU surface has intruded below 300 hPa. It is noteworthy that some of the Nepalese Himalayan peaks are higher than 8 km, i.e., approximately 400 hPa. The steep tropopause fold is particularly evident for an individual cloudburst event (July 1993 cloudburst not shown here). The vertical distribution of PV anomaly (averaged between 85-86E longitudes) shows the positive upper-level PV anomaly, significant at 95% confidence level, two days before the event at 45N. This PV anomaly grows and shifts southward until the cloudburst day and retreats afterwards.

The upper-level positive PV anomaly associated with the tropopause fold superpositioning with the elevated topography could be an important factor in deepening the surface low and enhancing rising motion during the cloudbursts. A positive PV anomaly associated with a deep tropopause fold over high mountains appears to couple with the elevated topography and establish a favorable coherent environment for surface low deepening (Arreola et al. 2003). Massacand et al. (1998) suggested that the north-south oriented upper-level PV anomaly streamer, during heavy precipitation over the European Alps, produced favorable conditions by reducing static stability beneath the anomaly, setting up rising motion in the forward flank (southward) of the anomaly, and enhancing a moist southerly flow component towards the mountains. Similar dynamics might have played a role during the cloudbursts in the Nepal Himalayas, with an upper-level positive PV anomaly north of the elevated Himalayas and a surface low over the Nepal

Himalayas, encouraging strong rising motion over the southern slopes of the Himalayas. The elevated topography may play a critical role in producing a “wall effect” which leads to the surface convergence region associated with moist low-level air flow over the mountain slope (Homar et al. 2002).

While above studies provide evidence of the association of upper-level PV anomaly and heavy precipitation in the mid-latitudes, the application of the quasi-geostrophic (QG) approximation in the subtropics may have significant error because of the low values of the vertical Coriolis parameter ( $f$ ). However, the topography may make QG theory more applicable than it typically is at the latitudes in question. Hoskins et al. (1985) discussed vertical extent (Rossby height) of the typical synoptic scale upper-level disturbance. At low latitudes, the vertical influence of a tropopause disturbance is smaller compared with the one in the mid-latitudes. The expected depth of the QG circulation in the low latitudes (<30N) tends to be too shallow to reach the surface, but high ground in the Himalayas may allow the upper-level trough and the PV anomaly to influence the surface circulation and the secondary circulation around the WJ to reach the surface. Therefore, it is possible that, even though the effective depth of the upper-level disturbance is shallow, the elevated topography of the Himalayas may provide a unique condition for the interaction of the upper-level PV anomaly with the surface low. Moreover, recent studies on the role of the upper-level PV anomaly on extreme events in the South Asian subtropics further support our analysis. For example, Hong et al. (2011) and Martius et al. (2013) attributed the forced orographic lifting of moist layer from the Arabian Sea to the upper-level PV anomaly during the July 2010 Pakistan flooding .

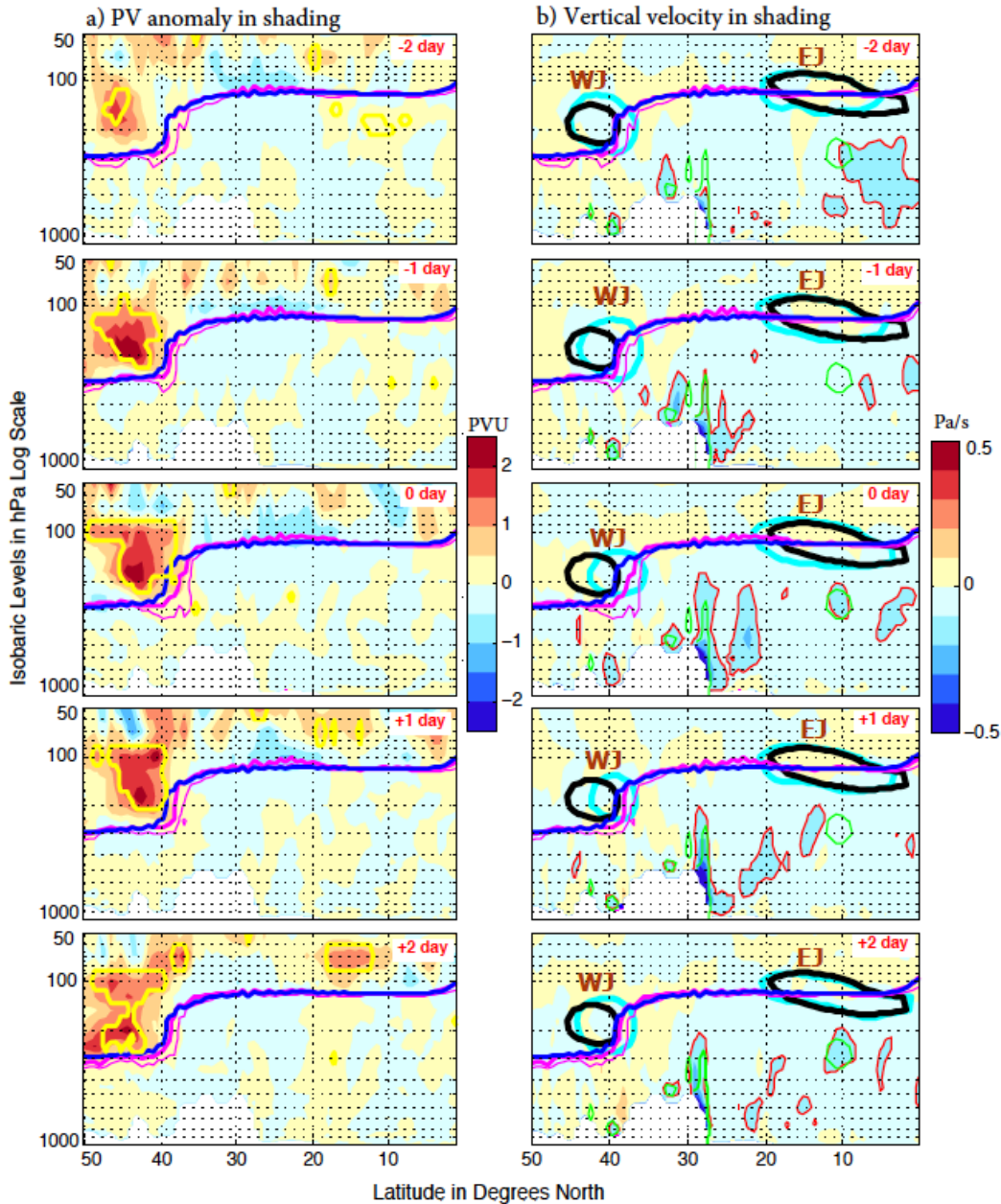


Figure 4.5: Vertical cross-section (averaged over 85-86E) showing evolution of composite PV anomaly and vertical velocity from two days before (-2 day) to two days after (+2 day) events. 0 day is cloudburst day. a) Potential vorticity (PV), shading: PV anomaly, yellow contour: 95% significance level of positive PV anomaly above 300 hPa, Thick magenta: 1.5 PVU surface and thin magenta: 1 PVU surface, Blue contour: 1.5 PVU surface in climatology, b) Vertical velocity (shading), red contour: cloudburst 0.2 Pa/s, green contour: climatological 0.2 Pa/s, Thick magenta: PV of 1.5 PVU surface and thin magenta: 1 PVU surface, Blue contour: 1.5PVU (PV climatology); Cyan contour: 30 m/s jet cores (cloudburst), Black contour: 30 m/s jet cores (climatology), White shading represents topography.

#### 4.2.4 Vertical Velocity

The possible association of the five upper-level and surface cloudburst synoptic features with rising motion was discussed in Section 4.2.1-4.2.3. In this section, the evolution of vertical motion before, during and after the cloudburst event was examined. Figure 4.5b depicts the evolution of vertical velocity (averaged between 85-86E longitudes) from 2 days before to 2 days after the cloudburst (red contour: 0.10 Pa/s) and WJ and EJ cores, along with the climatological (green contour: 0.10 Pa/s) vertical velocity and WJ and EJ cores. The magnitude of the vertical velocity does not represent the localized convective scale vertical velocity, which might be larger. Two days before the event the rising branch was stronger over the Tibetan Plateau and weaker over the southern slopes of the Himalayas compared to climatology. A stronger westerly jet was also visible on this day. One day before the cloudburst, the rising branch over Tibet and southern slopes of the Himalayas gained strength and another rising branch appeared south of the Himalayas. This strengthening and the expansion of rising branch coincided with southward shift of WJ and northward shift of EJ. On the cloudburst day, when the jets were closest to each other, the rising branches over the southern slopes of the Himalayas and south of the Himalayas were of maximum intensity. After the cloudburst day with the jets retreating to their climatological positions, the rising branch shrank. It is noteworthy that the rising branch south of the Himalayas moved southward with the EJ retreating southward.

In addition, the strengthening pattern of the rising branch over the slopes of the Himalayas clearly coincided with the southward migration of the upper-level westerly trough (Figure 4.2a) and formation of low pressure over the Nepal Himalayas (Figure 4.3a, Figure 4.3b and Figure 4.3c). The strongest vertical velocity on the cloudburst day (0day, Figure 4.5b) also coincided with the southern-most extension of upper-level

positive PV anomaly and deeper tropopause fold (Figure 4.5a). As discussed in section 4.2.1 through 4.3, the evolution of upper-level disturbances, the surface disturbance and vertical velocity before, during and after the cloudburst suggested the association of these synoptic features during the cloudbursts in the Nepal Himalayas

#### **4.2.5 Significance of Synoptic Features**

Figure 4.6a through Figure 4.6f present the 15-day timeseries of five synoptic features and associated vertical motion of composite cloudburst events. These synoptic features are 200 hPa upper-level westerly trough, negative MSLP anomaly over Nepal, southward shift of westerly jet (200 hPa positive wind speed anomaly), northward shift of easterly jet (125 hPa positive wind speed anomaly) and upper-level positive PV anomaly on the cloudburst day and a day before. The locations and variables used to define these synoptic features and vertical motion are summarized in Table 2. The composite timeseries shows that the magnitudes of the anomalies of these 6 variables are larger than  $\pm 0.5$  standard deviations on the cloudburst day (0 day) and a day before the cloudburst (-1 day), except for the PV anomaly. The positive PV anomaly is larger than + 0.5 standard deviation only on the cloudburst day. Before and after the cloudburst day, the anomalies of these variables are within  $\pm 0.5$  standard deviation.

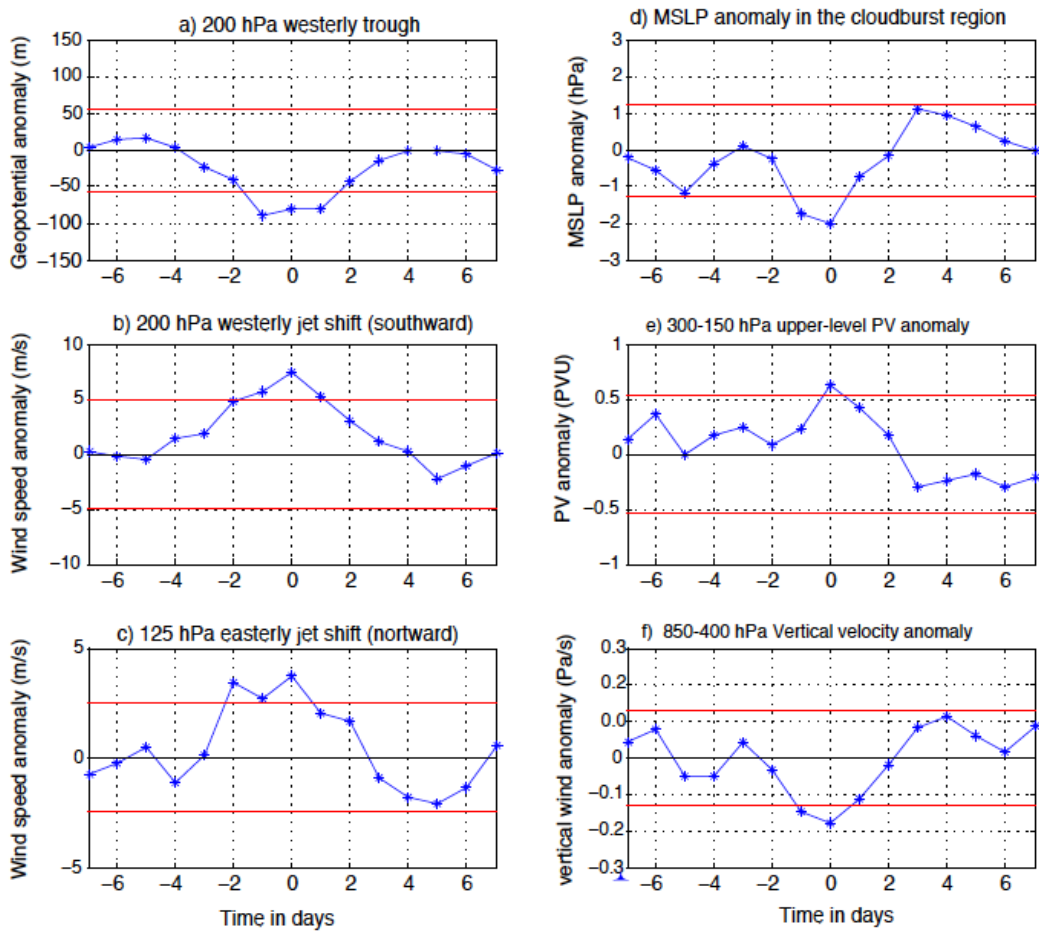


Figure 4.6: Composite timeseries of synoptic features from 7 days before to 7 days after the cloudburst event. Averaging regions are given in Table 2. 0 day is the cloudburst day. a) Westerly trough, 200 hPa negative geopotential anomaly; b) WJ shift, 200 hPa positive wind speed anomaly; c) EJ shift, 125 hPa wind speed anomaly; d) Monsoon trough shift, MSLP anomaly over Nepal; e) upper-level PV anomaly, 300 hPa PV anomaly; f) Rising motion, 850-400 hPa vertical velocity anomaly (Pa/s). Red lines from (a) through (f) represent  $\pm 0.5$  standard deviation.

Table 2: Description of six synoptic features of cloudburst composite, timeseries of which are shown in Figure 4.8

<b>Synoptic Features</b>	<b>Variables Used</b>	<b>Region</b>
Westerly trough	200 hPa negative geopotential anomaly northwest of the Himalayas	80.1-90E, 35.4-40.3N
Westerly jet shift (southward)	200 hPa positive wind speed anomaly north of Himalayas	85-90E, 30.535.4N
Easterly jet shift (northward)	125 hPa positive wind speed anomaly south of the Himalayas	85-86.4E, 17.8-22.1
Monsoon trough shift (northward)	negative MSLP anomaly over Nepal	83.6-85E, 27-29.8N
Upper-level positive PV anomaly	mean 300-150 hPa positive PV anomaly north of the Himalayas	85-85.7E, 36.8-40.3N
Rising motion	mean 850-400hPa negative vertical velocity anomaly over Nepal	85-85.7E, 27.7-28.4N

The fact that the anomalies of the variables are within  $\pm 1$  standard deviation could be because these anomalies are composite timeseries. Therefore, we analyzed standard deviations of these anomalies for 10 individual cloudburst events. For each individual case, we picked locations where the ratio of anomaly to standard deviation was largest on the cloudburst day and these regions are tabulated in Table 3. As an example, timeseries of the five synoptic features and associated vertical motion for 1993 event are shown in Figure 4.7a through Figure 4.7f. We did same analysis for remaining 9 events and the standard deviation results for the 10 individual events are summarized in Table 4. Anomalies of the synoptic features for all the events, except for July 17 2003, are larger than  $\pm 1$  standard deviation. Anomalies of these features during some cloudburst events are even larger than  $\pm 2$  standard deviation. These results further demonstrate the significance of five synoptic features and vertical velocity observed during the cloudbursts.

Table 3: Description of six synoptic features of individual cloudburst events along with regions averaged, timeseries of which are shown in Figure 10 for the 1993 event

Synoptic Features	Westerly trough	Westerly jet shift (southward)	Easterly jet shift (northward)	Monsoon trough shift (northward)	Upper-level positive PV anomaly	Rising motion
Variables Used	200 hPa negative geopotential anomaly northwest of the Himalayas	200 hPa positive wind speed anomaly north of the Himalayas	125 hPa positive wind speed anomaly south of the Himalayas	negative MSLP anomaly over Nepal	300 hPa positive PV anomaly north of the Himalayas	600 hPa negative vertical velocity anomaly over Nepal
<b>1986</b>	74.5-76.6E, 36.1-38.2N	84.3-85E, 33.3-34N	82.2-87.1E, 14.3-15N	84.3-85E, 34-34.5N	80.1-82.2E, 27.7-28.4N	87.8-88.5E, 28.4N
<b>1987</b>	60.4-61.2E, 30.5-31.2N	77.3-78E, 30.5-31.2N	82.2-87.1E, 17.1-18.5N	81.5-82.2E, 29.1N	86.4-87.8E, 27-28.4N	84.3-85.7E, 28.4N
<b>1990</b>	84.3-86.4 E, 44.6-42.6N	84.3-85E, 36.1-37.5	80.1-82.2E, 16.4-17.1N	84.3-85.7E, 30.5-31.2N	85-86.4, 32.6-33.3N	84.3-85, 28.4-29.8N
<b>1993</b>	86.5-87.1E, 36.1-38.2N	83.6-86.4E, 29.1-30.5N	82.2-86.4E, 16.4-17.1N	85.7-86.4E, 27.7-28.4N	83.6-84.3, 34-35.4	87.8-88.8, 27-29.8N
<b>1996</b>	75.2-80.2E, 38.2-39.6N	82.2-84.3E, 34-35.4N	83.6-85E, 17.1-18.5	83.6-84.3E, 33.3-34N	87.1-88.5E, 28.4-29.1N	85.7-86.4E, 27.728.4N
<b>2001</b>	62.5-63.8E, 48-49.4N	86.4-87.1E, 33.3-34.7N	84.3-86.4E, 19.2-20.7N	82.9-83.6E, 28.4-29.1N	84.3-85E, 34.7-35.4	86.4-87.1E, 27-29.1N
<b>2002</b>	66-68.2E, 34.7-35.5N	74.5-75.2E, 30.5-31.2N	84.3-86.4E, 16.4-17.1N	83.6-85E, 28.4-29.1N	88.5-89.2E, 31.9-32.6N	84.3-85E, 27-28.4N
<b>2003_1*</b>	85-86.4E, 42.4-43.8N	79.4-80.1E, 28.4-29.1	85-87.1E, 25.6-26.3N	82.-83E, 30.5-31.2N	89.2-90E, 26.3-27.7N	84.3-85E, 26.3-27N
<b>2003_2*</b>	83.6-83.4E, 41.7-42.4N	83.6-84.3E, 35.4-36.1	78-80.1E, 22.1-23.5N	82.2-84.3E, 29.8-30.5N	84.3-85E, 27.7-28.4n	84.3-85E, 27.7-28.4N
<b>2007</b>	74.5-76.6E, 40.3-41.7N	79.4-83.4E, 30.5-31.2N	85-87.1E, 18.5-19.2N	84.3-86.4E, 28.4-29.1N	84.3-85E, 34-35.4N	84.3-85E, 26.3-27N

\* 2003\_1 is July 18, 2003 event and 2003\_2 is July 31, 2003 event

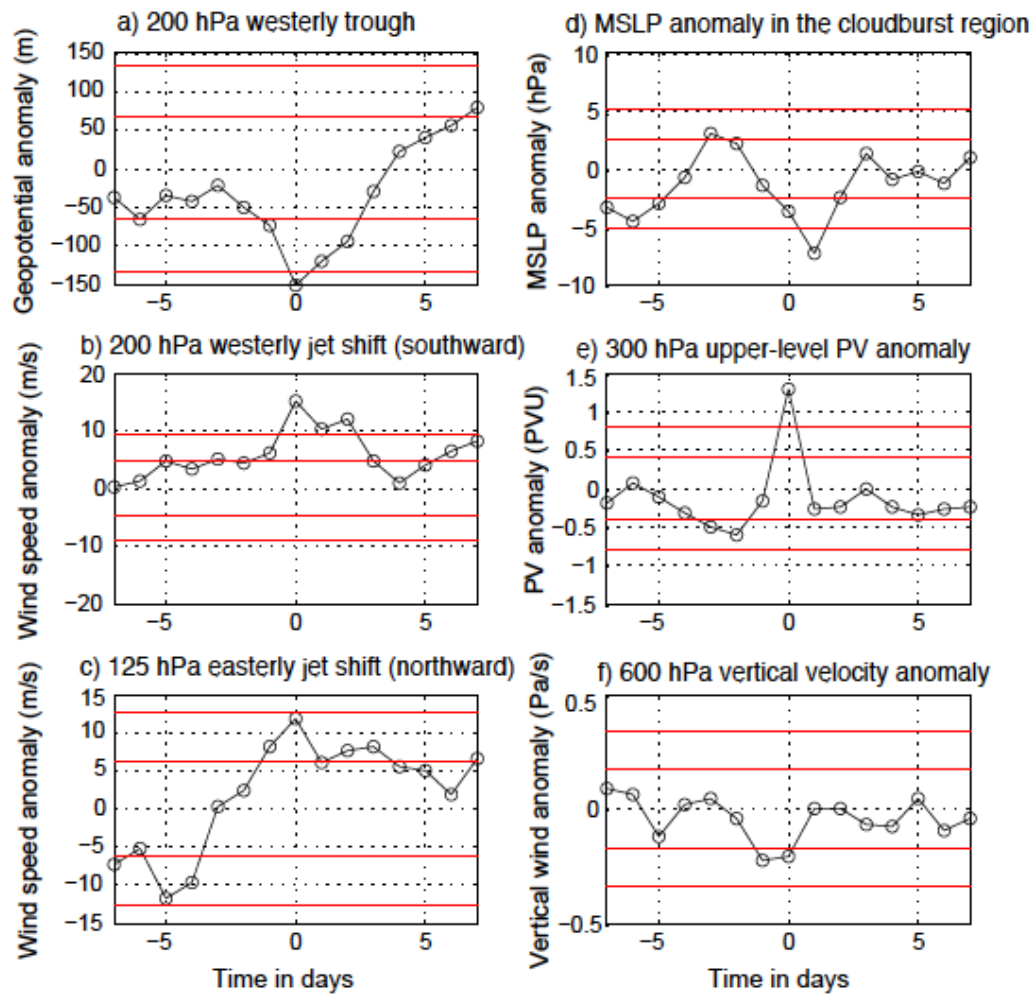


Figure 4.7: Timeseries of synoptic features for July 19-20 1993 cloudburst from 7 days before to 7 days after the cloudburst event: a) Westerly trough, 200 hPa negative geopotential anomaly; b) WJ shift, 200 hPa positive wind speed anomaly; c) EJ shift, 125 hPa positive wind speed anomaly; d) Monsoon trough shift, negative MSLP anomaly over Nepal; e) upper-level PV anomaly, 300 hPa PV anomaly; f) Rising motion, 600 hPa negative vertical velocity anomaly. Red lines from (a) through (f) represent  $\pm 1$  and  $\pm 2$  standard deviations. The list of the regions each of the variables is averaged over is in Table 3

Table 4: Status of anomalies of cloudbursts synoptic features compared to daily climatological standard deviations for the individual events.

Synoptic Features	Variables Used	Greater than or equal to $\pm 2\sigma$	Greater than or equal to $\pm 1\sigma$ but less than $\pm 2\sigma$	Less than or equal to $\pm 1\sigma$
Westerly trough	200 hPa negative geopotential anomaly northwest of the Himalayas	1986, 1987, 1993, 2001	1990, 1996, 2002, 2003_2*, 2007	2003_1*
Westerly jet shift (southward)	200 hPa positive wind speed anomaly north of the Himalayas	1986, 1987, 1990, 1993, 2002, 2003_2	1990, 2001, 2007	2003_1
Easterly jet shift (northward)	125 hPa positive wind speed anomaly south of the Himalayas		1986, 1987, 1990, 1993, 1996, 2001, 2002, 2003_2, 2007	2003_1
Monsoon trough shift	negative MSLP anomaly over Nepal	1987, 2002, 2003_2	1986, 1990, 1993, 1996, 2001, 2007	2003_1
Upper-level positive PV anomaly	300 hPa positive PV anomaly north of the Himalayas	1993, 1996, 2001	1987, 1990, 2002, 2003_2, 2007	1986, 2003_1
Rising motion	negative vertical velocity anomaly over Nepal	1986, 1987, 1990, 1996, 2002, 2003_2	1996, 2001, 2007	2003_1

\* 2003\_1 is July 18, 2003 event and 2003\_2 is July 31, 2003 event

The synoptic scale conditions found associated with cloudbursts do not appear to be as rare as cloudbursts. This suggests there are factors in addition to those captured by the composited analysis that are contributing to cloudbursts. Nonetheless, our composite analysis is a first step in determining what type of synoptic conditions are conducive to cloudbursts and the extent to which these synoptic scale conditions are unusual. This has not previously been done in the literature.

#### 4.3 Conceptual Model of Cloudburst Mechanism: Tropical-Extratropical

Upon consideration of the composite analysis we found the combination of the following five upper-level and surface synoptic signatures during cloudburst events in central Nepal Himalayas: 1) an upper-level westerly trough intrusion towards the Nepal Himalayas, 2) entrance regions of westerly and easterly jet entrance regions come closer towards Nepal Himalayas, 3) an upper-level PV anomaly associated with a steep tropopause fold over

the Himalayas north of the cloudburst region and 4) the monsoon trough shifts northward towards the Himalayas. Along with these features, we also found larger than normal rising motion.

The interaction of these synoptic features is shown in the conceptual diagram (Figure 4.8). In this model we propose that the upper-level trough helped the development of the surface low pressure over the foothills of the Nepal Himalayas (Figure 4.8a). This might be the reason for the shift of monsoon trough towards the Nepal Himalayas during the cloudbursts. The surface low over the Himalayas promotes the direct convergence of moist flow from the Arabian Sea over the mountains and orographic uplift. In the meantime, the co-location of upper-level jets entrances, with the rising motion around each jet entrance coming nearer to the Nepal Himalayas might be another favorable factor for the large-scale rising motion over the cloudburst region (Figure 4.8b).

The upper-level PV anomaly associated with the steep tropopause fold may have a critical role in further intensifying the surface low and promoting moist southerly flow to traverse over the southern slope of the Himalayas locally during the cloudbursts (Figure 4.8c). Therefore, the favorable condition for deepening the surface low and enhancing rising motion during the cloudbursts in the Nepal Himalayas may be due to the combination of these five upper-level synoptic features interacting with the elevated topography. We would like to point out that despite the fact that the upper-level features (westerly jet entrance and PV anomaly associated with tropopause fold) are situated further north of the Nepal Himalayas, the interaction between these upper-level features in the north with the surface flow in the southern slopes of the Nepal Himalayas is possible. It is because the topography creates the wall effect leading to extreme rainfall

events due to the orographic uplift in this region. We speculate that in the absence of the topography, the influence of the upper-level disturbance might occur further north of the current location in the Nepal Himalayas. In contrast to conceptual models of the cloudbursts by the Das et al. (2006) and by Rasmussen and Houze (2012), the cloudburst in the Nepal Himalayas do not seem to be associated with the propagation of convective systems by upper-level wind but rather associated with the combined effect of deep upper-level trough, upper-level PV anomaly superimposed with the elevated topography and closer proximity of westerly and easterly jet entrance regions over the Nepal Himalayas

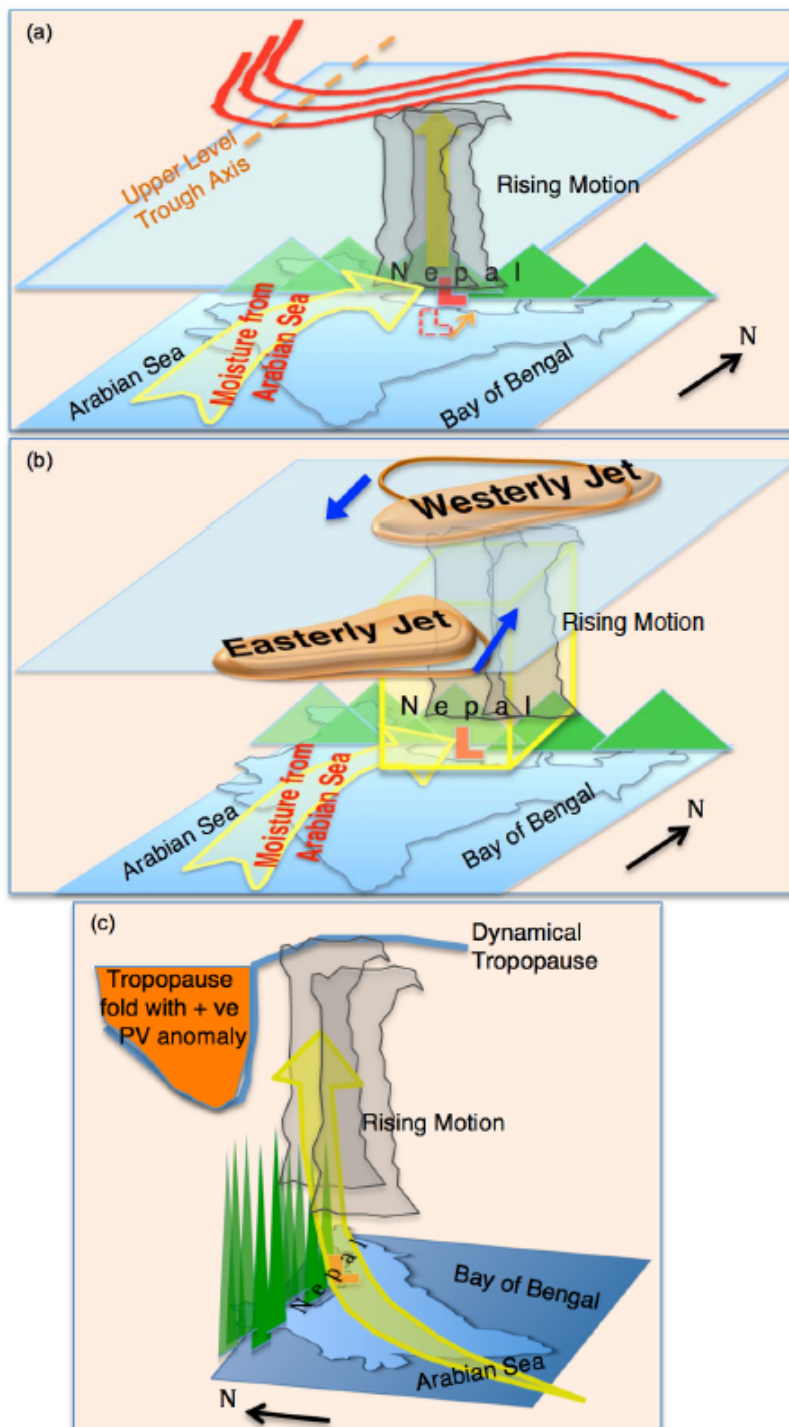


Figure 4.8: Conceptual diagram of interaction of synoptic features during cloudburst. a) Role of Upper-level trough in monsoon trough shift and moisture convergence towards the Nepal Himalayas; b) Role of Easterly and Westerly Jet shifts for enhanced vertical motion over the Nepal Himalayas; c) Upper-level PV anomaly associated with tropopause fold intensifying surface low and moisture convergence over the Nepal Himalayas.

In addition to the QG explanation, there is another potential explanation for the association of upper-level synoptic features with intense convection. A number of studies have shown relationship between the upper-level inertial instability with the meso-scale convective systems (Emanuel 1980, 1982; Mecikalski and Tripoli 2003; Rappin et al. 2011; Blanchard et al. 1998). For example, Blanchard et al. (1998) discusses the role of weak or unstable inertial stability in enhancing deep convective circulations equatorward of the WJ wind maxima where anticyclonic shear is large. Rappin et al. (2011) provide a similar argument about the role of the weak inertial stability in the equatorward side of the WJ on the intensification of the tropical storms or convective storms, by providing lower resistance to the outflow from these convective storms. From angular momentum conservation theory, an increase in angular momentum with latitude poses a horizontal constraint to the flow moving northward. This positive angular momentum in the northward direction represents strong inertial stability (Randall 2015, pp 177:178). The anticyclonic shear weakens the inertial stability by counteracting the planetary vorticity (Randall 2015, pp 178). The presence of strong westerly jet shows the strong anticyclonic shear in the equatorward side of the westerly jet and weak inertial stability. This makes it easier for outflow from convection to move northward, enhancing the storm. An appearance of a stronger and southwesterly jet (than climatology) over the Nepal Himalayas might have played similar role in providing weak inertial stability and supporting intensive cloudburst events.

The westerly jet with a slight southwesterly component can be seen east of the trough in Figure 4.2b (0 day). Near the surface, during cloudbursts, there is anomalous flow from the Arabian Sea (Figure 4.3c). The overall flow into Nepal comes from the Arabian Sea and is almost perpendicular to the orography (Figure 4.3b, Figure 4.4b), contrasting with

what is seen during climatological conditions (Figure 4.1d). These synoptic features are conceptualized in Figure 4.8b. Together the upper-level jet and anomalous low-level flow resemble the conditions for events known as PREs (Predecessor Rain Events) (Galarneau et al. 2010; Bosart et al. 2012) which are heavy rainfall events occurring ahead of tropical cyclones in the US. There is a particular resemblance to the southwesterly jet (SJ) category described by Moore et al. (2013), which occur due to the poleward advection of a deep moist layer established by the tropical cyclones in the Gulf of Mexico/Atlantic Ocean off the coast of Florida, and in the presence of a surface lifting mechanism, such as fronts, convergence or orographic regions. The SJ type PREs occur near an equatorward jet entrance region (Moore et al. 2013). Over the Nepal Himalayas, during cloudbursts, orographic lifting and the equatorward entrance region of the westerly jet may provide a favorable synoptic mechanism during the cloudbursts that is similar to what occurs during the SJ type PREs, with the Himalayas providing an orographic forcing barrier and the monsoonal flow from the Arabian sea representing the role of tropical cyclones in advecting low level moisture. This similarity suggests the tropical-extratropical interaction associated to upper-level inertial instability during the cloudburst events.

Previous studies have also shown a tropical-extratropical interaction due to the intrusion of mid-latitude troughs into the tropics (e.g. Kiladis and Weickmann 1992a; Ding and Wang 2007; Knippertz 2007, Hong et al. 2011). These studies showed that the intrusion of eastward moving upper-level troughs originated in the extratropics can trigger convection in the tropics, supporting our results. While it appears, from the above discussion, that the combined forcing from two jets and upper-level disturbances might have produced the enhanced rising motion, triggering favorable condition for the

cloudbursts, it is also possible that the strong convection during the cloudburst might have caused the WJ to shift southward. Causality cannot be definitively established in a composite study.

While this chapter identifies the favorable synoptic conditions that suggests tropical-extratropical interaction during the cloudbursts, a question what triggers this favorable condition still remains. The influences of tropical heating on the mid-latitude weather have been discussed in the number of studies (e.g., Sardeshmukh and Hoskins 1988; Kiladis and Weickmann 1992b). They showed that tropical convection generates a Rossby wave train poleward of the convective heating source. This might cause the WJ to shift southward. Examination of if tropical heating could be a precursor that triggers Rossby waves which may even make favorable conditions for the cloudbursts is one the objectives of this study and is discussed in Chapter 5.

## Chapter 5

### **Tropical-Extratropical Interaction Mechanism during Cloudburst**

This chapter focuses on two major hypothesis of this study. First, it examines the Hypothesis 2 that the tropical-extratropical interaction is stronger during the cloudbursts. Second, it tests the Hypothesis 3 that the role of tropical heating as a triggering factor that leads to a process that contributes to the extratropical-tropical interaction during the cloudburst mechanism in the Himalayas.

#### **5.1 Northward Tropical-Extratropical Interaction**

##### **5.1.1 Local Hadley Cell Strength**

Figure 5.1a compares the mean meridional circulation of the cloudburst day (right panel) with the climatology (left panel) averaged for 5 longitudinal zones from east to west [zone-1 (90E-100E), zone-2 (80E-90E), zone-3 (70E-80E), zone-4 (60E-70E) and zone-5 (20E-60E)]. Nepal Himalayas is located in zone-2. In the eastern two zones (zone-1 and zone-2) the northern meridional cells are stronger during the cloudburst events than climatology. In both eastern zones the extent of the northern cells is larger than climatology. In these two eastern zones, the southern cell breaks into two cells during cloudburst events: a local cell and cross-equatorial cell. This local cell has rising branch over the southern slopes of the Himalayas and descending branch spread between 10N and 20N. Climatologically, the southern cell is single and is inter-hemispheric with wide rising branch spreading between equator and 30N and descending branch in the southern hemisphere in these longitudes (Figure 5.1a left panel, zone-1 and zone-2). Nevertheless, both southern cells during cloudbursts are stronger than the climatology. In zone-3, the northern cell seems to be similar in magnitude in the upper-level but its width shrank to 40N during cloudburst in contrast to 45N for the climatology. This shrink seems to be due

the southward extension of extratropical indirect cell. In zone-4, the extratropical cell is stronger than climatology. In zone-5, the northern mean meridional cell is weaker than climatology. This is in contrary to the stronger northern cells in previous 4 zones between 60E-100E. The upper-level meridional wind also showed stronger northerly wind in the northern tropical cells in zones 1, 2 3, and 4 and weaker northerly wind in zone-5 and this is in the consistent with the strength of these cells. In other words more northward flow east of 60E and more southward flow west of 60E. *These results on the mean meridional cells suggest that between 80-100E, northern local Hadley cell is stronger during the cloudbursts than the climatology while between 20-60E, northern local Hadley cell is weaker than climatology.*

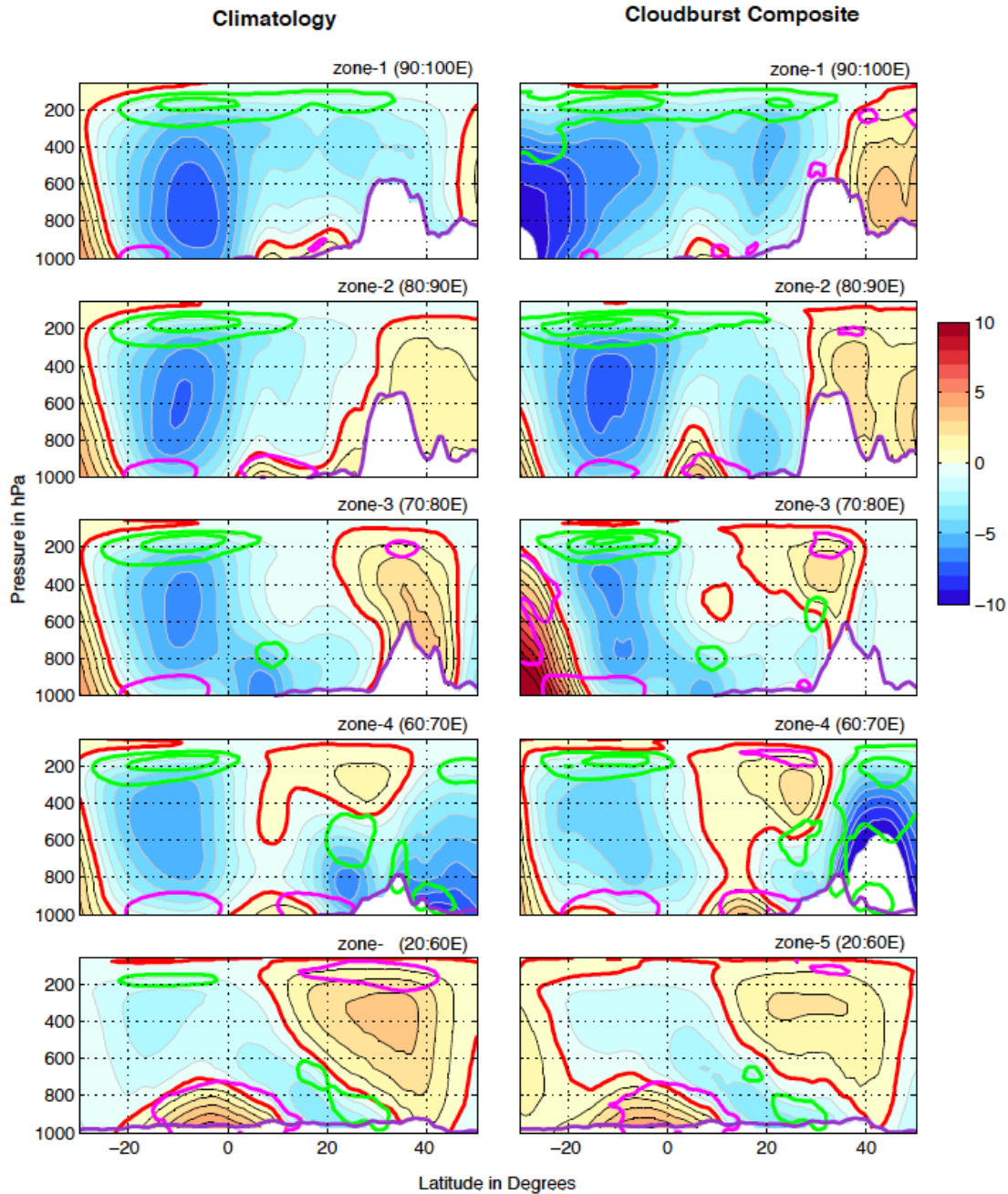


Figure 5.1a: Mean meridional streamfunction ( $10^{11}$  Kg/s) at 5 longitudinal zones. Left panel: Climatology; Right panel: Cloudburst composite. Gray contour (blue shading): anticlockwise circulation, black contour (orange shading): clockwise circulation; Red contour: streamfunction 0; Green contour: northerly wind (m/s); Magenta: southerly wind (m/s); Purple with white mask: mountains

### 5.1.2 Momentum Transport by Mean Meridional Circulation (Local Hadley Cell)

Figure 5.1b shows the comparison of the northward transport of westerly momentum by the mean meridional circulation between climatology (left panel) and cloudburst events

(right panel) at above mentioned five zones along the Himalayas. In the zone-1, the northward transport of momentum from 15S-30N is higher during the cloudburst events than the climatology. In zone-2, the mean circulation transports momentum northward from 15S to 50N and this transport is much higher than the climatology. In zone-1 and zone-2, the northward westerly momentum flux by northern Hadley cell exceeds the climatology. In zone-3, northward transport is from 30N-45N and is higher during the cloudburst than climatology. Noticeably, in zone- 4 southward transport of westerly momentum by tropical cell and by extratropical cell is higher during cloudburst events than the climatology. In zone- 5, northward transport is limited to the descending branch and from 30N-50N and is weaker than the climatology. *The northward flux of westerly momentum by mean meridional circulation is higher in the eastern three zones and southward flux of westerly momentum by mean meridional circulation is higher in the remaining two western zones during the cloudburst than the climatology.*

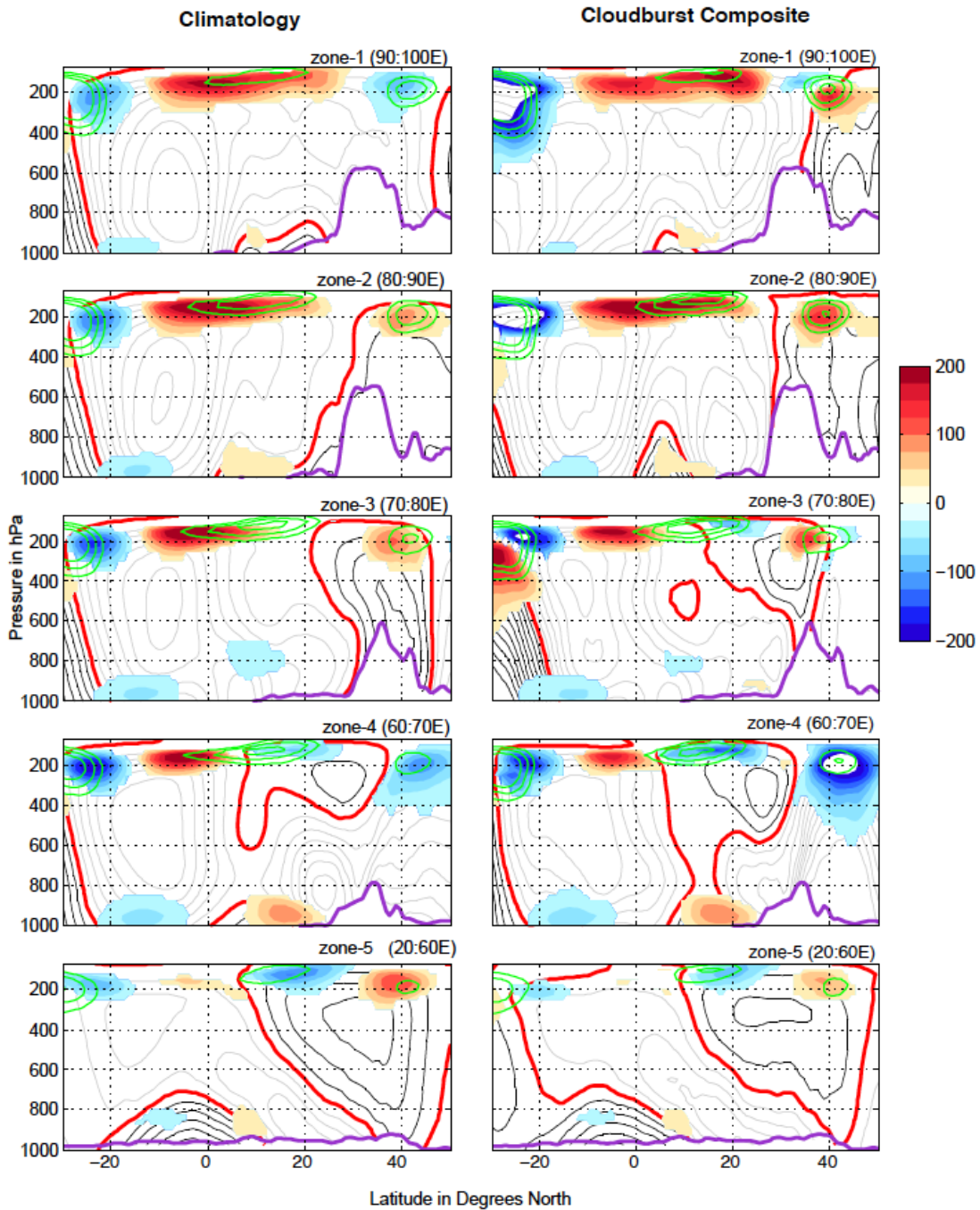


Figure 5.1b: Northward transport of westerly momentum by mean meridional circulation at 5 longitudinal zones (Shading in  $m^2 s^{-2}$ : Blue is southward  $< -50 m^2 s^{-2}$  and red is northward transport  $> 50 m^2 s^{-2}$ ). Left panel: Climatology; Right panel: Cloudburst composite. Gray contour: anticlockwise streamfunction cell ( $10^{11} Kg/s$ ), black contour: clockwise streamfunction cell ( $10^{11} Kg/s$ ), Red contour: 0 streamfunction; Green contour: Easterly and Westerly Jets (m/s). Purple with white mask: mountains

### 5.1.3 Momentum Transport by Transient Eddies

Figure 5.1c shows the northward transport of westerly momentum by transient eddies at above-mentioned five zones for climatology (left panel) and for cloudburst composite (right panel). In zone-1 and zone-3 northward transports of westerly momentum by transient eddies in the upper-level branch of northern cell are higher during the cloudburst events than during the climatology. In zone-2 the northward transport is similar in magnitude for the cloudbursts and the climatology. It is noteworthy that zone-2 is longitudes along Nepal where cloudbursts were selected and in this zone the local northern Hadley cell is strongest and northward transport of momentum is maximum compared with other zones. In zone-4 and zone-5, there are no northward transport of momentum by transient eddies. It is also noteworthy that, in the northern hemisphere, the northward transport of momentum by mean meridional cell is larger than by the transient eddies both during cloudburst events and climatology. *The northward transport of westerly momentum by transient eddies is mainly active in zone-1 (immediately east of Nepal) and zone-2 (immediately west of Nepal) during the cloudburst than the climatology.*

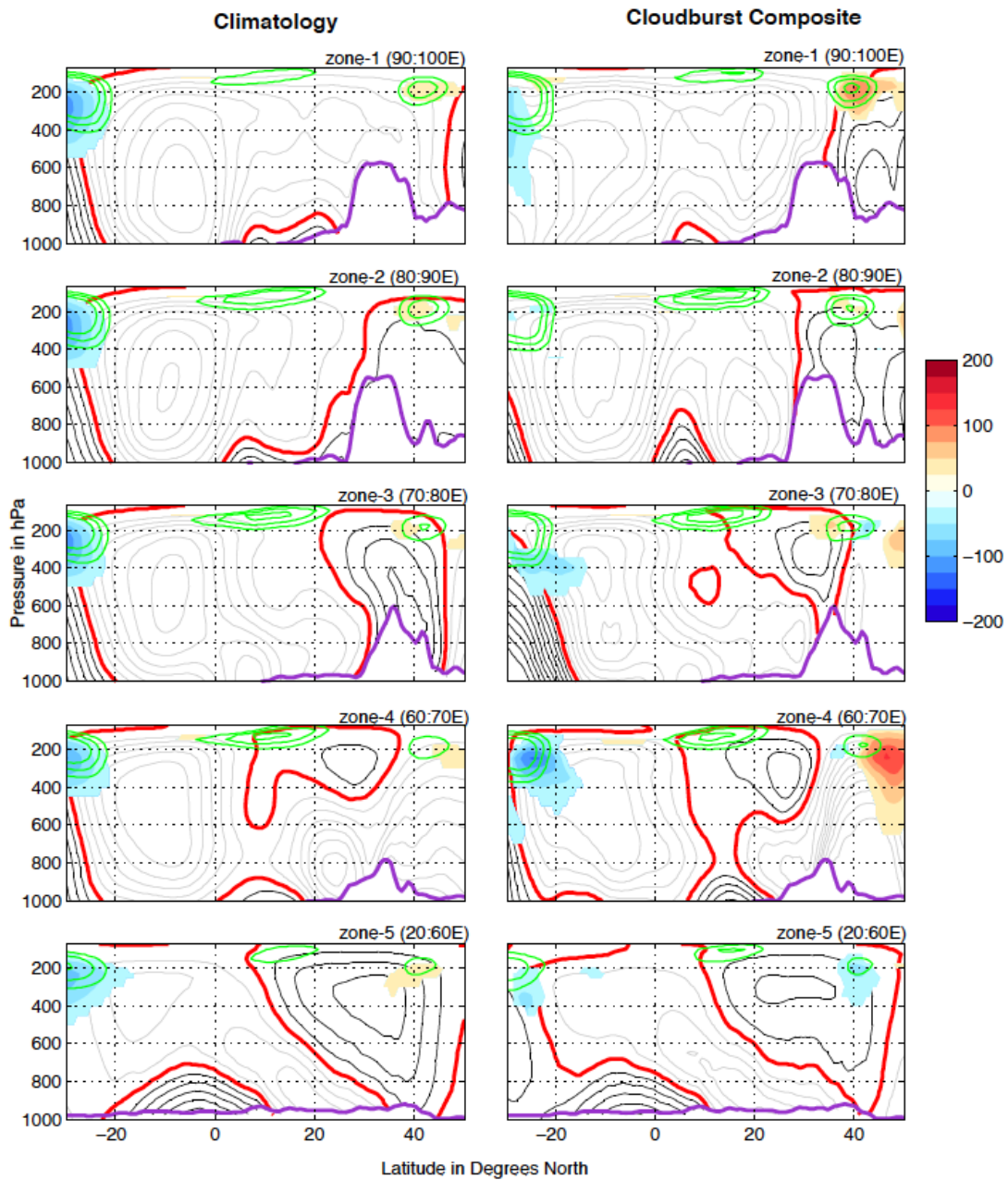


Figure 5.1c: Northward transport of westerly momentum by transient eddies at 5 longitudinal zones (Shading in  $\text{m}^2 \text{s}^{-2}$ : Blue is southward  $< -50 \text{ m}^2 \text{s}^{-2}$  and red is northward transport  $> 50 \text{ m}^2 \text{s}^{-2}$ ). Left panel: Climatology; Right panel: Cloudburst composite. Gray contour: anticlockwise streamfunction cell ( $10^{11} \text{ Kg/s}$ ), black contour: clockwise streamfunction cell ( $10^{11} \text{ Kg/s}$ ), Red contour: 0 streamfunction; Green contour: Easterly and Westerly Jets (m/s). Purple with white mask: mountains

#### **5.1.4 Momentum Transport by Stationary Eddies**

Figure 5.1d shows the northward transport of westerly momentum by the stationary eddies for climatology (left panel) and cloudburst events (right panel) in the above-mentioned 5 zones. It is noteworthy that the magnitude of momentum transport by stationary eddies is an order smaller than by the mean circulation and transient eddies. In zone-1, zone-2 and zone-3, the northward transport of moment upper branch of the northern cell is stronger during cloudbursts than during climatology. In zone-4, the magnitude is similar during cloudburst events and climatology. In zone-5 the northward transport is weaker during cloudburst events than the climatology.

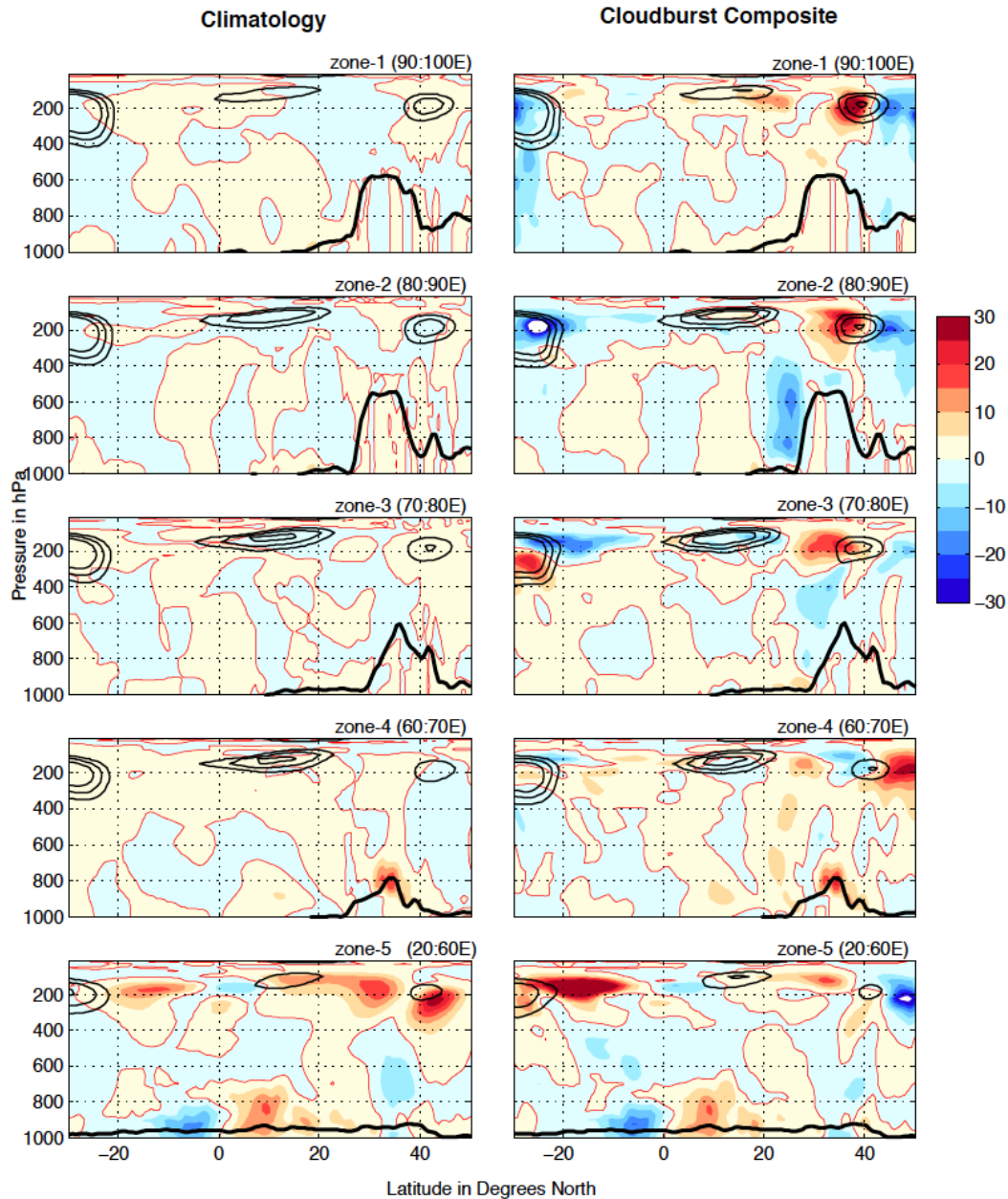


Figure 5.1d: Northward transport of westerly momentum by stationary eddies at 5 longitudinal zones (Shading in  $\text{m}^2 \text{s}^{-2}$ : Blue is southward and red is northward transport). Left panel: Climatology; Right panel: Cloudburst composite. Gray contour: anticlockwise streamfunction cell ( $10^{11} \text{ Kg/s}$ ), black contour: clockwise streamfunction cell ( $10^{11} \text{ Kg/s}$ ), Red contour: 0 streamfunction; Green contour: Easterly and Westerly Jets (m/s). Purple with white mask: mountains

### 5.1.5 Momentum Flux Divergence by Transient Eddies

Figure 5.1e depicts the horizontal flux divergence of momentum by the transient eddies for climatology (left panel) and cloudburst events (right panel) above mentioned five

zones. In zone-1, the flux divergence in rising branch of northern cells (30N-40N, south of westerly jet) is stronger during cloudbursts than during climatology. But in zone-2 (longitudes of Nepal) the flux divergence during the cloudburst is not significantly different from the climatology. In zone-3, flux divergence and convergence south of westerly jet is higher during the cloudbursts than the climatology. In zone 4 and 5 flux divergence south of westerly jet in climatology is replaced by the flux convergence during cloudbursts. It is interesting to note that flux divergence by eddies is much smaller during cloudburst events than climatology in the southern hemisphere. The flux pattern in various zones suggests that the mid-latitude eddies seem to effect east of 90E and west of 80E and has little effect in the zone between 80-90E along the Nepal Himalayas during cloudburst events. Bordoni and Schneider (2008) showed that the increase in divergence of momentum flux due to transient eddies strengthen the Hadley cell. Based on their findings and the flux divergence pattern in Figure 5.1e and the strength of Hadley cells in Figure 5.1a, it seems that eddy strengthens the Hadley cell east of 90E and weakens the Hadley cell to the west of 80E while having little effect between 80E-90E.

In summary, above results clearly showed enhanced northern Hadley cells and transport of westerly momentum by mean circulation between 80-90E (Nepal Himalayas) during the cloudbursts. While strong northern Hadley cell east of 90E seems to be the positive affect of transient eddies and weak northern Hadley cell west of 80E seems to be the negative affect of transient eddies as suggested by Bordoni and Schneider (2008).

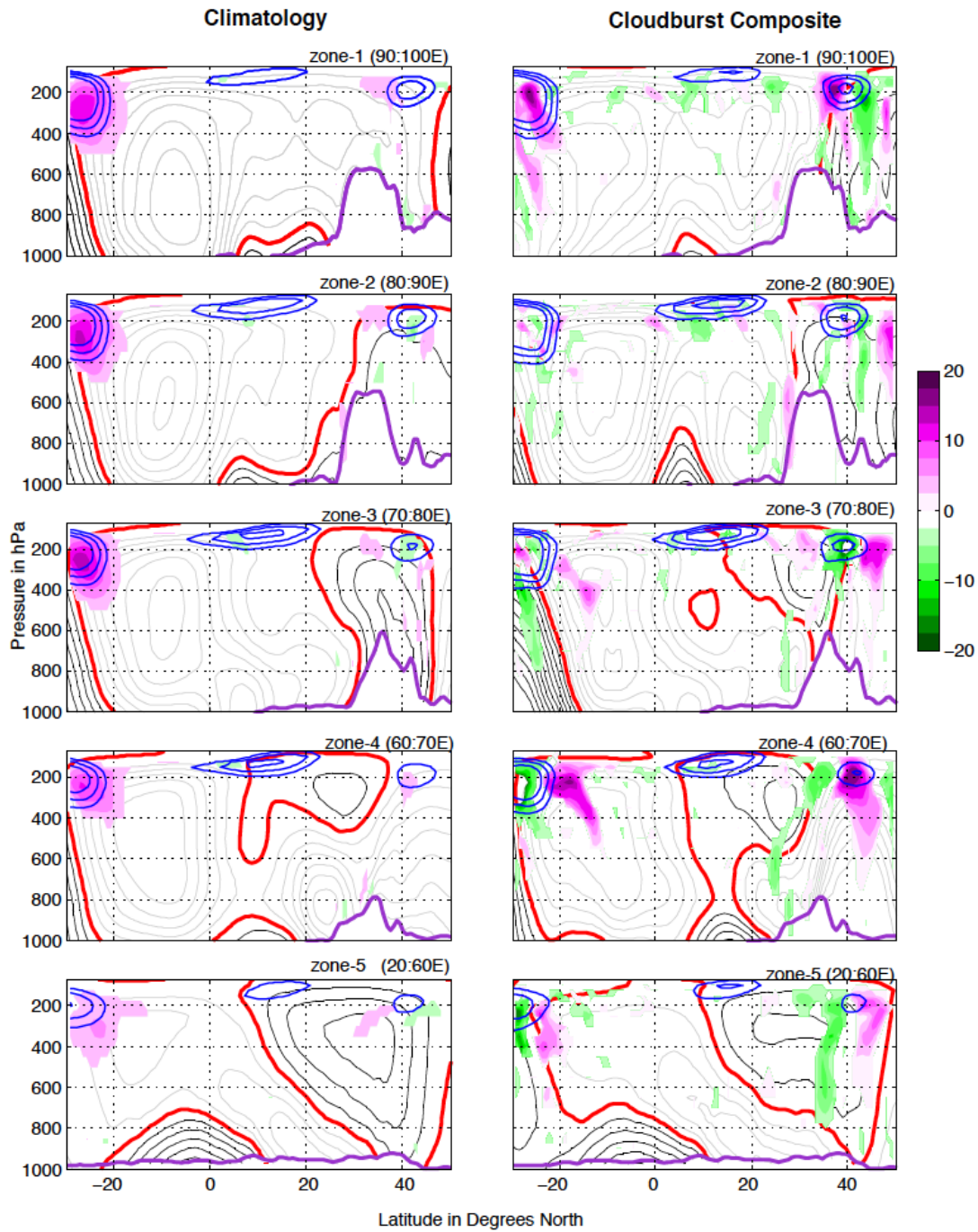


Figure 5.1e: Divergence of momentum flux divergence by transient eddies (Shading  $\text{ms}^{-2}$ : green is convergence and magenta is divergence). Left panel: climatology; Right panel: cloudburst composite. Gray contour: anticlockwise streamfunction cell ( $10^{11}$  Kg/s), black contour: clockwise streamfunction cell ( $10^{11}$  Kg/s), Red contour: 0 streamfunction; Green contour: Easterly and Westerly Jets (m/s). Purple with white mask: mountains

## 5.2 Force Balance Analysis on Tropical-Extratropical Interactions during the Cloudbursts: Pressure Gradient versus Inertial Forces

Climatologically, the northern mean meridional circulation cells during the South Asian (longitudes 50-120E) monsoon (Jul-Aug) season are weaker than the southern cells. However, the results presented in Section 5.1 showed stronger northern mean meridional cell during the cloudbursts east of 80E in the cloudburst longitudes. A stronger northern cell could either be due to the stronger poleward (northward) pressure gradient force or weaker inertial stability or due to both. This Section presents the upper-level force balance analysis in the northern cell compared that with in the southern cell during the cloudbursts. This Section compares of horizontal Montgomery streamfunction gradient (MSG) given by  $-\nabla_{\theta}\psi_M$ , and inertial force given by  $-(f + \zeta)\vec{k}x\vec{u}$  in the north and south of the Nepal Himalayas from the following horizontal momentum equation in the lamb vector form (ignoring kinetic energy gradient terms).

$$\frac{d\vec{u}}{dt} = -\nabla_{\theta}\psi_M - (f + \zeta)\vec{k}x\vec{u}$$

Figure 5.2a and 5.2b showed climatology of Montgomery streamfunction gradient (MSG) and inertial force term at 370K. Approximately around 30N, both the terms approaches to zero across all the longitudes. North of 30N, MSG is positive (which means PGF is northward) while inertial force is negative (inertial force is southward). South of 30N, MSG is negative and inertial term is positive. Inertial term ( $-4 \times 10^{-3}$ ) is stronger than MSG ( $3.5 \times 10^{-3}$ ) north of 30N while both of them is of same magnitude with different signs in the south of 30N.

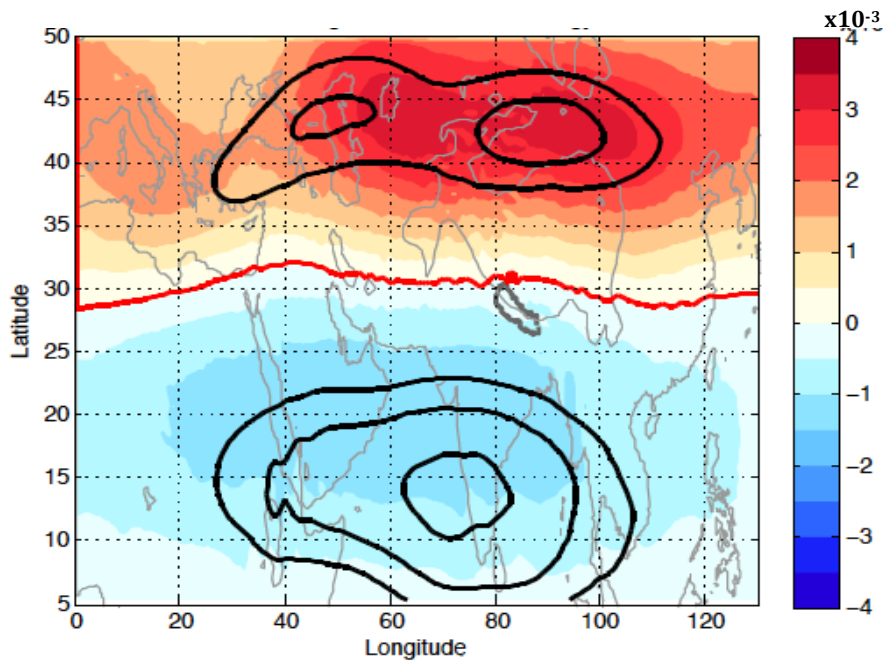


Figure 5.2a: Zonal cross section of Montgomery streamfunction gradient (MSG) at 370K for climatology (Shading). Black contours: Westerly and Easterly Jets. Red Contour: 0 MSG.

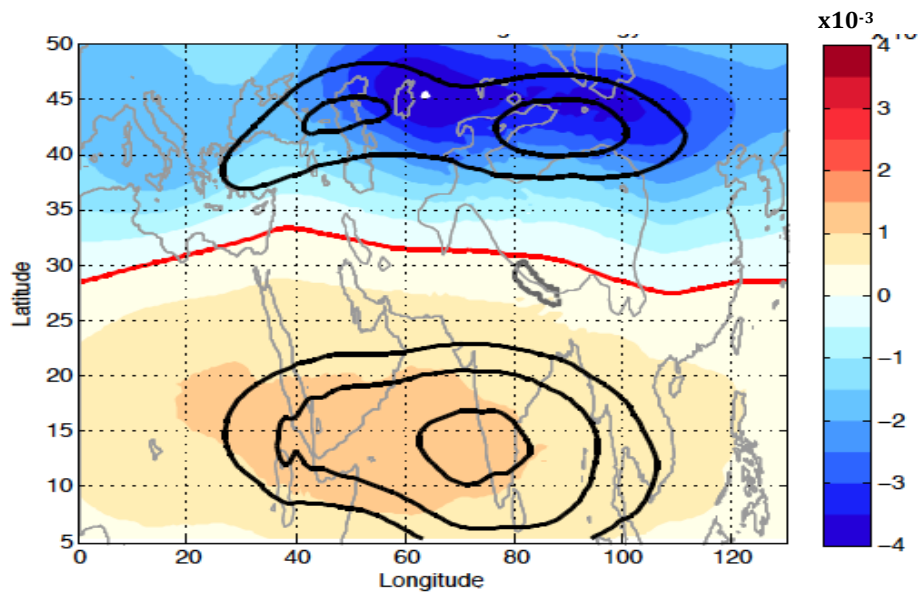


Figure 5.2b: Zonal cross section of climatological inertial terms  $[(f+\zeta)\vec{u}]$  at 370K (Shading). Black contours: Westerly and Easterly Jets. Red Contour: 0 Inertial term  $\left| \frac{-\nabla_{\theta}\psi_M}{[(f+\zeta)\vec{u}]} \right|$ .

Figure 5.2c shows the force balance ratio (FB-ratio), an absolute value of the ratio of Montgomery streamfunction gradient to inertial force term at 370K level, for the climatology. This ratio, greater than 1 suggests that acceleration due to pressure gradient

force exceeds the acceleration due to the inertial forces. For FB-ratio greater than 1, Figure 5.2a suggests that north of 30N is the acceleration is poleward and south of 30N is equatorward. Between 15N and 30N and between 30N and 40N, this parameter is greater than 1, which suggests that pressure gradient force exceeds inertial force. This suggests that the resulting meridional flow each side of 30N is due to the PGF. It is noteworthy that between 80E and 100E this parameter is slightly greater in the equatorward side of 30N than poleward side, indicating stronger southward mean meridional circulation than northward. This is consistent with the extent and strength of southern cell and northward transport of momentum in zone-1 and zone-2 (Figure 5.1a-c left panel). West of 80E, this parameter is much larger in poleward side than equatorward side of 30 N, suggesting stronger northern cell than southern cell. This is consistent with wider northern Hadley cell and northward transport of momentum (Figure 5.1a-c, left panel)

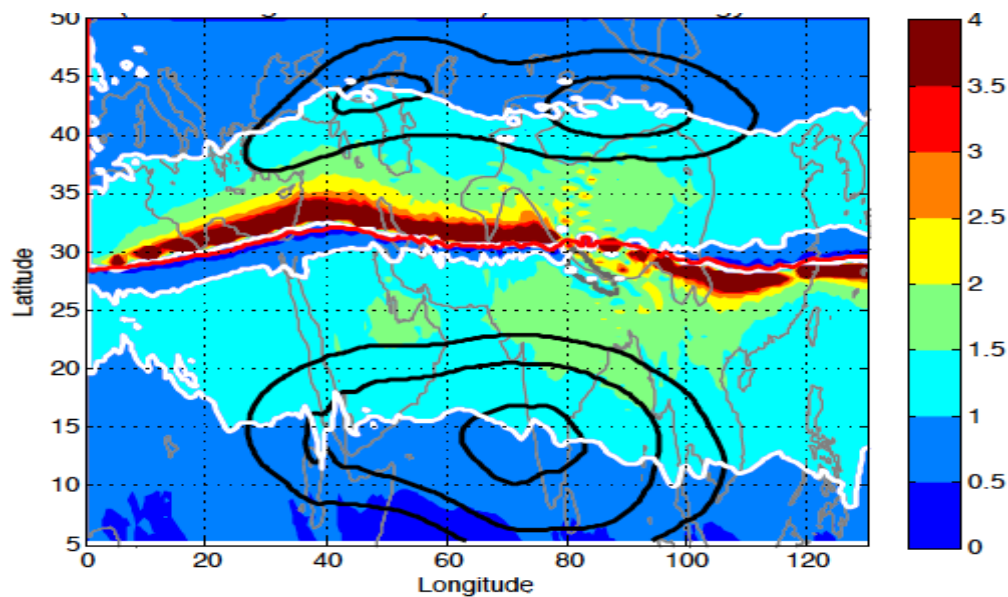


Figure 5.2c: Zonal cross section of climatology of force balance ratio (FB-ratio) at 370K (Shading). White contour: FB-ratio=1. Westerly and Easterly Jets

Figure 5.2d shows a latitudinal variation of the force balance ratio averaged for the cross-sections 80-90E and 90-100E for climatology. This parameter is slightly larger in the equatorward side than poleward side of 30N at the zone 80:90E and much higher at 90-

100E, suggesting climatologically more flow in the equatorward than poleward of 30N along this longitudes. This is consisted with the strength of the Hadley cell along the zone 80-100E.

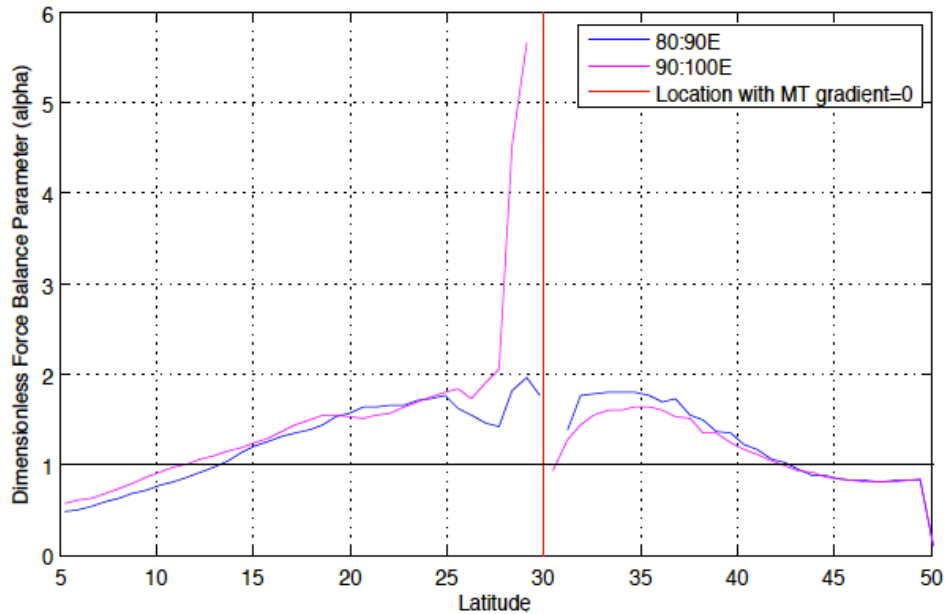


Figure 5.2d: Climatology of meridional variation force balance ratio (FB-ratio) at 370K for mean 80:90E and mean 90:100E.

Figure 5.2e shows the time evolution (at 2 day interval) of the FB-ratio at 370K for the cloudburst composite. North of 30N, on -6day, FB-ratio is much higher than 1 and uniformly spread longitudinally west of 80E, while this ratio is  $<1$  to  $\sim 1.5$  south of 30N in these longitudes. This pattern is similar to the climatology. On -4day, north of 30N FB-ratio  $>3.5$  concentrates in two regions, between 20-40E and 70-80E, near the westerly jet entrances. In these two regions this ratio is higher north of 30N than at the south. This ratio  $>1.5$  extends eastward to 100E and in this region the ratio is almost of same magnitude in both sides of 30N. From -6 day to -4day, east of 80E this ratio is greater equatorward (2.5-3) than poleward (1-2), similar to the climatology. Interestingly, on -2day, this ratio increases north of 30N significantly than at south along 80E to 90E. It is noteworthy that Nepal extends between 80E and 90E. On cloudburst day (0day) this ratio is much higher north of 30N than equatorward side, indicating higher pressure gradient

force and weaker inertial stability northward compare to equatorward between 80-100E. By +4 day the spatial pattern of the FB-ratio returns close to the normal as in climatology. This evolution of FB-ratio clearly implies that during the cloudburst pressure gradient force is higher and inertial stability is weaker poleward than equatorward of the Nepal Himalayas.

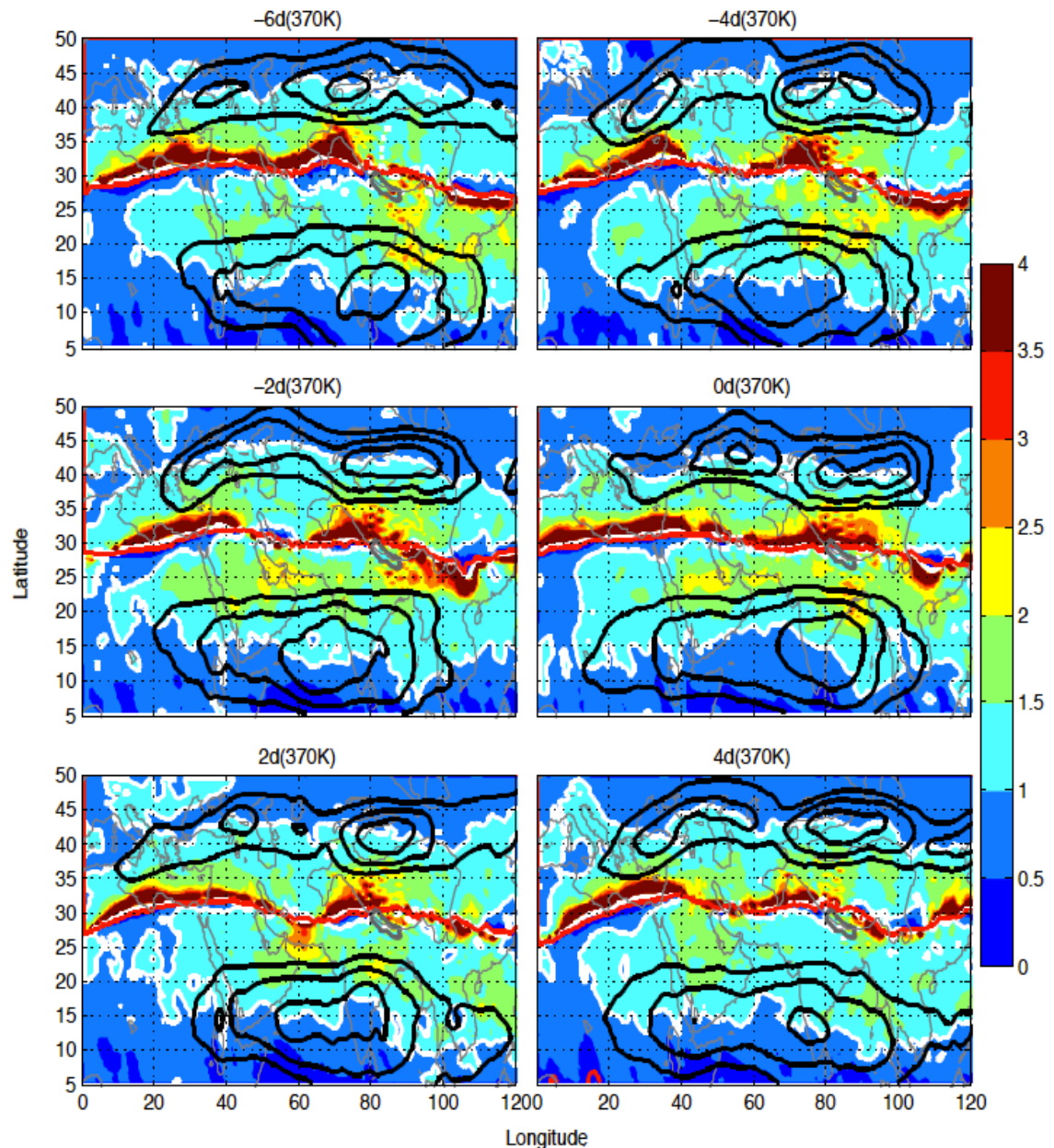


Figure 5.2e: Zonal cross section of time evolution of force balance ratio at 370K for cloudburst composites (shading) from -6day to +6day. 0day is the cloudburst day. White contour: FB-ratio=1. Westerly and Easterly Jets

Figure 5.2f shows the latitudinal variation of FB-ratio averaged over the longitudes of Nepal Himalayas for the cloudburst composite. This figure clearly shows the large force balance ratio north of 30N than to the south, indicating higher resultant flow towards north than equatorward during the cloudbursts. This parameter during the cloudburst is 4 times higher than climatological values (Figure 5.2d) north of 30N and half the climatological value south of 30N. This analysis shows that in the upper-level flow has northward tendency during cloudburst events than during the climatology due to force imbalance.

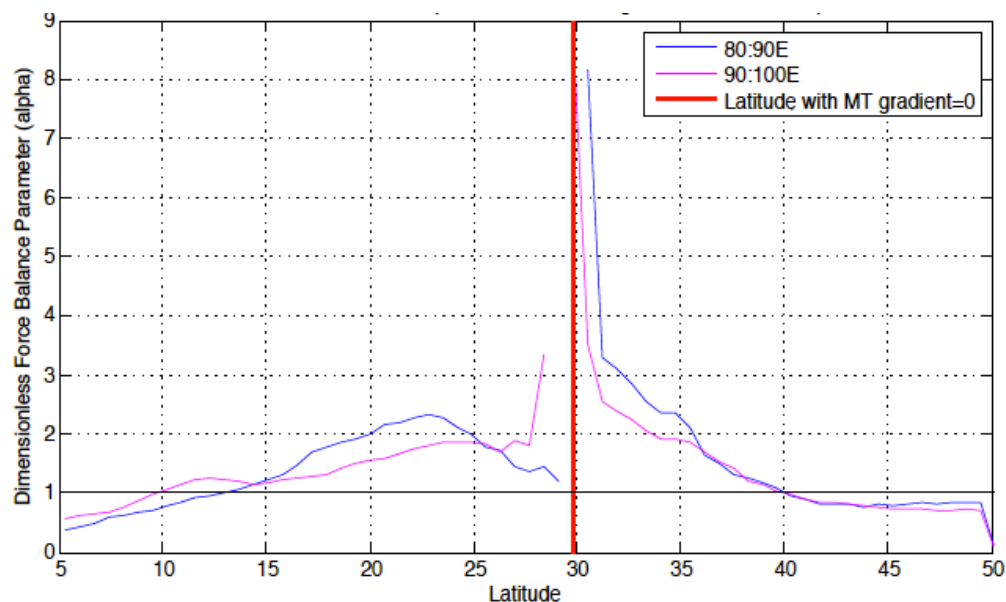


Figure 5.2f : Meridional variation force balance ratio (FB-ratio) at 370K for cloudburst composites averaged for longitudes 80:90E and mean 90:100E.

### 5.3 Upper-level Force Balance Analysis: Role of Weak Inertial Stability on Cloudburst Mechanism

This Section presents role of weak inertial force due to the non-linear terms of momentum equation. Figure 5.3a shows the climatology of force balance parameter ( $\alpha$ ) at 370K isentropic level as described in Chapter 3, section 3.5.3a. The  $\alpha$  is positive in the entire region, with close to zero values at low latitudes. This means climatologically,

upper atmosphere tends to remain inertially stable.

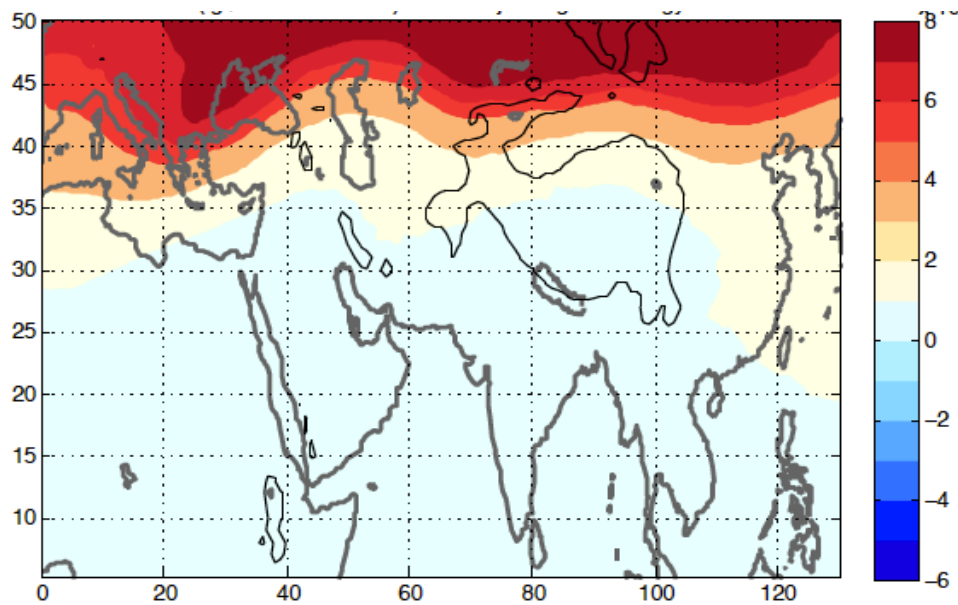


Figure 5.3a: Climatological pattern of  $\alpha = [(Q^2 - A^2 - B^2 - D^2 - 2\beta \cdot u) \times 0.5]$  in  $10^{-9} \text{s}^{-2}$  at 370K given by Eq. 5, Chapter 3. ( $\alpha$  is equivalent to inertial frequency)

Figure 5.3b shows time evolution of  $\alpha$  at 370K for cloudburst composites. The figure clearly shows increase in area and magnitude of negative value of  $\alpha$  north of the Nepal Himalayas from +6day to maximum negative value on the cloudburst day (0day) and the decreases after the event. This time evolution suggests that the non-linear terms weakens the inertial force and negative value grows as imbalance increases until the cloudburst day, leading increased northward flow on cloudburst day and then after the event the flow slowly adjusts and becomes balance. This shows the mechanism of the weakening inertial stability due to non-linear terms, leading to the force imbalance and thus tropical-extratropical interaction during the cloudburst. This type of analysis has not been done for the tropical-extratropical interaction in previous studies.

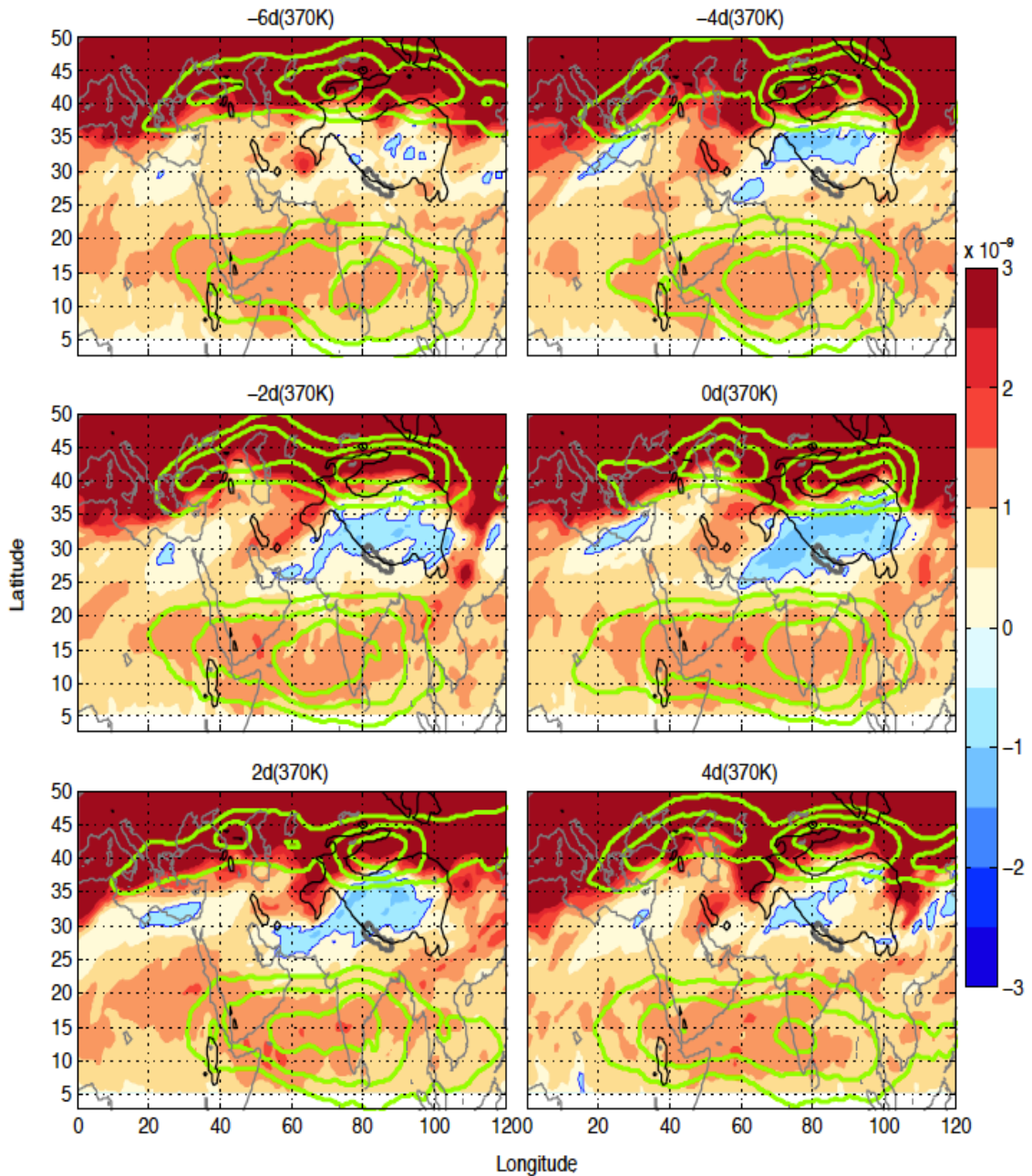


Figure 5.3b: Time evolution of  $\alpha$  ( $[(Q^2 - A^2 - B^2 - D^2 - 2\beta \cdot u) \times 0.5]$  in  $s^{-2}$  at 370K given by Eq. 5, Chapter 3.  $\alpha$  is equivalent to inertial frequency) at two-day interval from -6day to +4day for the cloudburst composite (shading). Green contours: Easterly and Westerly Jets (m/s)

#### 5.4 Role of Tropical Heating and Eddy Shedding in Triggering Favorable Condition for the Cloudbursts

Figure 5.4a shows the climatology of the locations of upper tropospheric heating (due to latent heating of monsoon rain represented by low OLR minima), lower tropospheric

low-pressure center northwest of the heating center and upper-level anticyclone (Montgomery streamfunction high) aloft surface low-pressure system. This set-up is identical to the dynamic response of off-equator tropical heating (Gill, 1980). The figure also depicts the upper-level low potential vorticity (PV) coincided with the upper-level anticyclone and elevated tropical tropopause. Figure 5.4b depicts the location of vertical motion at 500hpa and wind pattern at 370K isentropic level. It is interesting to note that strong upward motion center over the Bay of Bengal coincided with the low OLR, a heating center. The rising motion also coincided with right side of the EJ entrance region. Another rising motion center is over the southern slopes of the Himalayas (central and eastern parts), which seems be the effect of the topography. The subsidence at 500hPa coincided with the exit region of EJ and the first WJ core. It is interesting to note that East of 80E the flow in the upper-level is northerly equatorward from the 45N. Between 70-80E flow is slightly southerly north of 10N and between 60-70E flow is slightly northerly north of 25N, while west of 80E flow is southerly.

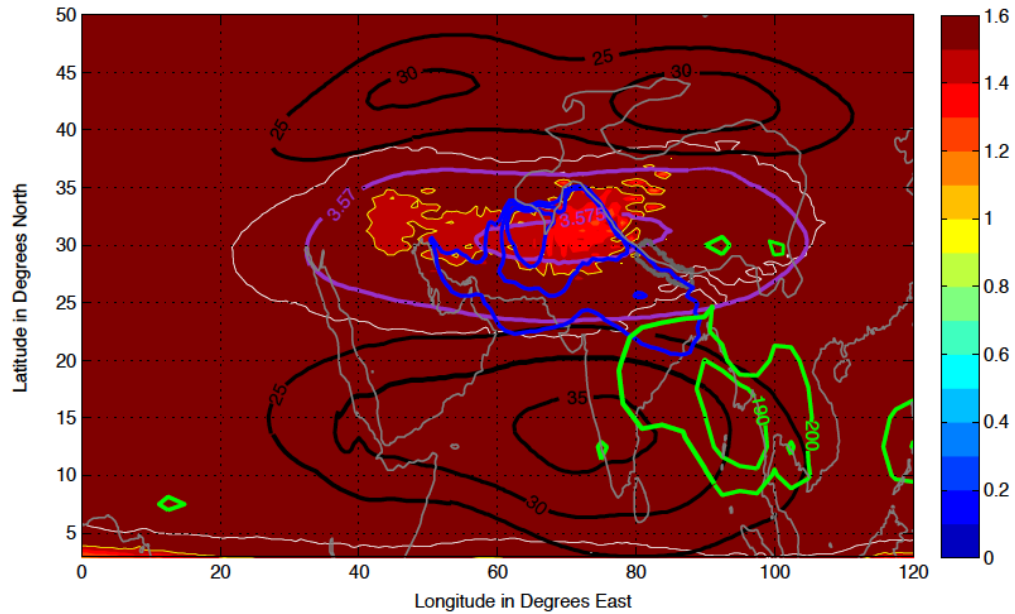


Figure 5.4a: Dynamic response of tropical heating (Jul-Aug) climatology. Green contours: OLR minima ( $190\text{-}200\text{ w/m}^2$ ) representing tropical heating; Purple contours: Montgomery Streamfunction high at 370K; Blue contours: monsoon trough (low pressure) at 850 hPa; Black contours: Easterly and Westerly Jets; Shading: PVU in PVU; Yellow contour: 1.5 PVU; White contour: 2 PVU.

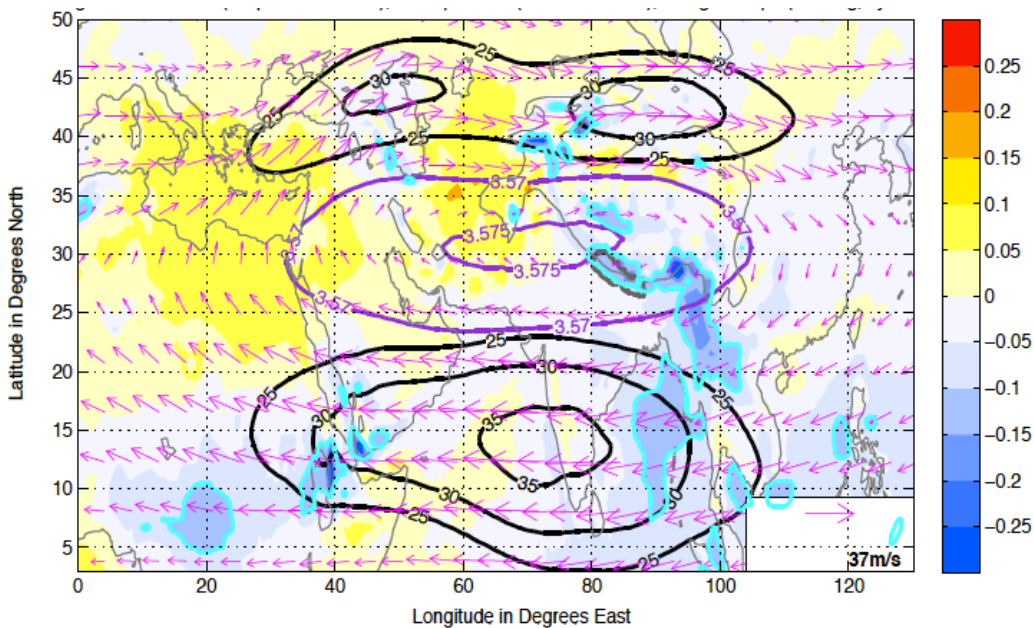


Figure 5.4b: Jul-Aug Climatology of 500 hPa vertical velocity (Shading), 370K wind vectors and Montgomery Stream function high (Purple contours). Cyan contour maximum rising motion centers

Figure 5.4c-d shows the time evolution of dynamic response of tropical heating and westward eddy shedding process from -7day before the cloudburst to +5day after the event. Because this figure is a composite of the ten cloudburst events, the eddy shedding mechanism in this figure is not as observable as in the individual case. In this figure the eddy shedding process is represented by the westward expansion of high Montgomery streamfunction center and westward movement of low PV eddies between 20N and 30N. On -7day negative OLR anomaly ( $-10$  to  $-20\text{w/m}^2$ ) is centered at 20N near the east coast of China (110E) and 850 hPa low-pressure center and upper-level high center is located northwest of this heating center (negative OLR anomaly). This dynamical setup is similar to the climatology (Figure 5.4a), except the OLR minima extended slightly eastward. On -6 day, negative OLR anomaly is lowest ( $-30\text{w/m}^2$ ) and is centered at 25N and remained at this latitude till -2 day before the event. This shows that the OLR minima center extended northward compared with the climatological location (Figure 5.4a). Significance tests reveal this center has minimal significance against climatology, and so we cannot conclude that this event is a necessary condition for all cloudbursts. Nevertheless, a region of deep convection is indicated north and east of Nepal in the composited analysis and so we assert that it may be one of several mechanisms that when occurring in the presence of other significant synoptic conditions, may set in motion dynamical processes described below, that can trigger the diversion of the low – level monsoon flow and ultimately cloudbursts.

The formation of low-level low-pressure and upper-level high-pressure northwest of this negative OLR anomaly suggests a dynamic response to the heating from this negative OLR anomaly. The eastward extension of eastern part of the upper-level high-pressure center is also consisted with this dynamic response. Till -5day, this high-pressure center

expanded eastward. From -4day to -2day the negative OLR anomaly (heating center) slightly weakens and shifts westward. This westward shift of negative OLR anomaly seems to be associated with formation of low-level low-pressure center as a dynamic response to the heating of -6day to -5day. From -4day, the upper-level high-pressure center extends westward and 850 hPa monsoon trough also retracted westward from the Bay of Bengal. This westward migration of upper-level high center is the eddy shedding process as explained by Hsu and Plumb (2000). According to the authors, this process occurs to overcome the violation of the vorticity constraint in the presence of divergence from the heating force. The upper-level high-pressure center extends up to 20E by -1day (Figure 5.4d). On -1day, negative OLR anomaly center at 25N vanishes and appears at 10N and 110E. On the cloudburst day (0day) the upper-level high-pressure center squeezes and can be seen only over its climatological position. A wavy westerly jet can be seen as the upper-level high-pressure center started extending westward since -5day. From +1 day the upper-level high-pressure center seems to be weakening and by +4day this high-pressure maxima vanishes. The monsoon trough also seems to be modulated during this eddy shedding process. This trough shifts northward since -2day till +2day and weakens there after.

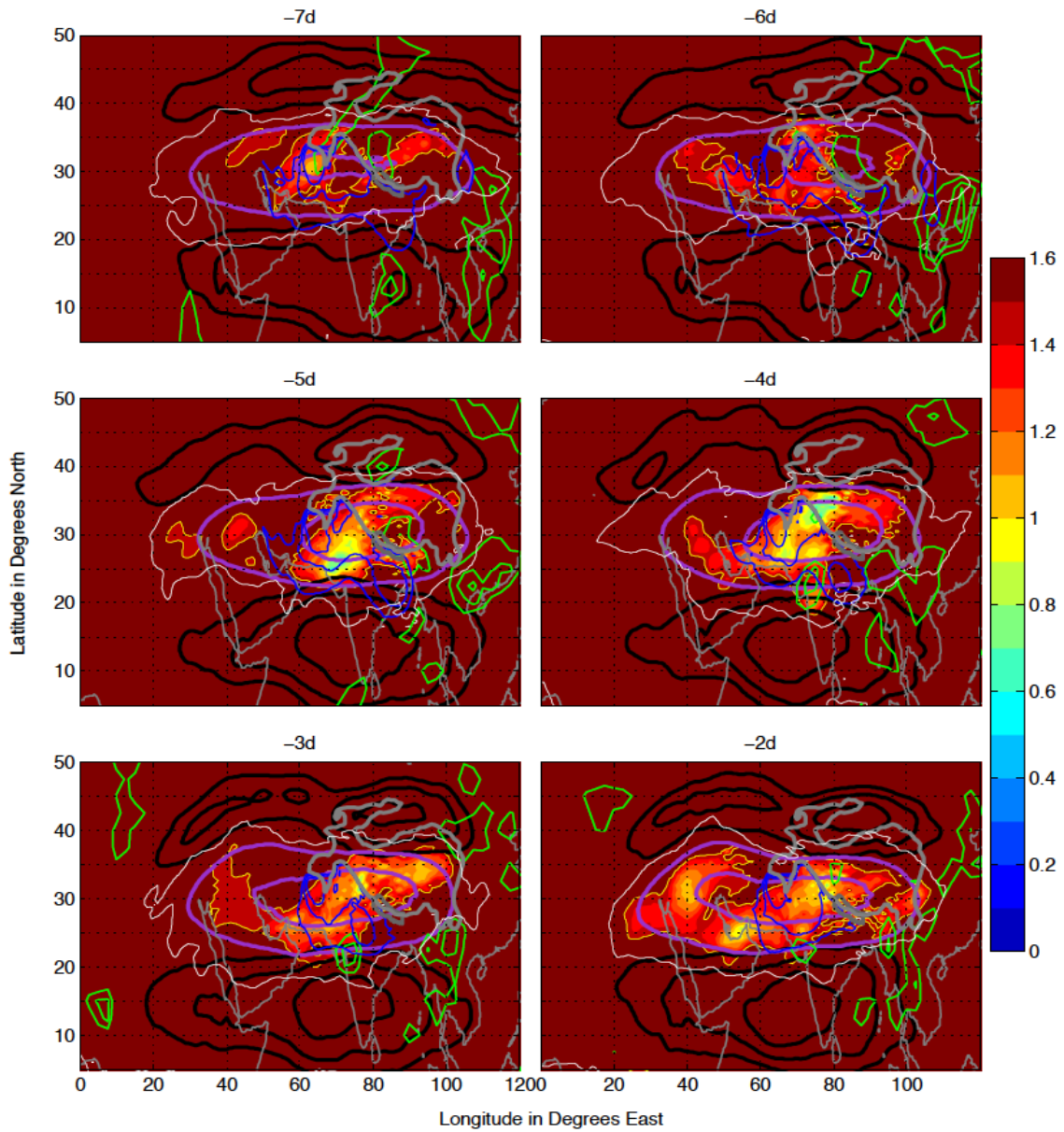


Figure 5.4c: Time evolution showing westward eddy shedding process of upper-level high in response to tropical heating for the cloudburst composite from -7day to -2day. Green contours: negative OLR anomaly ( $-10$  to  $-30\text{w/m}^2$ ) representing tropical heating; Purple contours: Montgomery Streamfunction high at 370K; Blue contours: monsoon trough (low pressure) at 850 hPa; Black contours: Easterly and Westerly Jets; Shading: PV in PVU; Yellow contour: 1.5 PVU; White contour: 2 PVU. Continuation in next figure.

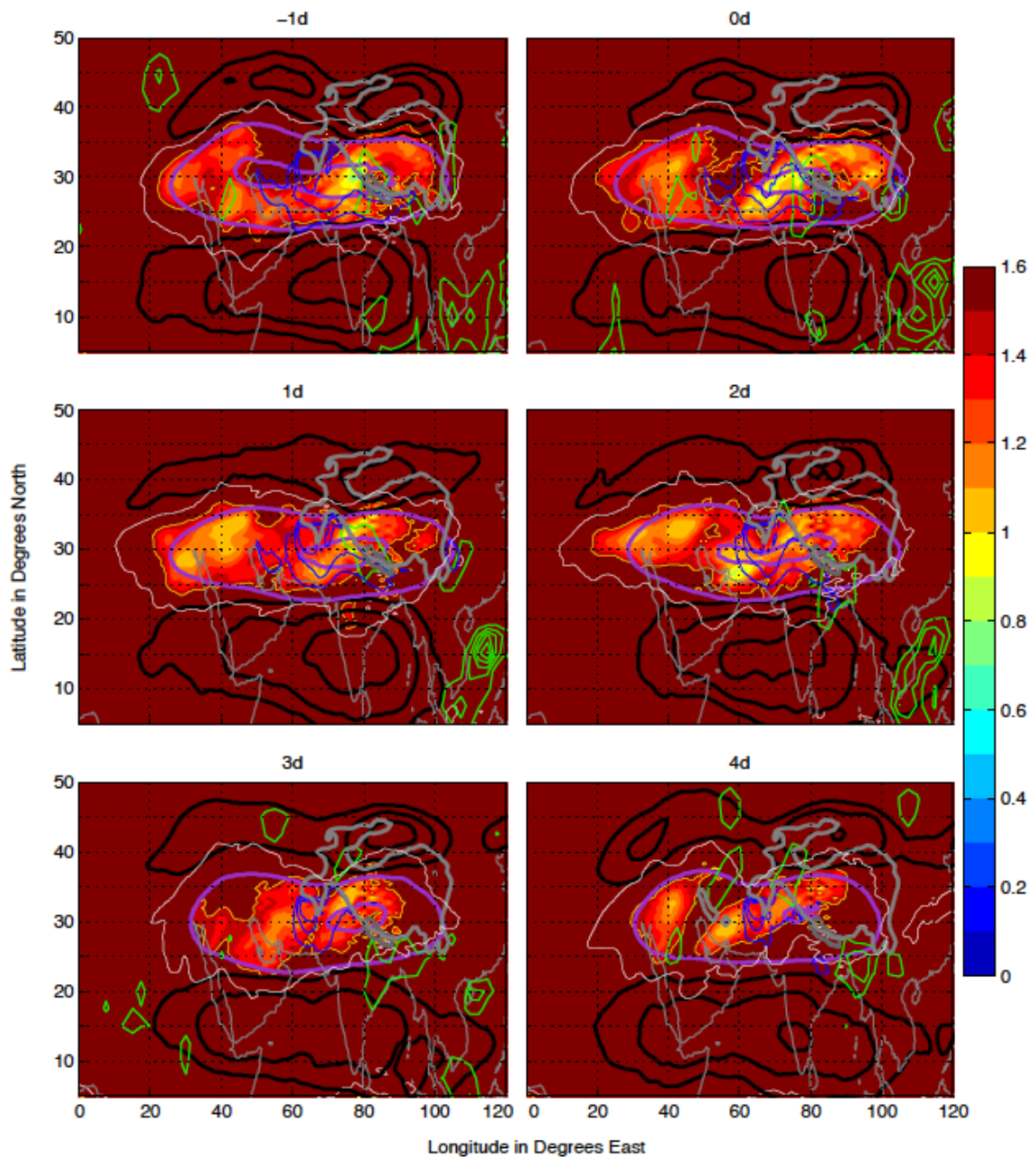


Figure 5.4d: Continuation of Figure 5.4c. Time evolution showing westward eddy shedding process of upper-level high in response to tropical heating for the cloudburst composite from -1 day to +4 day. Green contours: negative OLR anomaly ( $-10$  to  $-30 \text{ w/m}^2$ ) representing tropical heating; Purple contours: Montgomery Streamfunction high at 370K; Blue contours: monsoon trough (low pressure) at 850 hPa; Black contours: Easterly and Westerly Jets; Shading: PV in PVU; Yellow contour: 1.5 PVU; White contour: 2 PVU

Another important feature of the eddy shedding process is the modulation of upper-level low PV pattern as explained by Hsu and Plumb (2000). Figure 5.4e shows the time evolution of westward and northward propagation of low PV (less than 1.5 PVU) and

wind vectors at 370K, associated with the eddy shedding process. According to Hsu and Plumb (2000), the transient eddies, formed as a result of unsteady condition generated by divergence are the agents of westward propagation of low PV. These transient eddies, by balancing unsteady term (as given by Eq 3 in chapter 2), help to meet the constraint expressed in Eq. (4) in Chapter 2. On -7day area occupied by low PV is lowest and centered at 30N and 60E. On -6day a new low PV minimum developed, centered at around 27N & 80E. On -5day, the lowest PV is centered at 25N70E. This low PV of -7day and -5day seems to be the response of heating force as shown by Hsu and Plumb (2000) that forms west or southwest of heating forcing. The low PV minimum of -5day is slightly west of low PV minima of -6day, which shows process of westward eddy shedding process. On -4day, this low PV minima seems to be advected in two directions: northward and westward. The northward branch seems to associated with the northerly flow due to the development of anticyclonic eddy at around 30N, 80E as a dynamic response of monsoonal heating and on -3day. This anticyclone pattern is similar to the eddy shedding pattern shown by Hsu and Plumb (2000) for the heating force is between subtropics and near-equator and high beta parameter (Figure 2.15, chapter 2). As this low PV reaches north of 35N, it seems to be caught by westerly flow. The westward branch of low PV on -4day seems to be associated with the westward eddy shedding process as explained by Hsu and Plumb (2000). By -3day, as this westward propagating low PV stream caught by the northerly flow (at 40N) of the Asian anticyclone (Tibetan High) and the low PV propagates northward. This two northward propagating low PV streams, at 40E and 70E, seems to squeeze a high PV stream in between and could be the initiation of southward movement of extratropical trough.

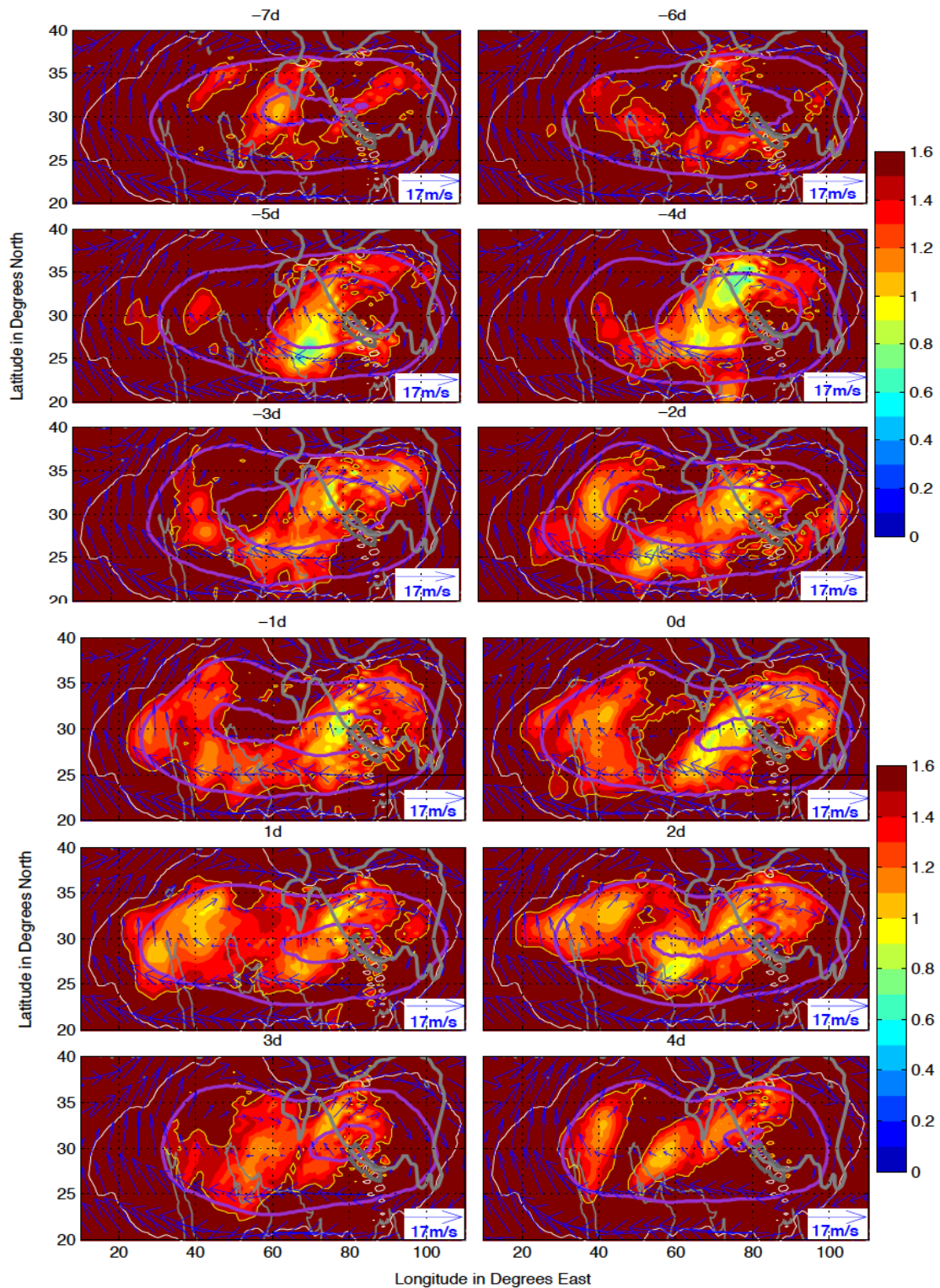


Figure 5.4e: Time evolution showing westward eddy shedding process of upper-level low PV (1.5 PVU) and wind vectors at 370K in response to tropical heating for the cloudburst composite from -7 day to +4day Shading: PV in PVU; Yellow contour: 1.5 PVU; White contour: 2 PVU; Purple contours: Montgomery Streamfunction high at 370K; Blue contours: monsoon trough (low pressure) at 850 hPa;

On -2day, the low PV stream at 40E caught by the westerly flow and seems to move eastward at 35N, while low PV stream at 70E, still fed by low PV from low latitude. Though low PV minima at 70E and 35N on -2days spreads eastward, low PV at this location seems stationary while the low PV at 40E seems to propagate eastward, producing deep high PV stream from mid-latitudes in between 40E and 70E. On -1day at 35N, the western low PV minima reaches 30E while eastern low PV minima remains stationary at 70E and spreading low PV eastward north of 30N. In the meantime another high PV stream moved southward by the southerly flow in the eastern flank of the upper-level high. This high PV stream is caught by easterly flow and moves westward (northwestward). On the cloudburst day (0day) at 35N, the western PV minima reaches 50E, which deepens the trough with high PV east of this low PV minima at 70E. On this day, low PV is minimum north of 30N and maximum south of 30N between 80E and 90E (Nepal Himalayas). The low PV seems to occupy large area on +1day and +2day and then start shrinking reaching again to the pattern similar to the initial (-7day) or climatological stage.

### **5.5 Discussion: Potential Association of Tropical Heating with the Favorable Synoptic Conditions for the Cloudbursts through Eddy Shedding Process**

Hsu and Plumb (2000) showed how latitudinal variation in the location of heating forcing can produce different patterns of eddy shedding in the upper-level anticyclones. According to them when heating function in higher latitude the eddy shedding process produce westerly wave with southward intrusion of deep trough while the heating source in lower latitude produce westward-elongated high-pressure center and low PV stream. In the cloudburst cases, the negative OLR anomaly representing monsoonal heating function is at around 25N, which is at higher latitude than the climatological position of OLR

minima at 15N from 6 days before the event till 4 days before the event. The results of eddy shedding processes and the westerly wave pattern in association with negative OLR anomaly at 25N discussed in section 5.4 is consistent with the results on the eddy shedding (westward movement of upper-level high center and low PV centers) process and wave pattern for the heating source between equator and subtropics in Hsu and Plumb (2000).

Figure 5.5 shows the low PV, upper-level high and lower-level low pattern on cloudburst day. Low PV north of the Nepal Himalayas and high PV south of the Nepal Himalayas are consisted with the flow pattern generated by eddy shedding process. This suggests that eddy-shedding process is the mechanism that is associated with the weakening the inertial constraint north of the Nepal Himalayas by bringing low PV here and strengthening the inertial constraint in the south of the Nepal Himalayas by advecting high PV. It appears that eddy-shedding process seems to play two roles in the tropical-extratropical interaction during the cloudburst events. First, this process seems to be associated with southward intrusion of deep trough and PV anomaly over the Nepal Himalayas intensifying pre-existed monsoon trough in the lower-level. Second, this eddy shedding process by weakening the inertial constraint north of the Himalayas and strengthening the inertial constraint south of the Himalayas was able to enhance northward tropical-extratropical interaction. The force imbalance north of the Nepal Himalayas appears to be associated with this low PV advection of the eddy shedding process.

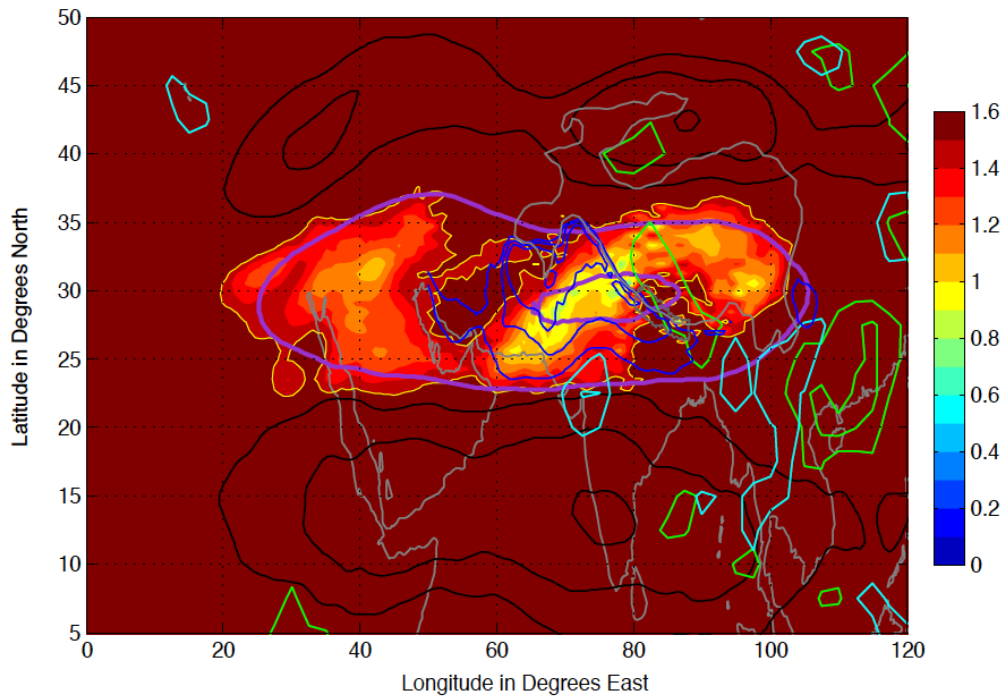


Figure 5.5: Snapshot ( 0 day cloudburst composite ) of westward eddy shedding process of upper-level low PV (1.5 PVU) at 370K in response to tropical heating. Shading: PV in PVU; Yellow contour: 1.5 PVU; White contour: 2 PVU; Purple contours: Montgomery Streamfunction high at 370K; Blue contours: monsoon trough (low pressure) at 850 hPa. Green contour: 3-day (-7d to -5d) mean negative OLR anomaly ( $-10$  to  $-30 \text{ W/m}^2$ ); Cyan contour: 3-day (-4d to -2d) mean negative OLR anomaly ( $-10$  to  $-30 \text{ W/m}^2$ )

The eddy shedding process presented in Section 5.4 provides an explanation how the monsoonal heat leads to the number of events (southward shift of upper-level trough, upper-level PV anomaly, weak inertial stability north of the Himalayas) via eddy shedding process and brings favorable synoptic conditions for the cloudbursts. First, the eddy shedding process explains how the monsoonal heating leads to the Rossby wave break, southward intrusion of westerly trough and positive PV anomaly over the Nepal Himalayas. Second, it also explains how, low PV from the low latitude is advected to north of Nepal Himalayas and high PV from high latitude is advected to the south of Nepal Himalayas. Low PV (high PV) is one of the indicators of low (high) inertial stability, which is similar to negative value of  $\alpha$  (force balance parameter).

## Chapter 6

### Conclusions and Future Work

#### 6.1 Conclusions

Despite the catastrophic impact on the human lives and the socio-economy in the Himalayan countries, only little attention is given to the meteorological study of “cloudbursts” and for those studies, the was mostly limited to the damage and flood assessment. Understanding cloudburst dynamics not only has huge implications in predicting this phenomenon in order to save lives in the Himalayan region but also has implications in the scientific community regarding the unique dynamics of this phenomena. The purpose of this study is of two fold. The first is to address the question how cloudburst synoptic conditions are different from normal monsoon synoptic systems. The second is to explore what and how favorable conditions for the cloudbursts are triggered. To address these questions three hypothesis were set and tested.

The study proved the first hypothesis that synoptic conditions during the cloudbursts are significantly different from the normal climatological monsoon conditions. Based on composite analysis this study proposes a conceptual model describing the interaction of observed upper-level and surface synoptic features during cloudburst events. The conceptual model includes the shift of the easterly and westerly jets to locations closer to the Nepal Himalayas. Analyses suggest that this might have played an important role for favorable condition for the large-scale enhance rising motion. An upper-level trough and PV anomaly might have also played critical roles in triggering and intensifying a surface low over the Nepal Himalayas and helping stronger southerly surface flow from the Arabian Sea to converge towards the slopes of the Nepal Himalayas.

This study proved a second hypothesis that, during the cloudburst events, tropical-extratropical interaction exceeds climatology. The study found that along the longitudinal cross-section of Nepal the northern local Hadley Cell is stronger, northward transport of westerly momentum by mean circulation, by both transient and stationary eddies is stronger than expected from the climatological means. Bordoni and Schneider (2008) argued that the horizontal flux divergence by transient eddies have a capacity to strengthen the Hadley cell. It is interesting to point out that the transport by the mean meridional circulation is nevertheless greater than by the transient eddies. This suggests that transient eddies may not have a dominant role in transporting momentum or to strengthening the local Hadley cell.

Third this study found that a northward-displaced tropical heating anomaly, represented by negative OLR minima, precedes the cloudburst events. The heating from a negative OLR minima, appearing in composited average conditions, is consistent with the enhanced eddy shedding process and the southward intrusion of upper-level trough west of Nepal Himalayas. The weak inertial force north of the Nepal Himalayas and strong inertial force south of the Nepal Himalayas, which is consistent with the enhanced tropical-extratropical interaction during the cloudbursts, seems to be associated with the low and high PV advection during the eddy shedding process. Therefore this study suggests that strong convective heating north and east of typical monsoon under proper conditions can lead to the enhanced low PV eddy shedding that in turn, breaches the inertial wall that contains the monsoon circulation south of the Himalayas from interacting with flow to the north. The result is the upper-level eruption of a poleward flowing tropical plume that connects to low levels by drawing the monsoon flow poleward, across the Himalayas, leading to cloudbursts events in the Nepal Himalayas.

## 6.2 Limitations

Since in situ storm data is quite limited, this study relied on daily rainfall measurements from direct observations augmented by satellite-derived estimates, to identify the cloudbursts. If directly observed vertical profiles of thermodynamic quantities were available, observationally-derived criteria for these events could have been developed. Instead, especially in the upper-level, this research used reanalysis data (ERA-Interim). Since there are no real-time upper-level observations taken in Nepal, limited in-situ information was incorporated in ERA-Interim reanalysis data. Although the upper-air ERA-Interim analysis cannot be verified directly against locally collected data, the data collected in the region of Asia and southern Asia together with satellite derived observations constrain the assimilated analysis and have demonstrated significant skill toward verification where data is available.

For this reason, this study did not focus on case studies, storm structure and thermodynamics and evolution of storm and instead focused on how large scale conditions, resolved by the reanalysis systems, varied from normal or average conditions during the cloud burst events.

This study used eddy-shedding theory based on the findings of Hsu and Plum (2000). According to this study, the eddy shedding pattern depends on the background zonal wind and strength of divergent wind, strength of beta-drift and latitudinal location of the heating function. The conclusions on eddy-shedding analysis in this dissertation, however, are only based on the latitudinal location of the heating center and did not incorporate other factors mentioned in Hsu and Plumb (2000).

### 6.3 Future Work

Unavailability of sufficient in situ rainfall intensity data for cloudburst events limits our ability to analyze and identify cloudbursts based on rainfall intensity criteria. In such case well-evaluated remotely sensed data, like TRMM and Global Precipitation Measurement (GPM), could be very useful. Das et al. (2006) used TRMM hydrometeor data to compare the simulation results on cloudburst. Therefore, studies using satellite data to understand the thermodynamic structure of the cloudbursts in the Nepal Himalayas should be performed.

The synoptic features identified for the cloudbursts in the Nepal Himalayas showed some similarities with the active monsoon condition in the Nepal Himalayas and the monsoon break in India. For example, the northward shift of monsoon trough that identified during the cloudburst events was also observed during the active monsoon case in the Nepal Himalayas and the monsoon break in India. Similarly, the southward shift of upper-level mid-latitude trough found during the cloudbursts was also noted during monsoon break in India. Since, as discussed in Section 2.1.2a, the rainfall pattern during the cloudbursts are different from the typical active monsoon condition in the Nepal Himalayas, it is important to compare the atmospheric dynamics of the cloudbursts with the dynamics of the monsoon break in India and active monsoon in the Nepal Himalayas. The question for further research would be whether the dynamics of the cloudbursts are similar to the dynamics of monsoon break in India and active phase in the Nepal Himalayas, with only difference being increased magnitude of the significant synoptic features during the cloudbursts compared with during the monsoon break in India and active monsoon in the Nepal Himalayas or the dynamics of the cloudbursts are totally different from the

dynamics of the active monsoon in the Nepal Himalayas and monsoon break in India.

The further research should focus on comparing following aspects between cloudburst events and monsoon break in India and active monsoon in the Nepal Himalayas

- Upper-level synoptic features
- Northward momentum transport
- Eddy-shedding process
- Upper-level Force balance analysis

The findings on eddy shedding use only the beta-parameter from Hsu and Plumb (2000) and did not cover the role of background zone flow on eddy shedding during cloudburst event. Further research can be done on examining the role of background zone flow on eddy shedding during the cloudbursts.

## References

- Alaka, M., 1961: The Occurrence of Anomalous Winds and Their Significance. *Mon. Weather Rev.*, **89**, 482–494, doi:10.1175/1520-0493(1961)089<0482:TOOAWA>2.0.CO;2.
- Arreola, J. L., V. Homar, and R. Romero, 2003: Multiscale numerical study of the 10-12 november 2001 strong cyclogenesis event in the western mediterranean. *Proceedings of the 4th EGS Plinius Conference held at Mallorca, Spain, October 2002*, 10–14  
<http://www.eumetcal.org/resources/ukmeteocal/cyclomed/www/english/msg/ciclom ed/library/aaa.pdf>.
- Bao, X., and F. Zhang, 2012: Evaluation of NCEP – CFSR , NCEP – NCAR , ERA-Interim , and ERA-40 Reanalysis Datasets against Independent Sounding Observations over the Tibetan Plateau. *J. Clim.*, **26**, 206–214, doi:10.1175/JCLI-D-12-00056.1.
- Barros, A. P., M. Joshi, J. Putkonen, and D. W. Burbank, 2000: A study of the 1999 monsoon rainfall in a mountainous region in central Nepal using TRMM products and rain gauge observations. *Geophys. Res. Lett.*, **27**, 3683–3686.
- Blanchard, D. O., W. R. Cotton, and J. M. Brown, 1998: Mesoscale Circulation Growth under Conditions of Weak Inertial Instability. *Mon. Weather Rev.*, **126**, 118–140, doi:10.1175/1520-0493(1998)126<0118:MCGUCO>2.0.CO;2.
- Bordoni, S., and T. Schneider, 2008: Monsoons as eddy-mediated regime transitions of the tropical overturning circulation. *Nat. Geosci.*, **1**, 515–519, doi:10.1038/ngeo248.
- Bosart, L. F., J. M. Cordeira, T. J. Galarneau, B. J. Moore, and H. M. Archambault, 2012: An Analysis of Multiple Predecessor Rain Events ahead of Tropical Cyclones Ike and Lowell: 10–15 September 2008. *Mon. Weather Rev.*, **140**, 1081–1107, doi:10.1175/MWR-D-11-00163.1.
- Bretherton, C. S., M. Widmann, V. P. Dymnikov, J. M. Wallace, and I. Bladé, 1999: The effective number of spatial degrees of freedom of a time-varying field. *J. Clim.*, **12**, 1990–2009, doi:10.1175/1520-0442(1999)012<1990:TENOSD>2.0.CO;2.
- Chang, C.-P., S. C. Hou, H. C. Kuo, and G. T. J. Chen, 1998: The Development of an Intense East Asian Summer Monsoon Disturbance with Strong Vertical Coupling. *Mon. Weather Rev.*, **126**, 2692–2712, doi:10.1175/1520-0493(1998)126<2692:TDOAIE>2.0.CO;2.
- Das, S., R. Ashrit, and M. W. Moncrieff, 2006: Simulation of a Himalayan cloudburst event. *J. Earth Syst. Sci.*, **115**, 299–313, doi:10.1007/BF02702044.

- Demott, C. A., C. Stan, and D. A. Randall, 2013: Northward Propagation Mechanisms of the Boreal Summer Intraseasonal Oscillation in the ERA-Interim and SP-CCSM. *J. Clim.*, **26**, 1973–1992, doi:10.1175/JCLI-D-12-00191.1.
- Dhital, M. R., N. Khanal, and K. B. Thapa, 1993: The Role of Extreme Weather Events\_ Mass Movements\_ and Land Use Changes.pdf.
- Ding, Q., and B. Wang, 2007: Intraseasonal Teleconnection between the Summer Eurasian Wave Train and the Indian Monsoon\*. *J. Clim.*, **20**, 3751–3767, doi:10.1175/JCLI4221.1.
- , and ———, 2009: Predicting Extreme Phases of the Indian Summer Monsoon\*. *J. Clim.*, **22**, 346–363, doi:10.1175/2008JCLI2449.1.
- Doswell, C. A., III, 1985: 1985: *The operational meteorology of convective weather. Volume II: Storm scale analysis. NOAA Tech. Memo. ERL ESG-15.*
- Emanuel, K. a., 1980: Inertial Instability and Mesoscale Convective Systems. Part I: Linear Theory of Inertial Instability in Rotating Viscous Fluids. *J. Atmos. Sci.*, **36**, 2425–2449, doi:10.1175/1520-0469(1979)036<2425:IIAMCS>2.0.CO;2.
- , 1982: Inertial Instability and Mesoscale Convective Systems. part II. Symmetric CISK in a Baroclinic Flow. *J. Atmos. Sci.*, **39**, 1980–1097.
- European Centre for Medium-Range Weather Forecasts, 2009: ERA-Interim Project. <http://rda.ucar.edu/datasets/ds627.0/>.
- Fierli, F., S. Pinori, S. Dietrich, C. Medaglia, and G. J. Tripoli, 2003: Potential vorticity analysis of the storm event of the 9-10 november algerian flood. *Proceedings of the Fourth EGS Plinius Conference, October 2002, Mallorca, Spain*, 10–13.
- Flohn, H., 1964: Investigations on the tropical easterly jet. *Bonner Meteorol. Abhandl.*, **4**, 83 pp.
- Galarneau, T. J., L. F. Bosart, and R. S. Schumacher, 2010: Predecessor Rain Events ahead of Tropical Cyclones. *Mon. Weather Rev.*, **138**, 3272–3297, doi:10.1175/2010MWR3243.1.
- Garny, H., and W. J. Randel, 2013: Dynamic variability of the Asian monsoon anticyclone observed in potential vorticity and correlations with tracer distributions. *J. Geophys. Res. Atmos.*, **118**, 13421–13433, doi:10.1002/2013JD020908.
- Gill, a. E., 1980: Some simple solutions for heat induced tropical circulation. *Q. J. R. Meteorol. Soc.*, **106**, 447–462, doi:10.1002/qj.49710644905. <http://onlinelibrary.wiley.com/doi/10.1002/qj.49710644905/full>.
- Grist, J. P., S. E. Nicholson, and A. I. Barcilon, 2002: Easterly Waves over Africa. Part II: Observed and Modeled Contrasts between Wet and Dry Years. *Mon. Weather Rev.*, **130**, 212–225, doi:10.1175/1520-0493(2002)130<0212:EWOAPI>2.0.CO;2.

- Hartmann, D. L., 2016: Time (or Space) Series Analysis: ATM552 Notes. [www.atmos.washington.edu/~dennis/552\\_Notes\\_6a.pdf](http://www.atmos.washington.edu/~dennis/552_Notes_6a.pdf), 128–150, doi:10.1017/CBO9781107415324.004. [http://www.atmos.washington.edu/~dennis/552\\_Notes\\_6a.pdf](http://www.atmos.washington.edu/~dennis/552_Notes_6a.pdf).
- Hastenrath, S., 1991: Regional Circulation Systems. *Climate Dynamics of the Tropics*, 114–218.
- Held, I. M., and a. Y. Hou, 1980: Nonlinear axially symmetric circulations in a nearly inviscid atmosphere. doi:10.1175/1520-0469(1980)037<0515:NASCIA>2.0.CO;2.
- Homar, V., C. Ramis, and S. Alonso, 2002: A deep cyclone of African origin over the Western Mediterranean: diagnosis and numerical simulation. *Ann. Geophys.*, **20**, 93–106, doi:10.5194/angeo-20-93-2002.
- Hong, C.-C., H.-H. Hsu, N.-H. Lin, and H. Chiu, 2011: Roles of European blocking and tropical-extratropical interaction in the 2010 Pakistan flooding. *Geophys. Res. Lett.*, **38**, 1–6, doi:10.1029/2011GL047583.
- Hoskins, B. J., and F.-F. Jin, 1991: The initial value problem for tropical perturbations to a baroclinic atmosphere. *Q. J. R. Meteorol. Soc.*, **117**, 299–317, doi:10.1002/qj.49711749803. <http://doi.wiley.com/10.1002/qj.49711749803>.
- Hoskins, B. J., and M. J. Rodwell, 1995: A Model of the Asian Summer Monsoon. Part I: The Global Scale. *J. Atmos. Sci.*, **52**, 1329–1340, doi:10.1175/1520-0469(1995)052<1329:AMOTAS>2.0.CO;2. [http://dx.doi.org/10.1175/1520-0469\(1995\)052<1329:AMOTAS>2.0.CO](http://dx.doi.org/10.1175/1520-0469(1995)052<1329:AMOTAS>2.0.CO).
- Hoskins, B. J., M. E. McIntyre, and A. W. Robertson, 1985: OF THE METEOROLOGICAL OCTOBER 1985. *Q. J. R. Meteorol. Soc.*, **111**, 877–946.
- Houze, R. A., D. C. Wilton, and B. F. Smull, 2007: Monsoon convection in the Himalayan region as seen by the TRMM Precipitation Radar. **1411**, 1389–1411, doi:10.1002/qj.
- Hsu, C. J., and R. A. Plumb, 2000: Nonaxisymmetric Thermally Driven Circulations and Upper-Tropospheric Monsoon Dynamics. *J. Atmos. Sci.*, **57**, 1255–1276, doi:10.1175/1520-0469(2000)057<1255:NTDCAU>2.0.CO;2.
- ISET-N and ISET, 2009: *Vulnerability through the Eyes of the vulnerable: Climate Change Induced Uncertainties and Nepal's Development Predicaments*.
- Jin, F., and B. J. Hoskins, 1995: The Direct Response to Tropical Heating in a Baroclinic Atmosphere. *J. Atmos. Sci.*, **52**, 307–319, doi:10.1175/1520-0469(1995)052<0307:TDRTH>2.0.CO;2. [http://journals.ametsoc.org/doi/abs/10.1175/1520-0469\(1995\)052<0307:TDRTH>2.0.CO;2](http://journals.ametsoc.org/doi/abs/10.1175/1520-0469(1995)052<0307:TDRTH>2.0.CO;2) [http://journals.ametsoc.org/doi/pdf/10.1175/1520-0469\(1995\)052<0307:TDRTH>2.0.CO;2](http://journals.ametsoc.org/doi/pdf/10.1175/1520-0469(1995)052<0307:TDRTH>2.0.CO;2).

- Kiladis, G. N., and K. M. Weickmann, 1992a: Extratropical Forcing of Tropical Pacific Convection during Northern Winter. *Mon. Weather Rev.*, **120**, 1924–1938.
- , and ———, 1992b: Circulation anomalies associated with tropical convection during northern winter. *Mon. Weather Rev.*, **120**, 1900–1923.
- Knippertz, P., 2007: Tropical–extratropical interactions related to upper-level troughs at low latitudes. *Dyn. Atmos. Ocean.*, **43**, 36–62, doi:10.1016/j.dynatmoce.2006.06.003. <http://linkinghub.elsevier.com/retrieve/pii/S0377026506000583> (Accessed July 16, 2014).
- Koteswaram, P., 1958: The Easterly Jet Stream in the tropics\*. *Tellus*, **X**, 43–57.
- Krishnamurti, T.N. and Bhalme, H. N., 1976: Oscillations of a Monsoon System. Part I. Observational Aspects. *J. Atmos. Sci.*, **33**, 1937–1954.
- Krishnan, R., Zhang, C. and Sugi, M., 2000: Dynamics of Breaks in the Indian Summer Monsoon. *J. Atmos. Sci.*, **57**, 1354–1372.
- Lau, K.-M., and H. Lim, 1982: Thermally driven motions in an equatorial  $\beta$ -plane: Hadley and Walker circulations during the winter monsoon. *Mon. Weather Rev.*, **110**, 336–353.
- Leith, C. E., 1973: The Standard Error of Time-Average Estimates of Climatic Means. *J. Appl. Meteorol.*, **12**, 1066–1069, doi:10.1175/1520-0450(1973)012<1066:TSEOTA>2.0.CO;2.
- Lin, Y.-L., S. Chiao, T.-A. Wang, M. L. Kaplan, and R. P. Weglarz, 2001: Some Common Ingredients for Heavy Orographic Rainfall. *Weather Forecast.*, **16**, 633–660, doi:10.1175/1520-0434(2001)016<0633:SCIFHO>2.0.CO;2.
- Maddox, R. A., L. R. Hoxit, C. F. Chappell, and F. Caracena, 1978: Comparison of Meteorological Aspects of the Big Thompson and Rapid City Flash Floods. *Mon. Weather Rev.*, **106**, 375–389.
- Martin, J. E., 2006: *Mid-Latitude Atmospheric Dynamics: A First Course*. 1st ed. Wiley, <http://www.amazon.com/exec/obidos/redirect?tag=citeulike07-20&path=ASIN/0470864656>.
- Martius, O., and Coauthors, 2012: The role of upper-level dynamics and surface processes for the Pakistan flood of July 2010. *Q. J. R. Meteorol. Soc.*, doi:10.1002/qj.2082.
- Massacand, A. C., H. Wernli, and H. C. Davies, 1998: Heavy precipitation on the alpine southside An upperlevel precursor. *Geophys. Res. Lett.*, **25**, 1435–1438, doi:10.1029/98GL50869.
- Matsuno, T., 1966: Quasi-geostrophic motions in the equatorial area. *J. Meteorol. Soc. Japan*, **44**, 25–43, doi:10.1002/qj.49710644905.

[https://www.jstage.jst.go.jp/article/jmsj1965/44/1/44\\_1\\_25/\\_article](https://www.jstage.jst.go.jp/article/jmsj1965/44/1/44_1_25/_article) \n<http://www.mcrones.com/tropical/2008/NPS/MR4242/Week2/Matsuno.PDF>.

- Mecikalski, J. R., and G. J. Tripoli, 2003: Influence of upper-tropospheric inertial stability on the convective transport of momentum. *Q. J. R. Meteorol. Soc.*, **129**, 1537–1563, doi:10.1256/qj.00.08. <http://dx.doi.org/10.1256/qj.00.08>.
- Miller, M., 1978: The Hampstead storm: A numerical simulation of a quasi-stationary cumulonimbus system. *Q. J. R. Meteorol. Soc.*, **104**, 413–427, doi:10.1256/smsqj.44013. <http://www.ingentaeselect.com/rpsv/cgi-bin/cgi?ini=xref&body=linker&reqdoi=10.1256/smsqj.44013>.
- Mooley, D., 1973: Some aspects of Indian monsoon depressions and the associated rainfall. *Mon. Weather Rev.*, **318**, 271–280, doi:10.1175/1520-0493(1973)101<0271:SAOIMD>2.3.CO;2. [http://journals.ametsoc.org/doi/abs/10.1175/1520-0493\(1973\)101<0271:SAOIMD>2.3.CO;2](http://journals.ametsoc.org/doi/abs/10.1175/1520-0493(1973)101<0271:SAOIMD>2.3.CO;2).
- Moore, B. J., L. F. Bosart, D. Keyser, and M. L. Jurewicz, 2013: Synoptic-scale Environments of Predecessor Rain Events Occurring East of the Rocky Mountains in association with Atlantic Basin Tropical Cyclones. *Mon. Weather Rev.*, 121018124620006, doi:10.1175/MWR-D-12-00178.1.
- Peters, J. M., and P. J. Roebber, 2014: Synoptic Control of Heavy-Rain-Producing Convective Training Episodes. *Mon. Weather Rev.*, **142**, 2464–2482, doi:10.1175/MWR-D-13-00263.1. <http://journals.ametsoc.org/doi/abs/10.1175/MWR-D-13-00263.1>.
- Petterssen, S., 1953: On the Relation between Vorticity, Deformation and Divergence and the Configuration of the Pressure Field. *Tellus*, **5**, 231–237, doi:10.1111/j.2153-3490.1953.tb01052.x. <http://doi.wiley.com/10.1111/j.2153-3490.1953.tb01052.x>.
- Pontrelli, M. D., G. Bryan, and J. M. Fritsch, 1999: The Madison County, Virginia, Flash Flood of 27 June 1995. *Weather Forecast.*, **14**, 384–404, doi:10.1175/1520-0434(1999)014<0384:TMCVFF>2.0.CO;2. <http://journals.ametsoc.org/doi/abs/10.1175/1520-0434%281999%29014%3C0384%3ATMCVFF%3E2.0.CO%3B2>.
- Popovic, J. M., and R. A. Plumb, 2001: Eddy Shedding from the Upper-Tropospheric Asian Monsoon Anticyclone. *J. Atmos. Sci.*, **58**, 93–104, doi:10.1175/1520-0469(2001)058<0093:ESFTUT>2.0.CO;2.
- Postel, G. a., and M. H. Hitchman, 1999: A Climatology of Rossby Wave Breaking along the Subtropical Tropopause. *J. Atmos. Sci.*, **56**, 359–373, doi:10.1175/1520-0469(1999)056<0359:ACORWB>2.0.CO;2.
- , and ———, 2001: A Case Study of Rossby Wave Breaking along the Subtropical Tropopause. *Mon. Weather Rev.*, **129**, 2555–2569, doi:10.1175/1520-0493(2001)129<2555:acsorw>2.0.co;2.

- Privé, N. C., and R. A. Plumb, 2007a: No TMonsoon Dynamics with Interactive Forcing. Part I: Axisymmetric Studies. *J. Atmos. Sci.*, **64**, 1417–1430, doi:10.1175/JAS3916.1.
- Privé, N. C., and R. A. Plumb, 2007b: Monsoon Dynamics with Interactive Forcing. Part II: Impact of Eddies and Asymmetric Geometries. *J. Atmos. Sci.*, **64**, 1431–1442, doi:10.1175/JAS3917.1.
- Rajeevan, M., S. Gadgil, and J. Bhate, 2010: Active and break spells of the Indian summer monsoon. *J. Earth Syst. Sci.*, **119**, 229–247.
- Ramamurthy, K., 1969: *FORECASTING PART IV MANUAL*.
- Ramaswamy, C., 1962: Breaks in the Indian summer monsoon as a phenomenon of interaction between the easterly and the sub-tropical westerly jet streams'. *Tellus*, **XIV**, 337–349.
- Randall, D. A., 2015: *An Introduction to the Global Circulation of the Atmosphere*. Princeton University Press,.
- Randel, W. J., D. J. Seidel, and L. L. Pan, 2007: Observational characteristics of double tropopauses. *J. Geophys. Res. Atmos.*, **112**, 1–13, doi:10.1029/2006JD007904.
- Rappin, E. D., M. C. Morgan, and G. J. Tripoli, 2011: The Impact of Outflow Environment on Tropical Cyclone Intensification and Structure. *J. Atmos. Sci.*, **68**, 177–194, doi:10.1175/2009JAS2970.1.
- Rasmussen, K. L., and R. a. Houze, 2012: A Flash-Flooding Storm at the Steep Edge of High Terrain: Disaster in the Himalayas. *Bull. Am. Meteorol. Soc.*, **93**, 1713–1724, doi:10.1175/BAMS-D-11-00236.1.
- Riehl, H., 1977: Venezuelan rain systems and the general circulation of the summer tropics II: Relations between low and high latitudes. *Mon. Weather Rev.*, **105**, 1421–1433.
- Roja Raman, M., V. V. M. Jagannadha Rao, M. Venkat Ratnam, M. Rajeevan, S. V. B. Rao, D. Narayana Rao, and N. Prabhakara Rao, 2009: Characteristics of the Tropical Easterly Jet: Long-term trends and their features during active and break monsoon phases. *J. Geophys. Res. Atmos.*, **114**, 1–14, doi:10.1029/2009JD012065.
- Romatschke, U., S. Medina, and R. A. Houze, 2010: Regional, Seasonal, and Diurnal Variations of Extreme Convection in the South Asian Region. *J. Clim.*, **23**, 419–439, doi:10.1175/2009JCLI3140.1.
- Sardeshmukh, P. D., and B. J. Hoskins, 1988: The generation of Global Rotational Flow by Steady Idealized Tropical Divergence. *J. Atmos. Sci.*, **45**, 1228–1251.
- Schneider, E. K., 1977: Axially Symmetric Steady-State Models of the Basic State for Instability and Climate Studies. Part II. Nonlinear Calculations. *J. Atmos. Sci.*, **34**, 280–296, doi:10.1175/1520-0469(1977)034<0280:ASSSMO>2.0.CO;2.

- Shrestha, A., 1998: Estimation of Evapotranspiration by Penman Monteith Equation and Analysis of General and Extreme Rainfall over Kulekhani Watershed. Tribhuvan University, Kathmandu, Nepal, .
- Shrestha, D., P. Singh, and K. Nakamura, 2012: Spatiotemporal variation of rainfall over the central Himalayan region revealed by TRMM Precipitation Radar. *J. Geophys. Res. Atmos.*, **117**, doi:10.1029/2012JD018140.  
<http://doi.wiley.com/10.1029/2012JD018140> (Accessed July 16, 2014).
- Sikka, D. R., 1977: Some aspects of the life history, structure and movement of monsoon depressions. *Pure Appl. Geophys. PAGEOPH*, **115**, 1501–1529, doi:10.1007/BF00874421.
- Singh, P., and K. Nakamura, 2010: Diurnal variation in summer monsoon precipitation during active and break periods over central India and southern Himalayan foothills. *J. Geophys. Res.*, **115**, D12122, doi:10.1029/2009JD012794.  
<http://doi.wiley.com/10.1029/2009JD012794> (Accessed July 16, 2014).
- Thayyen, R. J., a. P. Dimri, P. Kumar, and G. Agnihotri, 2013: Study of cloudburst and flash floods around Leh, India, during August 4-6, 2010. *Nat. Hazards*, **65**, 2175–2204, doi:10.1007/s11069-012-0464-2.
- Valero, F., M. Y. Luna, and M. L. Martín, 1997: An overview of a heavy rain event in southeastern Iberia: the role of large-scale meteorological conditions. *Ann. Geophys.*, **15**, 494, doi:10.1007/s005850050464.
- Wang, A., and X. Zeng, 2012: Evaluation of multireanalysis products with in situ observations over the Tibetan Plateau. *J. Geophys. Res.*, **117**, 1–12, doi:10.1029/2011JD016553.
- Yamamoto, K., Munehisa, K. Ueno, and K. Nakamura, 2011: Comparison of Satellite Precipitation Products with Rain Gauge Data for the Khumb Region, Nepal Himalayas. *J. Meteorol. Soc. Japan*, **89**, 597–610, doi:10.2151/jmsj.2011-601.
- Yatagai, A., O. Arakawa, K. Kamiguchi, and H. Kawamoto, 2009: A 44-Year Daily Gridded Precipitation Dataset for Asia. *SOLA*, **5**, 3–6.